From ex-vivo to in-vivo preclinical investigation of neurodegenerative diseases

Alessia Sanna

THÈSE

Pour obtenir le grade de

DOCTEUR DE L'UNIVERSITÉ GRENOBLE ALPES

École doctorale : ISCE - Ingénierie pour la Santé la Cognition et l'Environnement
Spécialité : BIS - Biotechnologie, instrumentation, signal et imagerie pour la biologie, la médecine et l'environnement
Unité de recherche : IAB : Epigenetics, Environment, Cell Plasticity, Cancer (UGA / Inserm U1209 / CNRS UMR 5309)

Investigation préclinique ex-vivo et in-vivo des maladies neurodégénératives

From ex-vivo to in-vivo preclinical investigation of neurodegenerative diseases

Présentée par :

Alessia SANNA

Direction de thèse :

Alberto BRAVIN FULL PROFESSOR, UNIVERSITA DEGLI STUDI DI MILANO-BICOCCA	Directeur de thèse
Lucie SANCEY DIRECTRICE DE RECHERCHE, CNRS DELEGATION ALPES	Co-directrice de thèse

Rapporteurs :

PAOLA COAN
FULL PROFESSOR, LUDWIG-MAXIMILIANS-UNIVERSITÄT MÜNCHEN
FULVIA ARFELLI
ASSOCIATE PROFESSOR, UNIVERSITA DEGLI STUDI DI TRIESTE

Thèse soutenue publiquement le **13 décembre 2023**, devant le jury composé de :

ALBERTO BRAVIN FULL PROFESSOR, UNIVERSITA DEGLI STUDI DI MILANO-BICOCCA	Directeur de thèse
LUCIE SANCEY DIRECTRICE DE RECHERCHE, CNRS DELEGATION ALPES	Co-directrice de thèse
PAOLA COAN FULL PROFESSOR, LUDWIG-MAXIMILIANS-UNIVERSITÄT MÜNCHEN	Rapporteure
FULVIA ARFELLI ASSOCIATE PROFESSOR, UNIVERSITA DEGLI STUDI DI TRIESTE	Rapporteure
NAURANG SAINI ASSOCIATE PROFESSOR, UNIV. DEGLI STUDI DI ROMA LA SAPIENZA	Examinateur
PHILIPPE ZEITOUN DIRECTEUR DE RECHERCHE, CNRS DELEGATION ILE-DE-FRANCE SUD	Examinateur
EMMANUEL BARBIER DIRECTEUR DE RECHERCHE, INSERM DELEGATION AUVERGNE-RHONE-ALPES	Examinateur
SAM BAYAT PROFESSEUR DES UNIVERSITES - PRATICIEN HOSPITALIER, UNIVERSITE GRENOBLE ALPES	Président

Invités :

ALESSIA CEDOLA
DIRECTRICE DE RECHERCHE, INSTITUTE OF NANOTECHNOLOGY - NANOTEC CNR (NATIONAL RESEARCH COUNCIL)

Index

Introduction

Neurodegenerative diseases (ND) are disorders affecting millions of people around the word. They are characterized by the progressive loss of function and structure of the cells of the central nervous system and present symptoms related to memory, movement, language [1]. Currently there is no cure for most of the neurodegenerative diseases and the available therapies are focused on the management of the symptoms and on the improvement of the quality of life for the patients [2]. In this context, it is clear that the research and study of the pre-symptomatic states of the disease are crucial to understand its causes and intervene at an early stage. The main imaging methods used for diagnosis of neurodegenerative diseases, including Alzheimer and Parkinson diseases, are MRI and PET, and more rarely CT [3-6]. The visualization and the monitoring [7-10] of the cells involved in the disorder is a fundamental request for this kind of studies, and both molecular and targeted imaging represent powerful tools for this aim. Antibody nanoconjugates are a valid targeted imaging probe recently used as novel approach in several diseases [11-13]. Antibodies are often conjugated with nanoparticles (NP) due to their unique features, such as size, high surface/volume ratio and surface chemistry, which can be conveniently manipulated to bind selected biomolecules. Colloidal NPs based on heavy elements, such as gold and gadolinium, are characterized by high X-ray-attenuation properties and have been proposed and tested as biocompatible [14, 15]and effective long-circulating contrast agents for X-ray imaging and conventional computed tomography [16-18], K-Edge imaging [19] and in other imaging techniques. While monoclonal antibodies (Ab) that target such specific markers have generally been immune reagents of choice, their usefulness for imaging is limited by their large size (atomic mass >150 kDa), which can lead to steric hindrance but also impedes their crossing of the blood-brain barrier (BBB) when imaging the central nervous system. In contrast, nanobodies (Nb) which are single-domain antibodies (sdAbs) are ideally suited for imaging due to their small size enabling them to target antigenic epitopes at locations not easily accessible to

conventional antibodies [20, 21]. sdAbs are composed of the single heavy chain of antibodies that are expressed uniquely in camelids and lack the light chain. The capability to bind antigen is retained by a 15 kDa molecule that is about 10 times smaller than a full Ab. In contrast to conventional Abs, sdAbs can cross the BBB, not only because of their small size, which allows extensive diffusion within cerebral tissue, but also because they can be tailored to increase their BBB-crossing propensity (adjusted surface charge) [21]. Such features, together with their stability and rapid clearance from blood, make sdAbs optimal candidates for molecular imaging in brain. Additionally, such small compounds can be administered intranasally for fast and efficient brain targeting, limiting the injected dose but at the same time directing it more effectively to the targeted brain tissue [22]. Different techniques such as positron emission tomography (PET), single photon emission computed tomography (SPECT), magnetic resonance imaging (MRI) or computed tomography (CT) have been combined to the use of nanoconjugates, but all of them show limits regarding the spatial resolution and the sensitivity [23]. X-ray phase contrast tomography (XPCT) overcomes these limits, enabling a 3D visualization of the entire organ with a spatial resolution ranging from microns to nanometres, permitting the detection of the cells of interest in the physiological and pathological contest. XPCT is able to simultaneously visualize cells, vascular and neuronal systems, together with the surrounding tissue, giving complete information about the morphology and the three-dimensionality of the sample without destroying or compromising it. However, an important limitation of this technique lies in the impossibility of uniquely identifying the cells visualised, except on a morphological/anatomical basis. Combining the Nb-nanoconjugates with the XPCT could represent an incredible boost in the molecular and targeted imaging of neurodegenerative diseases.

In this study, NPs were conjugated with nanobodies able to target astrocytes. The new complex, Nano2, was administered to EAE (Experimental Autoimmune Encephalomyelitis) and healthy mice using different administration routes. Through various steps, the ability of XPCT to detect Nano2 and consequently label the target cells with certainty was demonstrated, making XPCT a specific

technique. This thesis work starts with an overview of the state of the art of current strategies used to understand the mechanisms of neurodegenerative diseases, focusing on the importance of preclinical studies and animal models and mentioning the current imaging techniques used to study ND. Special attention is given to the effectiveness of XPCT in this context. Much space is given to the description of X-rays, their interaction with matter and the concept of X-ray imaging, especially phase contrast X-ray imaging. Information is then provided concerning the different players in this thesis, such as the different techniques used during the experiments, NPs and nanobodies. After an introduction to the concept of tomography, the experiments performed and the results obtained are reported. At the end of the manuscript an appendix with the experimental parameters is included.

State of the art

1.1 Neurodegenerative diseases

Neurodegenerative diseases are a heterogeneous class of disorders affecting millions of people around the world. About 50 million people are affected by dementia, major cause of disability and mortality, costing the world 1 trillion of dollars [24].With the increase of the lifetime, the number of affected people is estimated to rise. Neurodegenerative diseases are characterized by the progressive loss of neurons in the central and peripheral nervous system, leading to an impairment in memory, cognition and motor functions. Alzheimer's disease is the most common neurodegenerative disorder, representing 60-70% of all dementia cases, followed by Parkinson's diseases, with a global prevalence of over 6 million. In addition to these mentioned disorders, there are many others, such as Frontotemporal Dementia, Huntington's diseases, Amyotrophic Lateral Sclerosis, Multiple Sclerosis and so on [25].

Fundamental hallmarks of neurodegenerative diseases and their positioning are schematically reported in Figure 1.1, and are protein aggregation, synaptic and neuronal network dysfunction, aberrant proteostasis, cytoskeletal abnormalities, altered energy homeostasis, DNA and RNA defects, inflammation, and neuronal cell death [1].

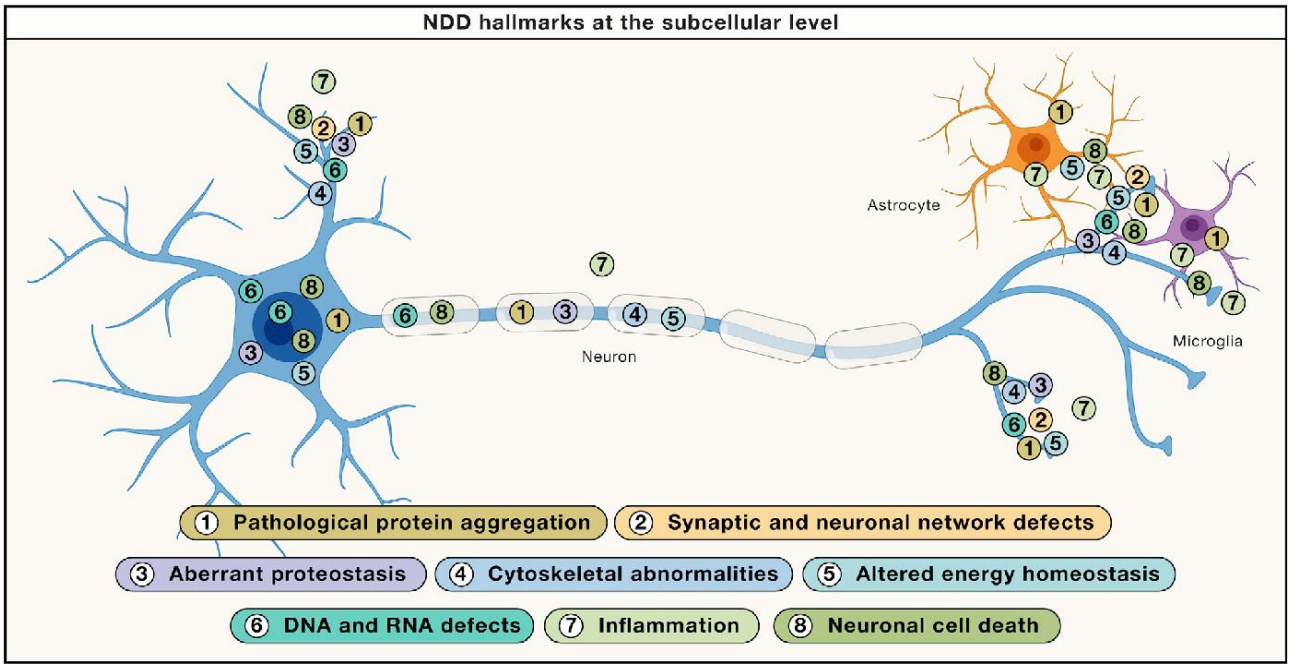

Figure 1.1 Schematic presentation of the NDD hallmarks and their location in the modeled neuron and/or accompanying glial cells. Figure from Wilson et al., Hallmarks of neurodegenerative diseases. *Cell* 186 (4), 693–714.

Often, in particular at the early stage of the disease, neurodegenerative disorders present similar symptoms and there is the risk of a misdiagnosis. Studies comparing clinical diagnoses with autopsy diagnoses indicate that, even at specialized dementia clinics, about 25–30% of patients with a clinical diagnosis of Alzheimer's disease are misdiagnosed. Accurate and timely diagnosis is crucial to optimize treatment strategies and to give patients opportunities to join clinical treatment trials. For this purpose, biomarkers are necessary to improve the diagnostic workup of many neurodegenerative disorders, especially during early stages of the disease.

1.2 Animal models and preclinical studies

To date, there is no cure for neurodegenerative diseases and the identification of effective drugs depends on the understanding of the pathophysiological mechanisms underlying each disease. One

step into this direction depends on the availability of animal models that can mimic the neuropathological and clinical features of each neurodegenerative disease.

Genetic implications and hallmark identification provided the opportunity to create animal models for neurodegenerative diseases able to partially mimic the human disorders, to give insight into molecular mechanisms and to help in the identification of potentially diseases-modifying therapies. No animal model fully phenocopies human disease. Some models can develop a complete neurodegenerative cascade, but it remains uncertain as to whether the entire sequence of pathophysiologic events that occur in the human disease is fully captured.

Despite the obvious limitations of the animal models, they still remain a valid contribution to the understanding of the disorders' mechanisms. Indeed, animals, in particular mammals, are biologically very similar to humans, and basic cell processes are the same in all animals; animals (rodent in particular) have shorter life-cycles than humans so they can be easily studied throughout their whole life-span or across several generations, a crucial element in understanding the disease processes; it is possible to control the environment around the animal and modify the experimental conditions [26, 27].

1.2.2 Experimental Autoimmune Encephalomyelitis (EAE)

The birth of EAE dates back to the first part of the 20th century, when Rivers et al. [28] noted that following repeated vaccination with rabbit brain or brain extract, some monkeys developed brain inflammation and paralysis associated with perivascular infiltrates and demyelination in the brain and spinal cord. Rivers called the disease acute disseminated encephalomyelitis, later changed to experimental allergic or autoimmune encephalomyelitis (EAE).

Previous observations with Pasteur's rabies vaccine, consisting of a suspension of desiccated spinal cord from rabies-infected rabbits, had shown occasional encephalomyelitis leading to paralysis of

limb, neck, facial muscles, resulting in gait, swallowing and breathing problems, in vaccinated individuals. Early investigators were able to induce a similar encephalomyelitis in rabbits or monkeys by administering repeated injections of neural tissue, thus demonstrating that the resultant encephalomyelitis was not due to rabies, but probably resulted from the unintentional induction of an autoimmune response against neural antigens. The introduction of complete Freund's adjuvant (CFA) made induction of EAE much simpler and more reliable, improving the reproducibility. CFA consists of a mixture of mineral oil and Mycobacterium Tuberculosis made into an emulsion with the antigen, and injecting antigen in CFA usually induces a vigorous and prolonged immune response against the antigen. CFA is a powerful inducer of Th1-type (pro-inflammatory) T-cell response that is responsible for disease initiation and that secrete pro-inflammatory cytokines. However, one can induce EAE by transferring activated T cells specific for myelin components, without CFA or something similar. Thus, they obtained a relapsing-remitting course of the disease accompanied by perivascular leukocyte infiltration in acute lesions and gliosis in chronic lesions, both reminiscent of MS pathology. Since then, many experimental models have been developed in different species and with different CNS antigens.

Blood Brain Barrier dysfunction in EAE

Blood-brain barrier dysfunction is involved in many different neurodegenerative diseases and has long been recognized as an important early feature of multiple sclerosis (MS). During infiltration of immune cells and lesion formation, blood-brain barrier is disrupted, or modified, in such a way that there is a dramatic increase of its permeability; function becomes compromised and vascular leakage with alteration at the junctional level occurs [29, 30]. In the EAE models, the compromised barrier has been associated with infiltration of T cells – pathological immune cell type in both MS and EAE - which extravasate into CNS, where they go towards because of their specificity for myelin antigens and undergo further activation [31]. In 2D analysis, extravasation from CNS blood

vessels, in particular capillaries, has been detected most appropriately in mice upon intravenous injection of immunofluorescent material and appears in optical fluorescence microscopy as "clouds" of material diffusing in the parenchyma [32]. Further analyses on EAE tissues show that alterations of blood barrier and of its environment can be detected at very early stage of the disease: perivascular astrogliosis which coincides with abnormalities in the junction protein expression and astrocyte activation are present before the onset [33]. The disruption of the BBB is greatest at the EAE onset, followed by inflammation and demyelination, indicating that the increase in permeability precedes the destructive inflammatory process [34]. The differential permeability in the different regions of the CNS could play a role in the progression of EAE which has been shown to be more prominent and to occur earlier at the distal spinal cord which is the more permeable region [35].

1.3 Neuroimaging as biomarker for neurodegenerative diseases

In recent years, neuroimaging was increasingly used as a biomarker in neurological disorders.

Imaging provides information on structures, functions, metabolites and allows estimates of receptors or molecular densities. The principal techniques for the whole brain imaging involved in the study of neurodegenerative diseases are magnetic resonance imaging (MRI), computed tomography (CT), functional MRI, positron emission tomography (PET), single positron emission computed tomography (SPECT) and magnetic resonance spectroscopy (MRS). Making use of these different tools, it is possible to obtain precise measures of change over time and to detect abnormalities also in presymptomatic samples.

Thanks to imaging techniques, indeed, we are able to visualize pattern of atrophy, to investigate gray and white matter (MRI), it is possible to measure the cerebral blood flow, brain metabolites, brain receptor (PET and SPECT) and the blood oxygen level dependent (BOLD) haemodynamic response in the brain (fMRI) [36].

The advantages and power of the currently available imaging techniques is clear; however, all of them show limits regarding the spatial resolution, the sensitivity or the probe penetration.

X-ray phase contrast tomography (XPCT) overcomes these limits, enabling a 3D visualization of the entire organ with a spatial resolution ranging from microns to nanometers, permitting the detection of the cells of interest in the physiological and pathological contest. XPCT is able to simultaneously visualize the cells, the vascular and the neuronal systems, together with the surrounding tissue, giving complete information about the morphology and the three-dimensionality of the sample without destroying or compromising it.

1.4 X-Ray phase contrast tomography in preclinical studies

The research in neurodegenerative diseases requires tools enabling the visualization of disease-relevant networks, such as the vascular and neuronal networks (VN and NN), and of affected cells, as well as the monitoring of treatment efficacy. The techniques currently used to investigate damage in the VN and NN at cellular level suffer from several limitations. In particular, 2D imaging (immuno-histochemistry and electron microscopy) restricts spatial coverage, entails destructive sample preparation, and is only applicable at the ex vivo level. Although jumping from 2D to 3D represented an outstanding breakthrough in the general quality of imaging and information obtained, magnetic resonance imaging, positron emission tomography, and X-ray-computed tomography fail to provide a satisfactory answer to the unmet medico-imaging needs for these diseases. Thus, MRI and PET are limited in terms of spatial resolution, and X-ray computed tomography, whilst providing 3D visualization of X-ray-absorbing tissues, fails in the analysis of soft tissues, such as the CNS. These severe limitations in 3D imaging can be overcome by the more advanced X-ray phase contrast tomography, which provides much higher resolution and contrast at cellular level also in soft tissues. XPCT makes possible the simultaneous multi-scale 3D biomedical imaging of neuronal and vascular networks, ranging from cells to brain as a whole. XPCT revolutionizes X-ray imaging and removes

its main limitation of poor image contrast arising from low attenuation differences. XPCT increases the contrast of all details and enables the detection of features classically considered as “X-ray invisible”. A key ability of XPCT is the possibility to generate a 3D multiscale image of the whole brain, which displays information on the NN and VN simultaneously [37-43]. In previous works [44, 45], we exploited this unique feature of XPCT to evaluate morphological alterations in the VN and NN, both in EAE and in the APP/PS1dE9 mouse model of Alzheimer’s disease.

1.4.1 XPCT for brain imaging

The ambitious objective to explore the CNS from the whole organ down to the single cell through a detailed 3D imaging, whilst preserving tissue chemistry and structure, can nowadays be achieved through XPCT. Its most compelling achievement is the possibility to investigate the highly complex VN and NN in the context of the tissue as a whole and, therefore, compare physiological vs. pathological states at the level of crucial disease targets [46-48].

In order to explore the complexity of the tissue, standard X-ray tomography of the brain requires the application of contrast agents, as shown in Figure 1.2 A. As can be seen, the difference in contrast between the cortex and the thalamus is clear, and the corpus callosum and the mammillothalamic tract are well defined. However, despite the use of contrast agents, little information can be extracted on nerve cells in the cortex and on nerve fibers (Figure 1.2 A). Contrary to standard X-ray tomography, the contrast in the XPCT images is not proportional to the X-ray attenuation inside the sample but is proportional to the refraction of the X-ray beam crossing the sample. Since in the biomedical samples the refraction coefficient can be 1000 times higher with respect to the absorption one, XPCT is a unique 3D technique able to image low-absorbing tissues. Figure 1.2 shows the same anatomic district imaged with conventional absorption-based X-ray tomography using iodine and methanol as contrast agent (Figure 1.2 A) and with XPCT (Figure 1.2 B), with no use of contrast agent. The richness of details in this case is quite impressive with respect to Figure 1.2 A. Even though

a contrast agent was not used, the vascularization in the cortex clearly appears, and the cells and fibers are imaged with optimal contrast.

Figure 1.2 The image shown puts together parts of naïve mouse brain with the left side assessed by standard X-ray micro-tomography with a mixture of 1% iodine and 90% methanol as contrast agent (A) as reported in Zikmund et al. (2018) JINST 13 C02039, while the right side was generated by XPCT without contrast agent(B). Small variations in density appear much more evident in XPCT imaging. Both images were obtained as z-projections of maximum intensity over 300 μm.

Figure 1.3 shows XPCT of a naïve mouse brain region where the VN and NN are virtually extracted. Figure 1.3 B presents a detail of the vascular network, while a zoomed image of the small capillary network obtained through holo-nano-XPCT is shown in Figure 1.3 C. In the latter image, holo-nano-XPCT distinguishes two different types of cells: the black-appearing cells at the capillary walls, which are compatible with endothelial cells, and cells surrounding the capillary, which display a white cytoplasm and a dark nucleus. Figure 1.3 E shows the hippocampal NN, while Figure 1.3 F displays a magnification of the tissue where a cell with typical pyramidal neuron morphology with dark cytoplasm, and surrounded by round cells, is clearly defined.

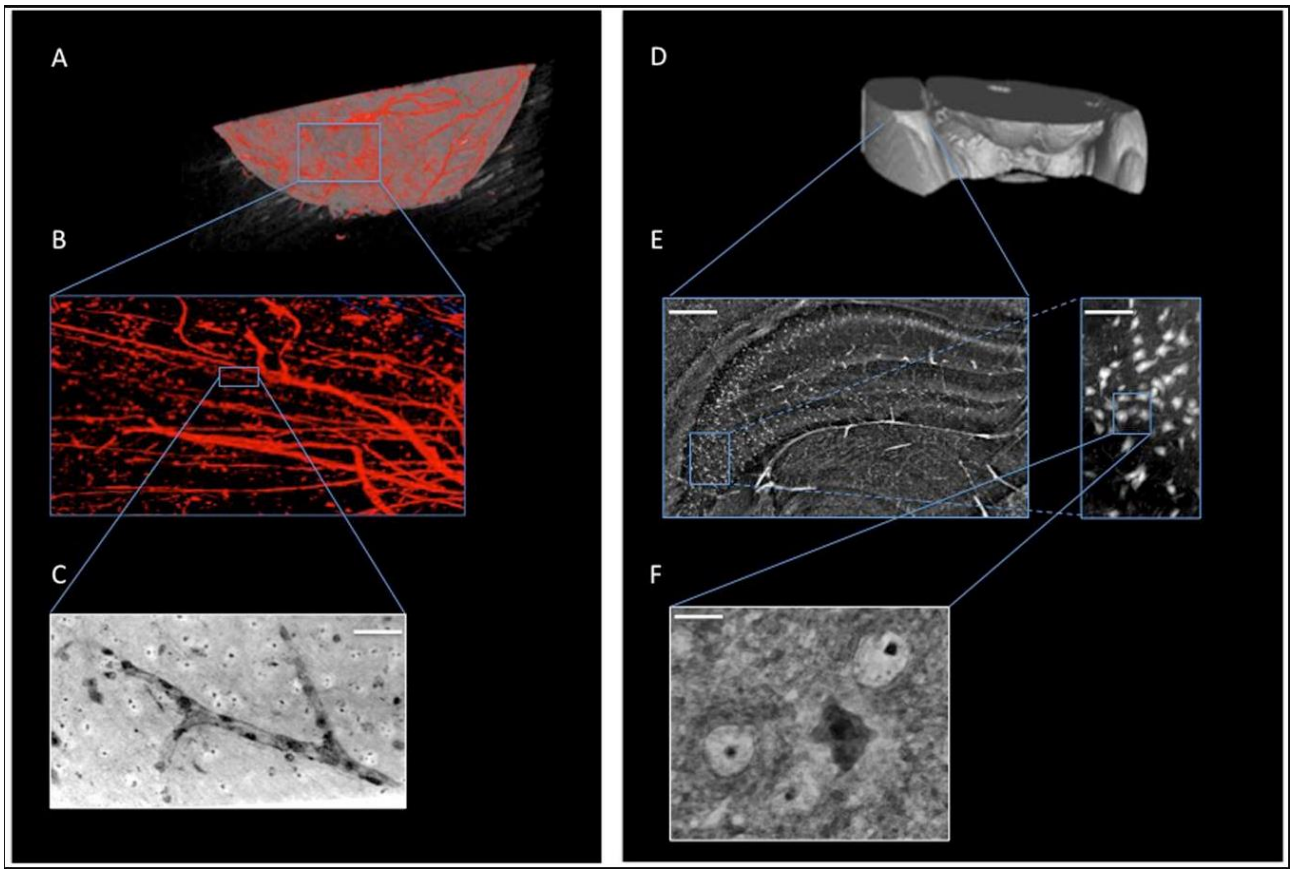

Figure 1.3 (A,B) 3D-rendering of naïve mouse brain vasculature (in red). (C) Holo-nano-XPCT image of a single capillary scale bar 50 µm. (D–F) XPCT images showing the multiscale approach to analyze the neuronal network down to the single cell; (E) Inset of (D) showing a micro-XPCT detail of brain in the hippocampal region (scale bar 250 µm) and a magnification (scale bar 80 µm) demonstrating the ability of micro-XPCT to go down to cell level; (F) Holo-nano-XPCT image highlighting the ability of XPCT to distinguish different cell types within the tissue. Scale bar 10 µm. Images acquired at ID16, ESRF by me and Tomalab group.

Selected results of the application of XPCT to neurodegenerative diseases produced by our team

The characteristics of the XPCT described above are dramatically important when study the different morphological aspects of neurodegenerative diseases. I report in the next few lines results of XPCT applied to Alzheimer's diseases and Multiple Sclerosis animal models (APP/PS1dE9 and Experimental Autoimmune Encephalomyelitis, respectively).

In Figure 1.4, an APP/PS1dE9 mouse brain section is shown. A large number of plaques (small bright spots) is visible in the cortex and in the hippocampus area. Holo-nano-XPCT of a plaque are showed in the insert of the figure.

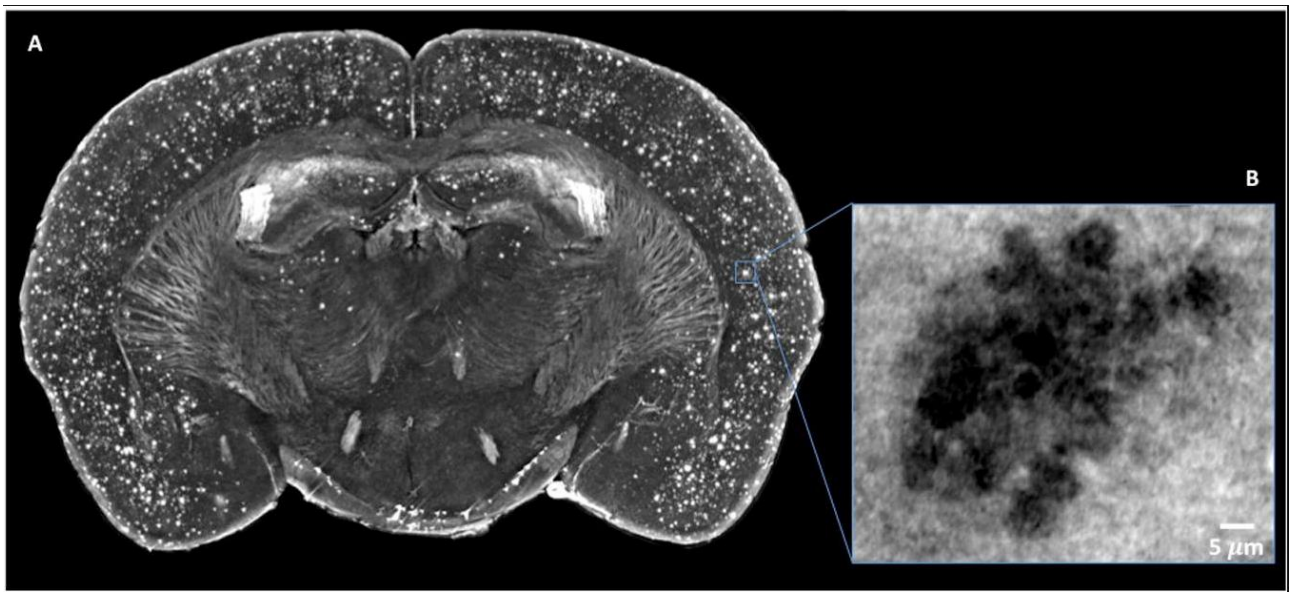

Figure 1.4 AD mouse brain clearly shows dramatic presence of Aβ deposits localized all over the cortex. Insert shows an holo-nano-XPCT magnification of a Aβ plaque in an AD mouse cortex). Images acquired by me and Tomalab group.

AD plaques deposition in the vessels can lead to an occlusion and to a consequent cerebral blood flow reduction. This situation is shown in Figure 1.5, showing intralumen plaque deposition in a capillary. In the insert, clear detection of cells with very different cytoplasm density, which might reflect the known presence of degenerated neurons (low cytoplasm density; red arrow), together with seemingly healthy neurons (high cytoplasm density; yellow arrow).

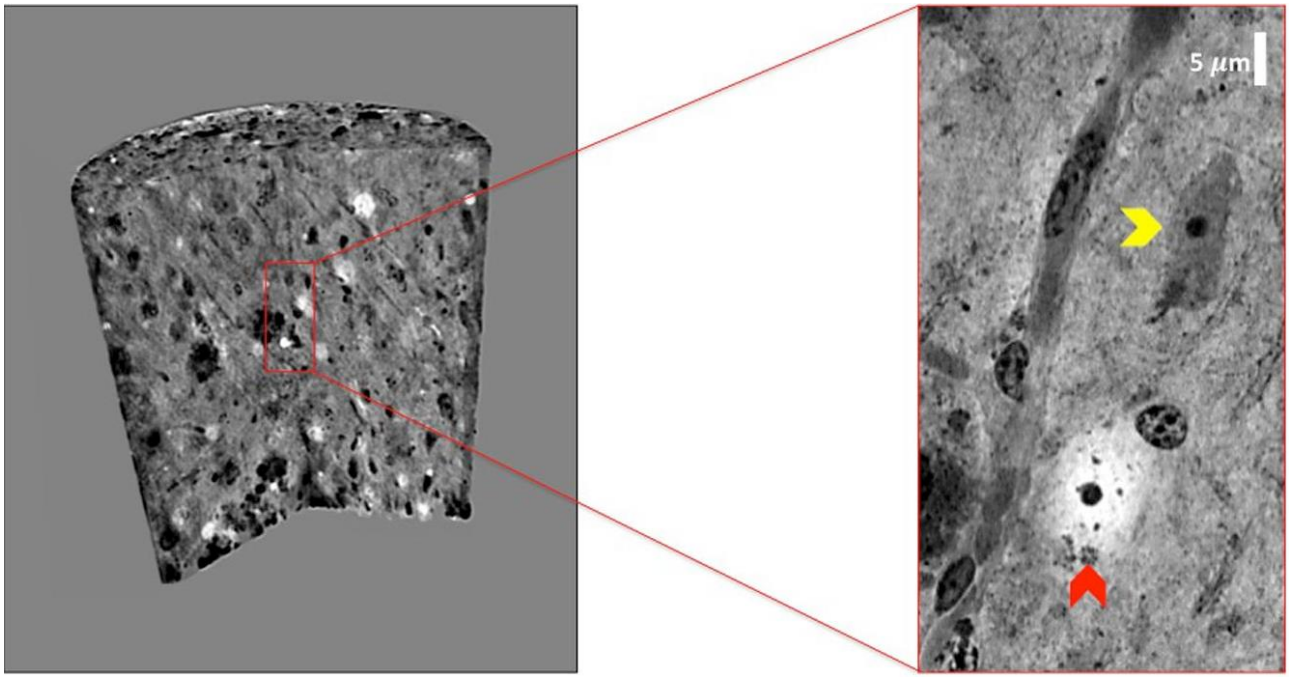

Figure 1.5 The volume of AD mouse brain tissue was rendered. The inset shows a detail of a capillary revealing the presence of intralumen plaque deposits and highlights the difference between healthy neurons featured by a dark-appearing dense cytoplasm (yellow arrow) and the degenerated ones with a low-density, white cytoplasm (red arrow). Images acquired at ID16, ESRF; by me and Tomalab group.

In Figure 1.6, images of XPCT acquisitions on a brain of an EAE mouse model. The presence of clouds of extravasated material surrounding the vessels in the spinal cord reflects the blood brain barrier (BBB) dysfunction, typical of multiple sclerosis.

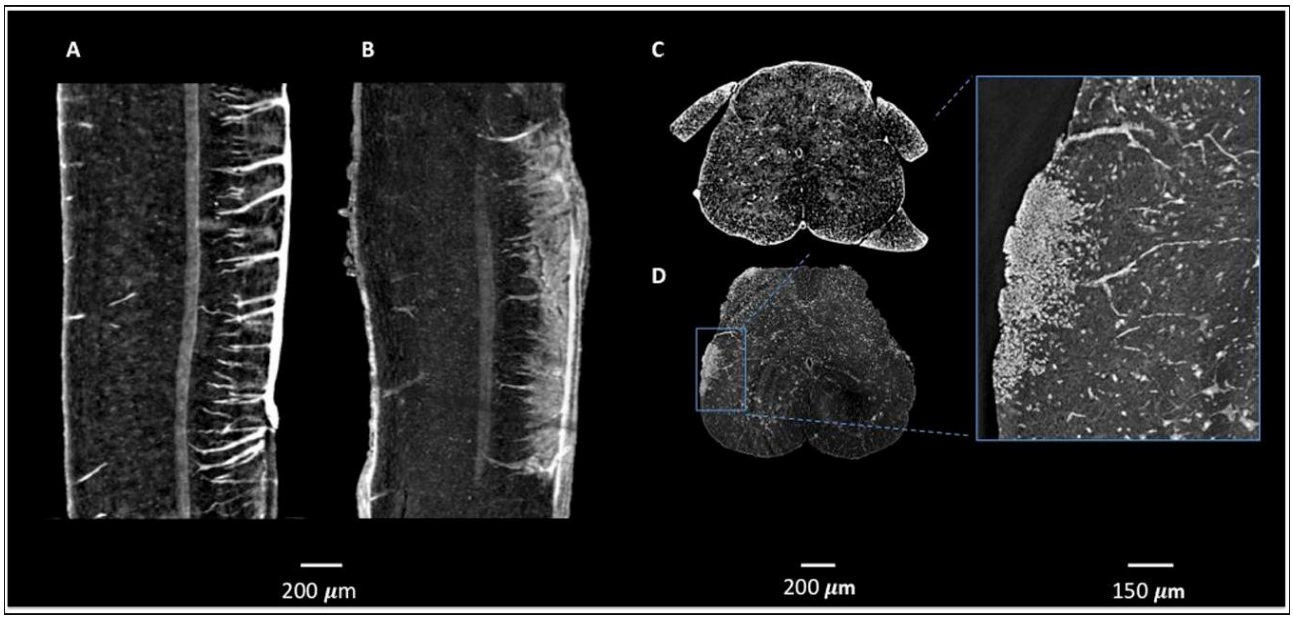

Figure 1.6 Micro-XPCT imaging of BBB leakage and lesion in lumbar spinal cord of EAE-affected mouse. (A–D) XPCT images showing the sagittal (A,B), and axial (C,D) views of the lumbar spinal cord in a naïve mouse (A,C), and an EAE-affected mouse at disease onset (B, D), where vessels appear surrounded by numerous "clouds" of extravasated material (B) reflecting the intense BBB dysfunction in the EAE-affected mouse, and the accumulation of cells around the leaky vessels (D) is commensurate with the classical EAE lesions. Images acquired by me and Tomalab group.

Materials and methods

2.1 X-ray imaging

X-rays are a form of high-energy electromagnetic radiation starting at about 0.1 keV. They have a wavelength that is shorter than visible light (<10 nm) and are capable of penetrating materials that are opaque to visible light. X-rays were discovered in 1895 by Wilhelm Röntgen, who noticed that a screen coated with a fluorescent material emitted light when exposed to a “mysterious”, invisible radiation. He named this new form of radiation as "X-rays" [49].

Nowadays, X-rays have a wide range of applications in various fields, including medical imaging, radiotherapy, industry, cultural heritage, and material science.

X-rays are ionizing electromagnetic radiation emitted by charged particles and the energy of each photon is proportional to its frequency, namely

$$E = h\nu = \frac{hc}{\lambda} \qquad (2.1)$$

where $h = 6.63 \times 10^{-34}\ Js$ is Planck’s constant, $c = 3 \times 10^{8}\ m/s$ is the speed of light, and λ is the wavelength of X radiation.

2.1.1 X-rays production

There are three common mechanisms to produce X-rays: the acceleration of a charged particle, atomic transitions between discrete energy levels, and the radioactive decay of some atomic nuclei. Each mechanism leads to a characteristic spectrum of X-ray radiation [50].

Accelerating electric charges emit electromagnetic waves. In an X-ray tube, the most common source of X-rays, a beam of high-energy electrons impacts on a solid target. As the fast-moving electrons in the beam interact with the electrons and nuclei of the target atoms, they are repeatedly deflected and decelerated. During this abrupt deceleration, the beam electrons emit the so-called “Bremsstralung”, a continuous spectrum of electro-magnetic radiation with maximum energy equal to the kinetic energy of the electron.

The total intensity of the Bremsstrahlung radiation resulting from a particle of mass m and electric charge ze incident on a target nucleus of charge Ze is proportional to

$$I \propto \frac{Z^2 z^4 e^6}{m^2} \qquad (2.2)$$

It follows immediately that the production of Bremsstrahlung radiation is the more effective the higher is the atomic number Z of the target atoms and the smaller is the mass of the incident particle. This is the reason why electrons are more efficient at generating Bremsstrahlung than a massive particle such as a proton or alpha particle.

In an X-ray tube, in addition to the continuous spectrum of radiation emitted by the decelerating electrons, there is also a spectrum of discrete X-ray emission lines that is characteristic of the target material. This “characteristic radiation” results from the excitation of the target atoms by collisions with the fast-moving electrons. Most commonly, a collision first causes a tightly bound inner-shell electron to be ejected from the atom; a loosely bound outer-shell electron then falls into the inner shell to fill the vacancy. In the process, a single photon is emitted by the atom with an energy equal to the difference between the inner-shell and outer-shell vacancy states. This energy difference usually corresponds to photon wavelengths in the X-ray region of the spectrum [51].

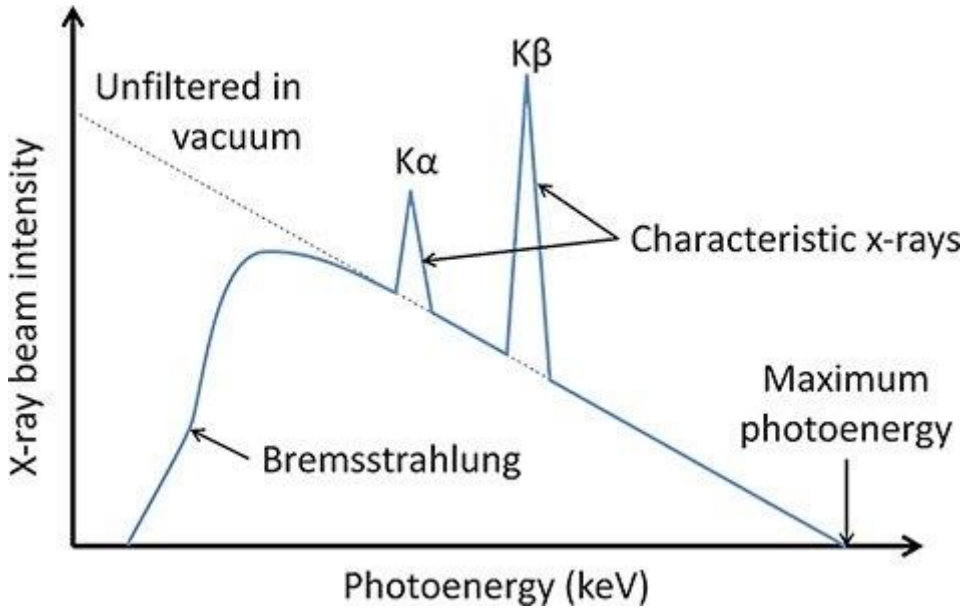

Figure 2. 1 X-ray beam production spectrum

X-ray emission is sometimes a by-product of a nuclear transformation. In the process of electron capture, an inner-shell atomic electron is captured by the atomic nucleus, initiating the transformation of a nuclear proton into a neutron and lowering the atomic number by one unit. The vacant inner-shell orbit is then quickly filled by an outer-shell electron, producing a characteristic X-ray photon. The relaxation of an excited nucleus to a lower-energy state also sometimes results in the emission of an X-ray photon [51].

2.1.2 Interaction of X-rays with matter

In the energy range of X-ray imaging (10-150 keV), the radiation can interact with matter by three mechanisms: photoelectric effect, Compton effect, and coherent scattering.

In the photoelectric effect, an incident X-photon liberates an electron from an inner shell of the atom. This phenomenon requires the energy of the photon to be greater than the binding energy of the electron. Over the binding energy, for photon energies $E_\gamma \ll m_e c^2$, where the photoelectric effect is dominant, the cross section is

$$\sigma \propto Z^5 \frac{1}{E_\gamma^3} \qquad (2.3)$$

and, therefore, is strongly dependent on the atomic number of the material. An outer-shell electron fills in the hole in the inner shell. A characteristic radiation is then emitted, with an energy equal to the difference between the binding energies of the inner and outer shell electrons. The interaction produces a positive ion, a photoelectron, and a photon of the characteristic radiation. The maximum absorption occurs when the energy of the incident photon X is almost identical to the binding energy of the electron.

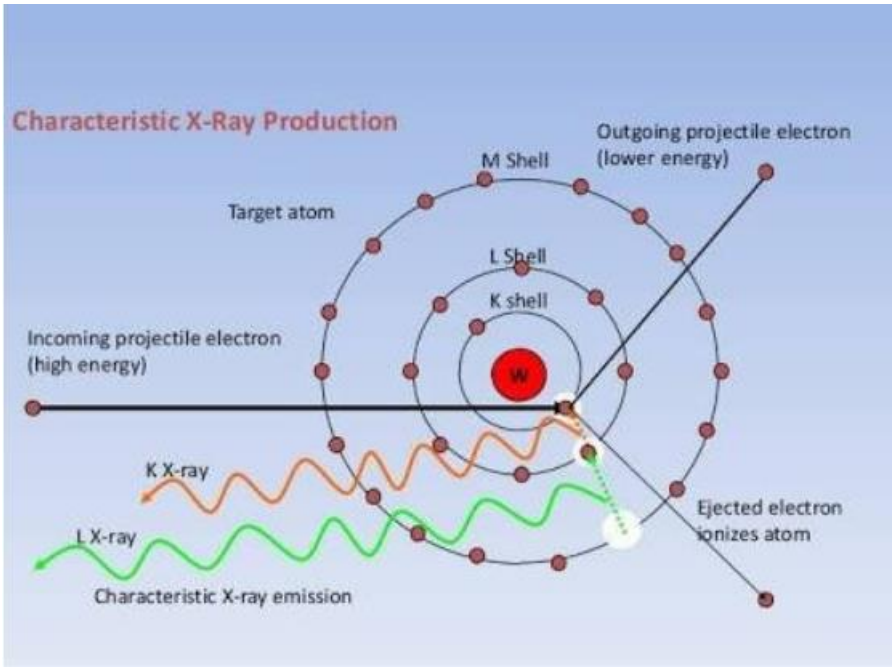

Figure 2. 2 X-Rays production scheme

The second way in which X rays interact with matter is the Compton effect (also called inelastic or Compton scattering). The photon strikes a weekly bond electron on an atom (assumed to be at rest) and the collision makes change its direction, so part of its energy is transferred to the electron. The energy loss can be calculated by considering the conservation of both energy and momentum during the interaction. As a result, the electron is ejected, and the photon is scattered with a reduced energy. Since only a small portion of the photon energy is absorbed, the energy absorbed is considerably less than the photoelectric effect. The Compton effect therefore does not generate relevant differences of contrast between different elements, since the electronic density is similar. The cross section is proportional to $\frac{1}{E_\gamma^2}$, while the cross section of the photoelectric effect is proportional to $\frac{1}{E_\gamma^3}$. In other words, the weight of photoelectric interaction decreases quickly with the increase in X-ray energy, while the Compton effect increases with the increase in X-ray energy.

Coherent scattering (also called elastic or Rayleigh scattering) occurs when the photon interacts with the whole atom, causing the oscillation of the entire electron cloud. Radiation with the same energy as that of the incident photon is emitted, and the photon changes the propagation direction.

In general, the relative contributions of these interactions vary depending on the sample material and X-ray energy.

The effect of these interactions of X-rays with the matter consists in the absorption or scattering of some incident photons. Therefore, X-ray radiation is attenuated when it passes through a material. For a monochromatic incident X-ray beam and a material of uniform density and atomic number the attenuation can be expressed by the relationship

$$I = I_0 e^{-t(a+b+c)} \tag{2. 4}$$

where I and I_0 are the incident and transmitted intensities of the beam and t is the thickness of the material; a, b, c are the attenuation coefficients of photoelectric effect, Compton effect and Rayleigh scattering of the material, respectively. This relation is also called the Beer-Lambert's law, and expressed as

$$I = I_0 e^{-\mu t} \tag{2. 5}$$

where μ is the linear attenuation coefficient of the material and t is the thickness of the material [51].

2.1.3 Refraction index

The refraction index gives information on the properties of the object to image. The index is defined as the ratio of the speed of light in vacuum to its speed in the medium

$$n = \frac{c}{v} \tag{2. 6}$$

From Maxwell equations it turns out that n satisfies the dispersion relation

$$k^2 = \frac{\omega^2 n^2}{c^2} \tag{2. 7}$$

By using (2. 6) and (2. 7), it is possible to express the refraction index in the specific case of X-ray radiation as

$$n\,(\omega) = 1 - \frac{n_a r_e \lambda^2}{2\pi} f^0(\omega) \tag{2. 8}$$

where λ is the wavelength of the radiation in the vacuum, n_a is the average density of atoms, r_e is the classical electron radius and $f^0(\omega)$ is the complex atomic scattering factor, which can be expressed as

$$f^0(\omega) = \sum_s g_s \frac{\omega^2}{(\omega^2 - \omega_s^2)^2 + i\gamma\omega} \tag{2. 9}$$

And may be written as the sum of a real and an imaginary part

$$f^0(\omega) = f_1^0(\omega) - i f_2^0(\omega) \tag{2. 10}$$

where $f_1^0(\omega)$ and $f_2^0(\omega)$ are

$$f_1^0(\omega) = \sum_s g_s \frac{\omega^2(\omega^2 - \omega_s^2)}{(\omega^2 - \omega_s^2)^2 + \gamma^2\omega^2} \tag{2. 11}$$

$$f_2^0(\omega) = \sum_s g_s \frac{\gamma\omega^2}{(\omega^2 - \omega_s^2)^2 + \gamma^2\omega^2} \tag{2. 12}$$

ω_0 is the resonance frequency of the electrons, γ is a dissipative term and g_s are the oscillator strengths, such that the sum of the oscillator strengths is equal to the atomic number Z

$$\sum_s g_s = Z \tag{2. 13}$$

The two optical constants, $f_1^0(\omega)$ and $f_2^0(\omega)$, describe two physical interactions: the phase shifts and the absorption of X-rays into the matter.

It is worth noting that, for $\omega \gg \omega_0$,

$$f_1^0(\omega) \to Z$$

(2. 14)

$$f_2^0(\omega) \to 0$$

(2. 15)

At this point, we can express the complex refraction index of X-rays passing through matter in the form generally used

$$n(\omega) = 1 - \delta + i\beta$$

(2. 16)

with

$$\delta = \frac{n_a r_e \lambda^2}{2\pi} f_1^0(\omega)$$

(2. 17)

$$\beta = \frac{n_a r_e \lambda^2}{2\pi} f_2^0(\omega)$$

(2. 18)

where δ and β are wavelength dependent.

Let us consider the propagation of a monochromatic plane wave in the sample described by

$$E_0 e^{-i\,(\omega t - k\cdot r)}$$

(2. 19)

We assume that k and r have the same direction so that $k \cdot r = kr$. The wave expression, using the dispersion relation, becomes

$$E(r,t) = E_0\, e^{-i(\omega t - \frac{\omega}{c}(1-n)r)} = E_0 e^{-i(\omega t - \frac{\omega}{c}(1-\delta + i\beta)r)} = E_0 e^{-i(\omega t - k_0 r)} e^{-ik_0 \delta r} e^{-k_0 \beta r} \quad (2.\ 20)$$

where $k_0 = \frac{\omega}{c}$ is the wave vector in vacuum, derived from the dispersion relation with $n = 1$.

We can distinguish three terms in the last part of equation 2.20:

- the first term represents the advance of the wave propagating in the vacuum;

- the second term which contains δ describes the modified phase shift due to the radiation-medium interaction. Generally, the phase shift of a wave passing through an object of a given thickness with respect to the wave freely propagating in the vacuum can be written as

$$\Delta\phi(x,y) = -\frac{2\pi}{\lambda}\int \delta(x,y,z)\, dz \quad (2.\ 21)$$

- the third term represents the decay of the wave amplitude in the medium due essentially to the photo-absorption. The amplitude attenuation can be expressed through

$$\mu_z(x,y) = \frac{1}{2}\int \mu(x,y,z)\, dz = \frac{2\pi}{\lambda}\int \beta(x,y,z)\, dz \quad (2.\ 22)$$

where μ is the *linear attenuation coefficient*, which with a reasonable approximation can be written as

$$\mu = \frac{4\pi\beta}{\lambda} \qquad (2.\ 23)$$

The integrals in are understood to be along the propagation direction z over the object.

It is clear that the interaction of the electromagnetic wave with matter affects its amplitude and phase. A visual representation is shown in Fig. 2.3. Schematic representation of what happens to a wave after interacting with an object: amplitude and phase are modified with respect to the incident wave, where two monochromatic plane waves travelling in the vacuum (black line) and in a material with refractive index n (blue line) are compared. After the wave-object interaction, the latter is longitudinally shifted (phase shift, ΔΦ) and its amplitude decreases (attenuation).

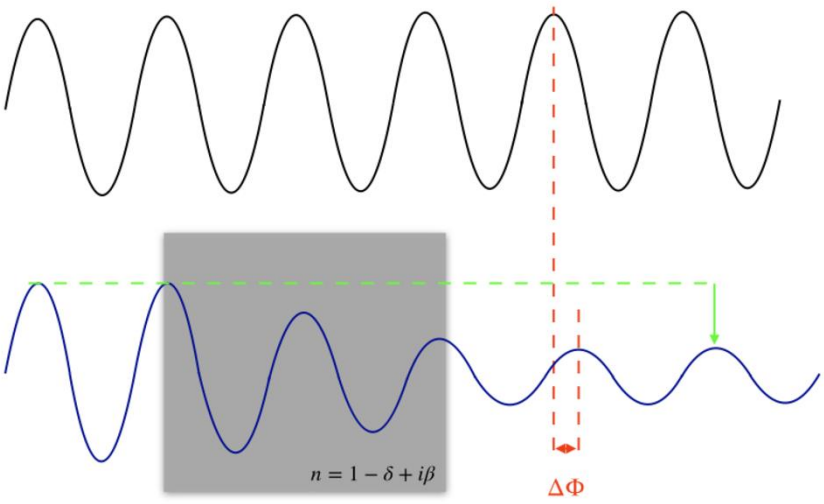

Fig. 2. 3 Schematic representation of what happens to a wave after interacting with an object: amplitude and phase are modified with respect to the incident wave.

For high energies, the absorption component β drops with energy much faster with respect to δ, since the asymptotic trends of the two terms for $\omega \gg \omega_0$ are

$$\delta(E) \propto \frac{1}{E^2} \tag{2. 24}$$

$$\beta(E) \propto \frac{1}{E^4} \tag{2. 25}$$

which can be derived from

$$\delta = \frac{n_a r_e \lambda^2}{2\pi} f_1^0(\omega) = \frac{n_a r_e \lambda^2}{2\pi} \sum_s g_s \frac{\omega^2(\omega^2 - \omega_s^2)}{(\omega^2 - \omega_s^2)^2 + \gamma^2\omega^2} \tag{2. 26}$$

$$\beta = \frac{n_a r_e \lambda^2}{2\pi} f_2^0(\omega) = \frac{n_a r_e \lambda^2}{2\pi} \sum_s g_s \frac{\gamma\omega^2}{(\omega^2 - \omega_s^2)^2 + \gamma^2\omega^2} \tag{2. 27}$$

Especially in the hard X-ray regime ($E \geq 6\ keV$), δ can be orders of magnitude larger than β. This means that the phase change of a transmitted wave can be affected much more significantly than its amplitude [51].

Since in the X-ray range the delta term is always positive and of the order 10^{-5}, n is always slightly smaller than 1. This fact implies that an X-ray beam impinging on a surface with a grazing angle smaller than a certain critical value, is totally reflected. On the other hand, for a grazing angle greater than the critical value, all the angular deviations (in absence of Bragg diffraction) will be small. However, the optical wavelength of X-rays is 10^4 times smaller than visible light and, therefore, the effect on the phase may still be appreciable and huge compared to the corresponding effect on the amplitude.

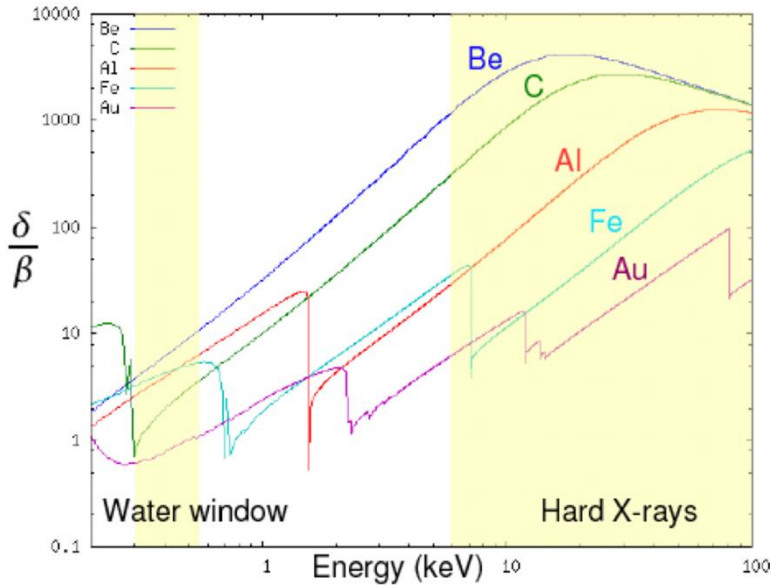

Fig. 2. 4 Ratio of the phase and the absorption components of the refractive index as a function of the energy for waves interacting with different elements.

Fig. 2. 4 shows the ratio of delta over beta of a transmitted wave as a function of energy for different elements. In the hard X-rays region, the ratio increases with energy to huge values: δ results to be greater than β up to 1000 times, in particular for light elements, which are the principal components of biological samples. These results show that, if properly exploited, a contrast imaging mechanism based on refraction can be more sensitive than a mechanism based on absorption.

2.1.4 Transmission Function

The interaction of the X-ray beam with the sample can be formalized by using the transmission function. It can be described as the ratio between the emerging field and the incident field.

First of all, we have to solve the interaction problem, that means calculating the field emerging from the object just downstream of the object plane. It is not always possible to find an exact solution, but some approximations have to be sought.

Let us introduce the *transmission function* (TF) which defines how the wave front is modified by the interaction of the incident field with the object impinged through the following linear relation

$$E_0(x,y) = T(x,y) \cdot E_{incident}(x,y) \qquad (2.\ 28)$$

where $E_0(x,y)$ is the emerging field in $z = 0$, $E_{incident}$ is the incident field and T is TF. In principle the transmission function should depend on both the sample and the incident field, so it should not be considered an intrinsic property of the object. In practice, TF is often estimated a priori and considered a function depending exclusively on the object [51, 52]. The dependence of TF from the incident field can be ignored under the *projection approximation* or *thin objects approximation*.

It is assumed that TF can be considered constant over a distance smaller than, or of the same order of, the incident field wavelength, and that every scatter inside the sample interacts only with the incident wave and not with the scattered one, i.e. that scattering effects inside the object can be neglected. We use the Born approximation ignoring multiple scattering events. The object is assumed to be sufficiently thin so that we can neglect any deviation from the straight-line propagation through the sample.

To show the solution of the equation through an analytic derivation, we have to start from that in a material the electric field $E(x, y, z, t)$ satisfies equation

$$\left(\frac{n^2}{c^2}\frac{\partial^2}{\partial t^2} - \nabla^2\right) E(x, y, z, t) = 0 \qquad (2.\ 29)$$

It is easy to verify by direct substitution that the general solution of eq. (2. 29) is a monochromatic wave of frequency $\omega = 2\pi c/\lambda$ with wavelength λ

$$E(x, y, z, t) = E_\omega(x, y, z) exp(-i\omega t) \qquad (2.\ 30)$$

Since (2. 30) is a solution of eq.(2. 29), $E_\omega(x, y, z)$ satisfies the *Helmholtz equation*

$$(\nabla^2 + k^2 n^2)\, E_\omega(x, y, z) = 0 \qquad (2.\ 31)$$

where $k = 2\pi/\lambda = \omega/c$.

For X-rays, the real part of the complex refraction index n (see equation (2. 16)) is always slightly smaller than 1, that means that the variations of X-ray propagation direction within the matter are tiny and negligible. Under these conditions, we have propagation in paraxial approximation and $E_\omega(x, y, z)$ can be written as

$$E_\omega(x, y, z) = E_0(x, y, z)exp(ikz) \tag{2. 32}$$

where z represents the wave propagation direction. The solution is

$$\frac{\partial^2 E_0}{\partial x^2} + \frac{\partial^2 E_0}{\partial y^2} + \frac{\partial^2 E_0}{\partial z^2} + 2ik\frac{\partial E_0}{\partial z} + (n^2 - 1)k^2 E_0 = 0 \tag{2. 33}$$

Since the amplitude is weakly variable in the propagation direction, the second derivative can be neglected and eq. (2. 33) becomes

$$\frac{\partial^2 E_0}{\partial x^2} + \frac{\partial^2 E_0}{\partial y^2} + 2ik\frac{\partial E_0}{\partial z} + (n^2 - 1)k^2 E_0 = \Delta_\perp E_0 + 2ik\frac{\partial E_0}{\partial z} + (n^2 - 1)k^2 E_0 = 0 \tag{2. 34}$$

where $\Delta_\perp$ is the Laplacian in the xy plane.

Eq. (2. 34) can be solved imposing the *thin objects approximation*, quoted above, which states that every element inside the specimen interacts only with the incident wave and not with the scattered one. For eq. (2. 34) this means that the effect of the transverse Laplacian $\Delta_{\perp}$ will be much smaller than that of the axial derivative δz and therefore becomes

$$2ik\frac{\partial E_0}{\partial z} + (n^2 - 1)k^2 E_0 = 0 \qquad (2.\ 35)$$

which solution corresponds to the linear relation which describes the transmission function $T(x, y)$

$$E\ (x, y, z) = T(x, y)\ E(x, y, z = 0) \qquad (2.\ 36)$$

where $E(x, y, z = 0)$ is the incident wave in the object plane and $E\ (x, y, z)$ is the wave downstream of the sample.

The transmission function is described by

$$T(x, y) = exp(ik \int \frac{n^2 - 1}{2} dz) \qquad (2.\ 37)$$

with the integral evaluated simply along the optical axis z, thanks to the *thin object approximation* [53].

Substituting $n = 1 - \delta + i\beta$ in $\frac{n^2-1}{2}$ and neglecting the second-order terms, since δ and β are extremely small in the X-rays range ($\delta \sim O(10^{-6})$ and $\beta \sim O(10^{-9})$) [54]

$$\frac{n^2 - 1}{2} = \frac{(1 - \delta + i\beta)^2 - 1}{2} \sim -\delta + i\beta \tag{2. 38}$$

Replacing equation (2. 38) in equation (2. 37)

$$T(x, y) = exp[-k \int \beta(x, y, z)\, dz - ik \int \delta(x, y, z)\, dz] \tag{2. 39}$$

Now let's recall the section concerning the refraction index, where we defined the phase shift in terms of δ and the attenuation coefficient in terms of β

$$\phi(x, y) = -\frac{2\pi}{\lambda} \int \delta(x, y, z)\, dz \tag{2. 40}$$

$$\mu_z(x, y) = \frac{1}{2} \int \mu(x, y, z)\, dz = \frac{2\pi}{\lambda} \int \beta(x, y, z)\, dz \tag{2. 41}$$

where the integrations are along the propagation axis z.

It is possible to recognize in the equation (2. 41) the phase shift and the linear attenuation coefficient. Thus, the transmission function can be rewritten in a more concise form

$$T(x,y) = e^{-\mu_z(x,y)} e^{i\phi(x,y)}$$

(2. 42)

If the object modifies only the amplitude of the incident wave and leaves unchanged the phase, then it is called an amplitude object. Instead, it is called a pure phase object, if modifies the phase and the absorption term $e^{-\mu_z(x,y)}$ is independent from x e y.

We can reduce the expression of the transmission function to a simple linear form – useful for analytic studies for the intensity - by using the weak object approximation. If the interactions imparted by the object are assumed to be sufficiently weak that $\mu_z(x,y)$ and $\phi(x,y)$ may be considered small respect to 1, we can Taylor expand the expression of $T(x,y)$ to the first order

$$T(x,y) \sim 1 - \mu_z(x,y) + i\phi(x,y)$$

(2. 43)

As discussed in the refraction index section, since for the X-rays n is always slightly smaller than 1, the interaction with matter is weak ($|1-n| \sim 10^{-6}$) and the propagation inside the sample can be considered as to be straight. To verify this condition, the lateral displacement have to be small compared to the spatial resolution r

$$\sqrt{2\delta}\tau < r$$

(2. 44)

where $\sqrt{2\delta}$ is the maximum angular deviation which occurs in case of total external reflection and where τ is the thickness of the object. Straight propagation implies that the Fresnel diffraction in the sample itself is negligible. The radius of the first Fresnel zone corresponding to propagation in the object has to be small compared to the resolution

$$\sqrt{\lambda\tau} < r$$

(2. 45)

Under this condition the effect of the three-dimensionality of the object can be neglected.

2.1.5 The Propagation Problem

As discussed above, we derived the solution to the interaction problem, i.e. we calculated the field E_0 emerging just downstream of the object, once the incident field E_i and the object are known.

After the interaction with the sample, the wave front undergoes further modifications during the propagation through free space. We will describe the propagation of the field by calculating the expression of the field E_z at any finite distance z from the object and using the Fresnel and Fraunhofer approximations.

When a wave encounters an obstacle or an aperture in its path, the phenomenon of diffraction occurs and it is associated with the deviation of the propagation trajectory. The essential features of diffraction can be explained quantitatively by using the Huygens-Fresnel principle, which states that the propagation of a light wave can be predicted by assuming that each point of a wave front acts as the source of a spherical secondary wavelet with the same frequency as the primary wave [51]. The envelope of all the secondary waves is the new wave front. Let us translate Huygens-Fresnel principle in a precise mathematical form known as Fresnel-Kirchhoff formula.

Let consider a single plane wave with amplitude

$$E_0(x, y)e^{-i(k_x x + k_y y)}$$

(2. 46)

at the plane $z = 0$ (where the object is located). The wave propagates along z axis from $z = 0$ to $z = D$ in a known manner simply acquiring a factor $e^{-ik_z D}$. Then the amplitude E_D of the plane wave at D becomes

$$E_D(x, y) = E_0(x, y)e^{-i(k_x x + k_y y)}e^{-ik_z D} \tag{2. 47}$$

The strategy to solve the propagation problem can be explained as follows: decomposing the generic field E_0 into plane waves through a Fourier expansion and exploiting the linearity of this decomposition by propagating independently each Fourier component. In practice this simply corresponds to represent E_0 in a Fourier expansion and in multiplying each plane wave of the expansion by the factor $e^{-ik_z D}$.

Following this procedure, it turns out that the propagated field is a convolution between the field E_0 at z=0 and a kernel (propagator) P_D which represents the propagation

$$E_D(r) = \iint_{\infty} dr'\, E_0(r') \iint_{\infty} e^{-2\pi i[f(r-r')]} e^{-ik_z D} df = \iint_{\infty} dr'\, E_0(r') P_D(r - r') \tag{2. 48}$$

where $r = (x, y)$ and $\underline{r} = (\underline{x}, \underline{y})$ identify points on the image and object planes respectively, $f = (p, q)$ where p and q are spatial frequencies

$$p = \frac{k_x}{2\pi} \qquad q = \frac{k_y}{2\pi} \tag{2. 49}$$

$$k_z = \sqrt{\left(\frac{2\pi}{\lambda}\right)^2 - (2\pi p)^2 - (2\pi q)^2}$$

(2. 50)

and

$$P_D(r) = \iint_{\infty} e^{2\pi i(fr)} e^{-ik_z D} df$$

(2. 51)

The expression (2. 51) can be indicated in a compact form as

$$E_D(r) = E(r) \otimes P_D(r)$$

(2. 52)

where the symbol $\otimes$ indicates the convolution operator. The field in $z = D$ can then be calculated as the convolution between the field E_0 just downstream of the object and the propagator P_D. Through this equation it is possible to determine the field at any distance D from the object interacting with the beam.

The calculation of diffracted fields, starting from the expansion in plane waves, generally implies the resolution of integrals. For many optical problems we obtain sufficiently accurate results by introducing some approximations in the diffraction integrals. Among these, the Fresnel and Fraunhofer approximations will be discussed.

Fresnel Approximation

To calculate the diffracted field at z, we express the equation (2. 48) in the useful Rayleigh-Sommerfeld form

$$E(x,y,z) = \frac{i}{\lambda}\iint_{\infty} E_0(\xi,\eta)\frac{e^{-ikd}}{d}\,cos\vartheta\; d\xi d\eta$$

(2. 53)

where

$$d = [z^2 + (x-\xi)^2 + (y-\eta)^2]^{\frac{1}{2}} \qquad\qquad cos\vartheta = \frac{z}{d}$$

(2. 54)

Now, we introduce the Fresnel approximation: the field $E_0(\xi,\eta)$ is assumed to be equal to zero outside of a region centered in the axis origin, with linear dimensions small with respect to z, and E will be calculated in a region around the position $(0,0,z)$ with linear dimensions small with respect to z. This approximation is referred to also as paraxial approximation [55]. Then it is possible to consider

$$cos\vartheta \approx 1 \;\rightarrow\; \frac{1}{d} \approx \frac{1}{z}$$

(2. 55)

You can also give an approximated form to the term d that appears in the exponential. However, since this is an oscillating function, the approximation must be done in order to neglect, in the kd argument, only the terms that give a small contribution compared to 2π. We can write d in the form

$$d = z\left[1 + \frac{(x-\xi)^2 + (y-\eta)^2}{z^2}\right]^{\frac{1}{2}}$$

(2. 56)

and use the expansion

$$(1+t)^{\frac{1}{2}} = 1 + \frac{t}{2} - \frac{t^2}{8} + \frac{t^3}{16} \dots$$

(2. 57)

to approximate d at the first order

$$d \approx z + \frac{(x-\xi)^2 + (y-\eta)^2}{2z}$$

(2. 58)

the sufficient condition to neglect the terms from the second order onwards is

$$k\left[\frac{(x-\xi)^2 + (y-\eta)^2}{8z^3}\right]^2 \ll 2\pi \rightarrow \left[\frac{(x-\xi)^2 + (y-\eta)^2}{8\lambda}\right]^2 \ll z^3$$

(2. 59)

Finally, equation (2. 53) becomes

$$E(x,y,z) = \frac{ie^{-ikd}}{\lambda z} \iint_{\infty} E_0(\xi,\eta)\, e^{-ik\frac{(x-\xi)^2+(y-\eta)^2}{2z}} cos\vartheta\, d\xi d\eta$$

(2. 60)

which represents the diffraction produced by an object in the Fresnel approximation at z. The integral is extended to the entire plane ξ, η and transverse limitations are taken into account through E_0. Equation (2. 60) still has a convolution form, where the propagator at $z = D$ is

$$P_D(x,y) = \frac{i}{\lambda z} e^{-i\pi\frac{(x-\xi)^2+(y-\eta)^2}{\lambda D}}$$

(2. 61)

In equation (2. 60) the propagator acts linearly on the field E_0 so that the propagation process has the same effect as a linear filtering. Due to this feature, the most natural treatment of the propagation is obtained in the Fourier space. Indeed, since from a mathematical point of view the convolution corresponds in reciprocal space to a simple multiplication, the field E_D measured at $z = D$ in (2. 60) can be written in reciprocal space as:

$$\tilde{E}_D(f) = \tilde{E}_0(f) \cdot \tilde{P}_D(f)$$

(2. 62)

where **f** denotes the spatial frequency conjugate to **r** and the tilde indicates the Fourier transformation.

From equation (2. 61) the propagator for Fresnel diffraction in the Fourier space can be written:

$$\tilde{P}_D(f) = e^{-i\pi\lambda D f^2}$$

(2. 63)

In the derivation, the source has been assumed to be completely coherent, i.e. there is a constant phase difference of all the secondary waves during the time of measurement. As a consequence, the intensity is simply the square modulus of the amplitude. However, this is the situation of an ideal monochromatic point source, but for any real situation the X-ray beam is only partially coherent. This means that any real source differs more or less from an ideal one because it has a spectral bandwidth and a finite spatial dimension.

Fraunhofer Approximation

We want to derive the expression of the diffracted field in the so-called *limit of far-field* or *Fraunhofer approximation* [56].

We resume the expression of r used in the Fresnel approximation

$$d \approx z + \frac{(x-\xi)^2 + (y-\eta)^2}{2z} = z + \frac{x^2 + y^2 + \xi^2 + \eta^2 - 2\xi x - 2y\eta}{2z} \tag{2. 64}$$

The presence of the terms η and ξ makes it difficult to calculate the integral (2. 60). However, it can be observed that when z tends to infinite, the terms η and ξ give a negligible contribution to the argument of the exponential function with respect to 2π. Under this condition, η and ξ are omitted and the diffraction integral takes the form

$$E(x,y,z) = \frac{ie^{-i[kz + \frac{k}{2z}(x^2+y^2)]}}{\lambda z} \iint_{\infty} E_0(\xi,\eta)\, e^{i2\pi\frac{\xi x + y\eta}{\lambda z}}\, d\xi d\eta \tag{2. 65}$$

which is the expression of the diffraction in the far-field limit. The analytic form is now particularly simple because the integral (2. 65) is the Fourier transform of E_0 calculated at $\frac{x}{\lambda z}$ and $\frac{y}{\lambda z}$.

The condition that ensures the validity of Fraunhofer's approximation is

$$k\frac{\xi^2 + \eta^2}{2z} \ll 2\pi \rightarrow \frac{\xi^2 + \eta^2}{2\lambda} \ll z \tag{2. 66}$$

From this condition the distance of transition between Fresnel and Fraunhofer diffraction region can be estimated. Assuming that the element generating diffraction is contained within a circle of radius a, the distance at which we are no longer in Fresnel but in Fraunhofer regime should be

$$z \gg \frac{a^2}{2\lambda}$$

(2. 67)

In practice, it is found that already at not very large distances from the second term the diffracted field can be described by Fraunhofer approximation. Conventionally, the critical distance of transition is assumed to be

$$z_c = \frac{\pi a^2}{\lambda}$$

(2. 68)

The order of magnitude of this distance will be taken in the following to define and distinguish the different regions of formation of the image.

Fresnel zones

Let us consider the diffraction of a plane wave propagating along z axis. A plane opaque screen with a circular aperture of radius d produces, at a generic distance z (see Figure 2.5), the usual diffraction pattern of lighter and darker rings on a screen orthogonal to the z-axis.

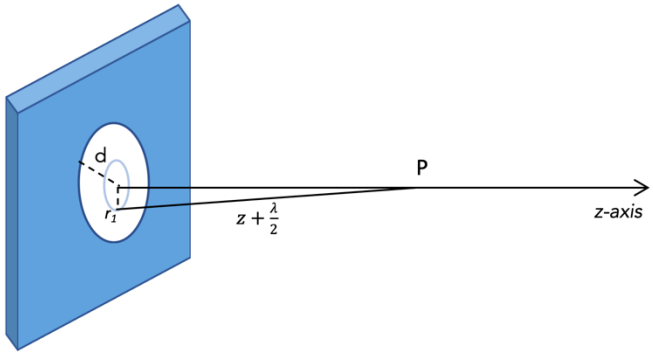

Fig. 2. 5 Visual description of Fresnel zones.

For any given point P on the z axis, it is convenient to classify the regions on the z=0 plane (where the aperture is located) depending on the constructive or destructive interference produced in P. These regions are named Fresnel zones.

The first Fresnel zone for the point P distant z from the screen is a circle of radius r_1. If $z+\frac{\lambda}{2}$ is the distance from P to the points on the circle edge, and $z \gg \lambda$, we can approximate:

$$r_1^2 = (z+\frac{\lambda}{2})^2 - z^2 \approx z\lambda \tag{2. 69}$$

The field generated by this circle in P is easily obtained in Fresnel approximation [57]:

$$W_1 = Ae^{-ikz}\left(1-e^{-i\pi}\right) = 2Ae^{-ikz} \tag{2. 70}$$

so that its amplitude is two times larger than the field amplitude in the absence of the screen. In other words, if the aperture had a radius $d=r_1$, then the whole radiation passing through it would interfere constructively in P thus explaining the increased intensity.

The second Fresnel zone is a ring of internal radius r_1 and external radius given by:

$$r_2^2 = (z+\lambda)^2 - z^2 \approx 2z\lambda \tag{2. 71}$$

where $z+\lambda$ is the distance of the points on the external circumference from P. The field produced at P by the points belonging to this second Fresnel zone is obtained by

$$W_2 = Ae^{-ikz}\left[\left(1-e^{-2i\pi}\right)-\left(1-e^{-i\pi}\right)\right] = -2Ae^{-ikz} \tag{2. 72}$$

which is the difference between the field produced by the points of a circle of radius r_2 and the field produced by the points of a circle of radius r_1, i.e. the points belonging to the first Fresnel zone.

W_2 has the same value in modulus of W_1, but has the negative sign. This means that, if the aperture had a radius $d=r_2$, the radiation from the first Fresnel zone would interfere destructively with the radiation coming from the second one and the intensity in P would vanish.

It is possible to calculate the following Fresnel zones, represented by the circles whose points are distant $z+\frac{n\lambda}{2}$ from P, with $n = 3,4,5$ ... To sum up, the radius of the general n^{th} zone is:

$$r_n = \sqrt{nz\lambda} \tag{2. 73}$$

and the field amplitude $W(z)$ along the z-axis is described by

$$W(z) = Ae^{-ikz}\left(1 - e^{-i\pi N_F}\right) = -2iAe^{-i\left(kz+\frac{\pi}{2}N_F\right)}sin(\frac{\pi}{2}N_F) \quad (2.\ 74)$$

where

$$N_F = \frac{d^2}{\lambda z} \quad (2.\ 75)$$

is the Fresnel number, which is equal to the number of Fresnel zones contained in the aperture. In particular, if this number is an even integer, the interference of the radiation from the various zones is destructive and the intensity in P is zero. If N_F is an odd integer, the radiation from one whole zone is unbalanced and the intensity is maximal.

It is important to notice that the Fresnel zones are independent on the size of the aperture and they only depend on the position of P and on the wavelength.

So far, the Fresnel zones were introduced in relation to a generic point P at distance z on the axis. Conversely, one could identify a distance on the z-axis, such that the aperture – whose generic dimension is equal to d - coincides with the first Fresnel zone [58]. This is the so-called *Fresnel distance*, described by

$$z_F = \frac{d^2}{\lambda} \quad (2.\ 76)$$

z_F is the largest distance on z at which a maximum in the field intensity occurs, as can be derived from (2. 74). Other maxima appear at smaller distances $z = \frac{d^2}{\lambda}(2n + 1)$. In this frame, z_F can be defined as the distance at which the whole object of linear dimension d contributes to diffraction.

For $z > z_F$, the intensity tends to decrease monotonously and, for z larger than the transition value $z_t = \pi \frac{d^2}{\lambda}$ derived in (2. 68) one enters the region of Fraunhofer regime.

2.1.6 Coherence

A high degree of coherence is a necessary requirement for phase contrast experiment based on propagation. For this reason, a general presentation of some basic notions about coherence and correlation is given in this section.

The most evident effect of coherence properties comes out in diffraction phenomena. Coherence is commonly defined as the ability of a field to form stable interference fringes [59].

We consider two plane harmonic linearly polarized waves of frequency ω:

$$E_1 = E_1 \, exp \, exp \, i(k_1 \cdot r1 - \omega t + \varphi_1)$$
$$E_2 = E_2 \, exp \, exp \, i(k_2 \cdot r2 - \omega t + \varphi_2) \quad (2.\ 77)$$

If the phase difference $\varphi_1 - \varphi_2$ is constant, the two sources the waves originate from are said to be mutually coherent. The electric field produced at a point in empty space by the vector sum of

$$E = E_1 + E_2 \quad (2.\ 78)$$

is also mutually coherent in this case.

The superposition of the two monochromatic plane waves, aside from a constant proportionality factor, results in the intensity function

$$I = |E|^2 = |E_1|^2 + |E_2|^2 + 2E_1 \cdot E_2 \cos\vartheta \tag{2. 79}$$

where $\vartheta = k_1 \cdot r_1 - k_2 \cdot r_2 + \varphi_1 - \varphi_2$.

The term $2E_1 \cdot E_2 \cos\vartheta$ is the interference term, which indicates that I can be greater than or less than the sum $I = I_1 + I_2$, depending on the value of ϑ. Since ϑ depends on r, periodic spatial variations in the intensity occur: they are the interference fringes which appear when two mutually coherent beams are combined. Instead, if the sources of the two waves are mutually incoherent, the phase difference $\varphi_1 - \varphi_2$ varies randomly with time. In these conditions, the mean value of $\cos\vartheta$ is zero: there is no interference.

Coherence can be both spatial and temporal:

• Two electromagnetic waves originating from two distinct points in space and propagating along the same direction are said to be spatially coherent if their phase difference does not change over time. Most sources do not produce a beam with high spatial coherence, and this is because they are real sources with finite, non-point-like extensions.

• A wave is said to be temporally coherent if there are no phase variations during its propagation. These phase variations occur because a real wave is not perfectly monochromatic, and therefore, it is composed of different frequency components that may undergo deviations, leading to changes in phase compared to the expected sinusoidal behavior of an ideal monochromatic wave. The coherence

time is defined as the time during which the wave's behavior remains predictable with a perfectly monochromatic plane wave model.

2.2 X-ray phase contrast imaging

X-ray phase-contrast imaging is an effective method that takes advantage of how X-rays change direction when they pass through different materials. This technique is especially useful for visualizing subtle details in soft tissues, which are commonly studied in the fields of biology and medicine. It is highly sensitive to even minor differences in electronic density. In recent years, there have been notable advancements in this technique, thanks to new experimental setups and improved light sources. These advancements have allowed for higher beam energy, enabling the analysis of thicker samples, shorter exposure times, and increased sensitivity [47]. As a result, phase contrast imaging has found applications in various fields, including biology, material science, industry, cultural heritage, and, most notably, the biomedical field. Numerous ex-vivo and in-vivo experiments have demonstrated the diagnostic potential of phase-contrast imaging for various pathologies, such as breast cancer, neurodegenerative diseases, and regenerative medicine for bones and cartilages. X-ray phase contrast imaging offers the ability to visualize thick and complex samples in 3D with high-contrast and spatial resolution. There are several techniques available for detecting phase contrast; in the following sections, we will delve further into the discussion of the free space propagation method [60-62].

2.2.1 Phase-Based Techniques for X-ray Imaging

An X-ray beam transmitted by an object not only undergoes attenuation but also acquires a phase shift related to the real part of the refractive index of the material. The aim of phase-based methods

is measuring the phase shift induced by the object, in order to produce a 2D (radiography) or 3D (tomography) distribution map, proportional to its electron density, which can provide a far better contrast than absorption, in the range of X-rays. The first experiments date back to the sixties, but it is since the mid-nineties that different approaches for phase-based X-ray imaging have been explored, and nowadays most of these are widely applied. It is not possible to state which is the best method in absolute terms, because each of these phase-sensitive approaches has advantages and disadvantages, that concern the way in which the information about the phase is extracted, the complexity of the experimental set-up, the requirements on the beam, the covered spatial frequency range or the amount of radiation dose delivered to the sample. For these reasons, each of the techniques we will describe has a privileged field of application, that can be medicine, biology, material science, cultural heritage preservation, and many others.

Free Space Propagation Imaging

Among the experimental methods to detect the phase variations with hard X-rays, the propagation-based approach stands out for the extreme simplicity of the set-up. It does not need any optical element, consisting only in a (partially) coherent X-ray source, the sample and a detector displaced in line with each other. On the other hand, it requires coherence properties of X-rays beams, accessible thanks to third-generation synchrotron light sources.

The propagation technique exploits Fresnel diffraction, discussed in the previous chapter. The contrast is due to the interference between the beam diffracted by the interaction with the object and the reference wave front. Unlike the interferometric methods, there is no distinct reference beam, since the beam transmitted through the object plays this role itself interfering with the perturbed wave front. The overlap between different parts of the same beam is only possible after propagation over a sufficient distance, because the angular deviations suffered by the interacting part of the wave front

are quite slight. For this reason, the detector is moved away from the sample, with respect to the case of standard X-ray imaging, when the detector (or image plane) is positioned immediately behind the sample, assuming that the X-ray wave front does not modify during the propagation from the sample to the detector. The transition between the absorption and phase imaging is obtained by changing the detector-object distance. As said above, the set-up is very simple, hence the stability requirements are easily fulfilled. The phase modulation can be reconstructed for each recorded image through phase retrieval algorithms [63, 64].

Geometrical Approximation

Variations in thickness and X-ray refractive index of the sample lead to a change of the X-ray wave front passing through the sample. In the geometrical optics approximation, the phase shift is given by

$$\Delta\phi(x,y) = -\frac{2\pi}{\lambda}\int \delta(x,y,z)\,dz \qquad (2.80)$$

where the wave front propagates along z axis. (derived in section Refraction index). Since δ is typically of the order of 10^{-6} for light materials and we deal with hard X-ray, the angular deviation of the beam interacting with the object - with respect to the direction of propagation - is usually quite small. The local propagation vector s is dependent on the gradient of the phase in the orthogonal direction to the local incident wavevector and can be written in paraxial approximation when $|\nabla\phi| \ll k$ as [64]

$$s(x,y,z) = (-\frac{\partial\phi}{\partial x}, -\frac{\partial\phi}{\partial y}, k) \qquad (2.81)$$

so that s is normal to the wave front in (x, y, z).

The angular deviation of the interacting beam with respect to the normal to the wave front can be expressed as

$$\Delta\alpha \approx |\nabla_{x,y} \int \delta(x, y, z)\, dz|$$

(2. 82)

and it thus depends on the variation of the projected refractive index perpendicular to the propagation vector k. Rapid variations in refractive index lead to large deviation of the beam from the propagation axis. The relationship between the angular deviation and the phase shift can be derived by (2. 80) and (2. 82):

$$\Delta\alpha \approx \frac{\lambda}{2\pi} \left|\nabla_{x,y} \Delta\phi(x, y)\right|$$

(2. 83)

Deviations lead to a phase shift $\Delta\phi$ of the interacting beam with respect to the rays freely propagating in the vacuum. The angular deviation is proportional to the phase gradient. The expression diverges when the ray is tangent to the interface, translating into sharp refraction contrast at the edge of the object.

The differences in optical paths produce interference and hence intensity modulations: the free space propagation allows the interference between the transmitted-deflected beam passing through the object and the unperturbed beam and it transforms phase modulations of the incident beam into amplitude modulations. By recording the intensity of the wave front sufficiently far from the sample (defocused image), the intensity variations due to refractive index and thickness variations in the sample may be detected corresponding to a form of differential phase contrast imaging.

Contrast Transfer Function

Experimentally, on the detector we measured the intensity of the field E_D, which is the square modulus of the field amplitude:

$$I_D(r) = |E_z(r)|^2 \tag{2. 84}$$

The amplitude information of the wave is readily available, while the phase information is completely lost. Hence, the main difficulty in phase contrast imaging is that the phase cannot be measured directly and therefore several indirect methods have been developed to transform phase modulations into intensity modulations.

Free space propagation solves the problem thanks to the very simple idea that the phase modulation turns into an amplitude information through propagation. In this case the (partial) coherence of the beam is a necessary condition since, illuminating the object with an incoherent source, the information about the phase is lost just after the object because the phase of the incident wave changes in a random way and the phase changes produced by the object are irrelevant.

The amplitude of the field calculated for the position z from the object interacting with the beam can be obtained from the expression

$$E_z(r) = E_0(r) \otimes P_z(r) \tag{2. 85}$$

The convolution between the field E_0 calculated at $z = 0$ and the propagator P becomes a simple multiplication in Fourier space. The propagation of the transmitted wave in free space at distance z from the object is well described in the Fresnel approximation by

$$\tilde{E}_z(f) = \tilde{E}_0(f) \cdot \tilde{P}_z(f) \tag{2. 86}$$

If we consider an incident plane wave of unit amplitude for which the approximation of weak object is valid, the amplitude of the field for the position z can be expressed by

$$\tilde{E}_z(f) = \tilde{T}(f) \cdot \tilde{P}_z(f) \tag{2. 87}$$

where $\tilde{T}$ is the Fourier transform of the transmission function

$$T(x, y) \sim 1 - \mu_z(x, y) + i\phi(x, y) \tag{2. 88}$$

The function in Fourier space is

$$\tilde{T}(x, y) \sim \delta - \tilde{\mu}_z(x, y) + i\tilde{\phi}(x, y) \tag{2. 89}$$

where δ is the delta function of Dirac.

Considering the expression of the propagator $\tilde{P}_z$ in reciprocal space

$$\tilde{P}_z(f) = e^{-i\pi\lambda z f^2}$$

(2. 90)

in the one-dimensional case the expression for the field becomes:

$$\tilde{E}_z = e^{i\pi\lambda z u^2} e^{(\delta + i\tilde{\phi} - \tilde{\mu}_z)}$$

(2. 91)

The field in Fourier space becomes:

$$\tilde{E}_z = \left(\delta - \tilde{\mu}_z \, cos \, \widetilde{cos} \, (\chi) \; - \tilde{\phi} sin(\chi) \right) + i(\tilde{\phi} cos(\chi) - \tilde{\mu}_z \, sin \, \widetilde{sin} \, (\chi) \,)$$

(2. 92)

where $\chi = \pi\lambda z u^2$.

By inverse Fourier transforming,

$$E_z = \left(1 - \mu_z \, cos \, \widetilde{cos} \, (\chi) \; - \phi \widetilde{sin(\chi)} \right) + i(\phi \, \widetilde{cos(\chi)} - \mu_z \, sin \, \widetilde{sin} \, (\chi) \,)$$

(2. 93)

Therefore, the intensity by retaining only first-order terms in ϕ and μ_z is

$$I_z = |E_z|^2 \approx 1 - 2\mu_z \, cos \, \widetilde{cos} \, (\chi) \; - 2 \, \phi \widetilde{sin(\chi)}$$

(2. 94)

which is the image plane intensity at a distance z from the sample, in the weak object approximation.

The final expression for the intensity in the Fourier field

$$\tilde{I}_z = \delta - 2\tilde{\mu}_z \cos\cos(\chi) - 2\tilde{\phi}\sin(\chi)$$

(2. 95)

and replacing the two-dimensional expression for $\chi = \pi\lambda z f^2$

$$\tilde{I}_z = \delta - 2\tilde{\mu}_z \cos\cos(\pi\lambda z f^2) - 2\tilde{\phi}\sin(\pi\lambda z f^2)$$

(2. 96)

and the field can be written

$$\tilde{E}_z = \delta - \tilde{\mu}_z \cos\cos(\pi\lambda z f^2) - \tilde{\phi}\sin(\pi\lambda z f^2)$$

(2. 97)

Finally, we obtained an expression where the attenuation and phase contributions are uncoupled; the information on the phase is no longer lost, but from the recorded intensity it is possible to recover it. The first term containing Dirac's delta function corresponds to a homogeneous background in the image, due to the direct and non-interacting beam. The second and third terms are called *amplitude* and *phase contrast transfer function* respectively. The term with the cosine describes the contribution due to absorption, while the term with the sine represents a modulation of intensity due to phase variation. The factors multiplying $\tilde{\mu}$ and $\tilde{\phi}$ are the contrast factors for amplitude and phase modulation respectively. It follows that exploiting the propagation of the wave in free space - in practice by simply moving away the detector from the sample - the phase variations due to the interaction with the object are transferred into detectable intensity modulation. Fig. 2. 6 shows both the contrasts as functions of the reduced spatial frequency $f' = \sqrt{\lambda z} f$.

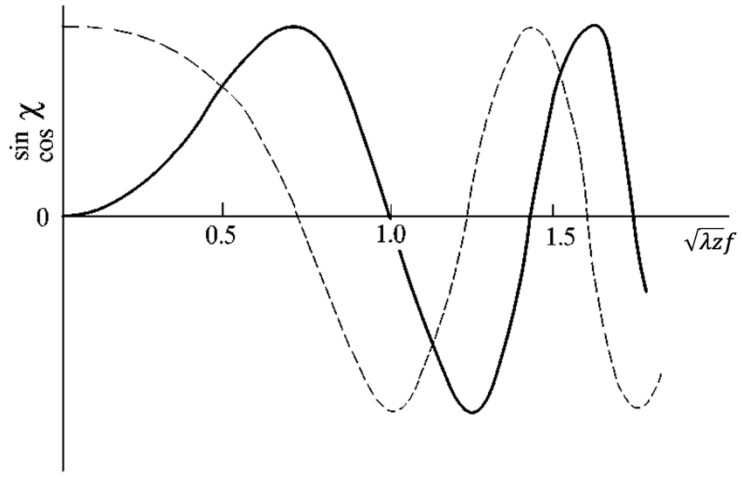

Fig. 2. 6 Absorption (dashed line) and phase (solid line) parts of the Fresnel diffraction optical transfer function as functions of reduced spatial frequency f^'=√λz f. Figure from Pogany,et al 1997[65]

Note that for $\lambda z|f^2| = 0$, which corresponds to the contact image ($z = 0$), and for $\lambda z|f^2| = 1,2,3.$., i.e. on the circles in Fourier space, the phase contrast transfer function is zero, while the absorption contrast reaches a maximum. Instead, for other positions, like $\lambda z|f^2| = \frac{1}{2}$, the situation reverses: the phase contrast is maximum, while the absorption contrast is minimum [66]. For this reason, the first value of f for which optimal phase contrast can be obtained is

$$f_{max} = \frac{1}{\sqrt{2\lambda z}} \tag{2. 98}$$

For frequencies around f_{max}, the intensity in (2. 96) can be described by

$$\tilde{I}_z(f) = \delta(f) - 2\tilde{\phi}(f)$$

(2. 99)

The condition (2. 98) on f corresponds to a distance

$$z = \frac{1}{2\lambda f^2} \approx \frac{d^2}{2\lambda}$$

(2. 100)

where a experimentally is the linear typical size of the detail to detect, and the ratio $\frac{d^2}{\lambda}$ is nothing but the so-called *Fresnel distance* D_F, i.e. the distance at which the first Fresnel zone becomes comparable to the width of the object causing the diffraction.

Region of Image Formation

The image formed on the detector, obtained as a modulation of the intensity due to absorption and phase variations, is called *defocused image*, because it is recorded out of focus, due to the propagation from the sample to the detector, as it is known in electron microscopy [67]. It is common to introduce an effective propagation distance called *defocusing distance*, which expresses the amount of defocusing, defined as:

$$D = \frac{z_1 z_2}{z_1 + z_2}$$

(2. 101)

where z_1 and z_2 are the source-sample distance and the sample-detector distance respectively.

In the case of a distant source - the incident beam can be considered a plane wave - then the distance z_1 is much larger than the propagation distance z_2 and the defocusing distance D can be approximated to:

$$D \approx z_2 \tag{2. 102}$$

As the distance D varies, different regions with different interference patterns are identified. These regions are determined with respect to a length scale defined by

$$D_F = \frac{d^2}{\lambda} \tag{2. 103}$$

where d is the typical linear size of the detail to be detected. D_F is the Fresnel distance, i.e. the distance at which the first Fresnel zone becomes comparable to the width of the object causing the diffraction. Owing to the meaning of Fresnel zone at distances $D \approx D_F$ the fields diffracted by the whole object contribute to the field in D. At smaller distances $D \ll D_F$, only an effective area of order λD contributes to the image arising from the diffracted field. On the other hand, for $D > \frac{\pi d^2}{\lambda}$ one enters the region where the diffraction can be dealt following the Fraunhofer's approximation.

Absorption

When $D = 0$, there is no wave propagation. As seen in the previous section, for this distance the phase contrast contribution is zero and there is only absorption contrast. Consequently, only the attenuation of the incident wave is measured. The expression for the intensity is reduced to

$$I = I_{in} e^{-i \int \mu(x,y) dr}$$

(2. 104)

This is the case of absorption imaging, when the detector is placed just downstream of the object, at $z_2 = 0$, to avoid blurring at the edges due to the interference.

Near-field region

The near-field regime is defined by the condition

$$\lambda D \ll d$$

(2. 105)

where d is the detail linear size. In other world we are in near-filed when the object-detector distance is much less than the Fresnel distance:

$$D \ll D_F$$

(2. 106)

Fields coming from different parts of the object do not interfere if these parts are spatially separated by more than $r = \sqrt{\lambda D}$. For weak defocusing, i.e. $r = \sqrt{\lambda D} \ll d$, only a small portion of the object of linear dimension of order r_1 contributes to the image in D. This is due to the fact that only the first

Fresnel zone contributes constructively to the image recorded. The contribution from the other regions of the object tends to cancel so that the rest of the object acts as if it were virtually opaque.

For weak defocusing, i.e. $\sqrt{\lambda D} \ll \frac{1}{f}$, the sine and cosine in (2. 97) can be expanded and the amplitude becomes:

$$\tilde{E}_z(f) = \delta(f) - \tilde{\mu}_z(f) - \pi\lambda z f^2 \tilde{\phi}(f)$$

(2. 107)

The expression of the intensity in terms of D in real space under weak defocusing conditions is

$$I_D(x,y) \approx I_0(x,y)\,[1 - \frac{\lambda D}{2\pi}\nabla^2_{x,y}\varphi]$$

(2. 108)

where $I_0(x,y)$ is the intensity of the field just downstream the object.

We derived the expression with the following passages. In reciprocal space the propagator $\tilde{P}_D(f)$ for Fresnel diffraction can be approximated as

$$\tilde{P}_z(f) \approx 1 - i\pi\lambda D f^2$$

(2. 109)

The amplitude of the field at distance D is

$$\tilde{E}_D(f) \approx \tilde{E}_0(f)\,(1 - i\pi\lambda D f^2)$$

(2. 110)

where $\tilde{E}_0(f)$ is the field in the reciprocal space just downstream the object.

In the direct space

$$E_D(x,y) \approx E_0(x,y) + i\frac{\lambda D}{4\pi}\nabla_{x,y}^2 E_0(x,y) \quad (2.\ 111)$$

The intensity can be expressed as

$$I_D = |E_D(x,y)|^2 \approx |E_0(x,y)|^2 - \frac{\lambda D}{2\pi} Im\left[E_0 \nabla_{x,y}^2 E^*\right] \quad (2.\ 112)$$

Since $|E_0(x,y)|^2 = |T(x,y)E_{inc}(x,y)|^2 = T^2(x,y)\,|E_{inc}(x,y)|^2 = |A(x,y)e^{i\varphi}|^2\, I_{inc}$, where $A(x,y)$ and $e^{i\varphi}$ are the absorption and phase term, respectively, and V_{inc} is the field incident on the sample, the intensity can be written as

$$I_D \approx I_{inc}A(x,y)^2\left[1 - \frac{\lambda D}{2\pi}\nabla_{x,y}^2\varphi\right] - I_{inc}\frac{\lambda D}{2\pi}(\nabla_{x,y}^2 A(x,y)^2 \nabla_{x,y}\varphi) \quad (2.\ 113)$$

If $A(x,y)$ varies slowly compared to φ, the last term in the expression can be neglected, giving the equation (3.29), where

$$I_0 = I_{inc}A(x,y)^2 = I_{inc}e^{-\int \mu(x,z)dz} \quad (2.\ 114)$$

Equation (2. 108) shows that the defocusing does not practically affect the absorption image and the contrast increases linearly with D. Secondly, the wavelength appears only as a separable factor so that the geometric features of the contrast are wavelength independent. This means that polychromatic radiation could equally well be used, leading to a strong phase contrast, by replacing λ by a spectrally weighted sum [64, 65, 68-71].

The total recorded intensity at distance D is a product of the term I_0, related to unfocused absorption, and a phase sensitive defocused term. The intensity for phase contrast in the near-field is proportional to the Laplacian of the phase shift and therefore it is proportional to the second derivative of the refraction index, since

$$\phi(x,y) = -\frac{2\pi}{\lambda}\int \delta(x,y,z)\,dz \qquad (2.\ 115)$$

The expression (2. 108) shows that phase contrast is sensitive to variations of the refraction index. Moreover, we derive that, to detect a contrast, the second derivative of the phase must be different from zero. We cannot detect a homogeneous phase gradient because it corresponds to an overall deflection of the beam.

Of course, the intensity above breaks down considering an object with a sharp edge because the Laplacian diverges in this case. However, the partial coherence of the real sources and the finite resolution of the detector would prevent these limitations from being observable.

In the near-field regime, the recorded image of the sample is still close to the real image (weak defocusing) but, at the same time, high contrast is given by sharp changes in the refraction index, e.g. at borders, for small particles or due to inclusions. For this reason, in the experimental condition in which the object-sample D distance respect the condition $D \ll D_F$, it should be correct to speak of edge enhancement.

Fresnel region

Fresnel regime is defined for

$$D \approx D_F = \frac{d^2}{\lambda}$$

(2. 116)

Due to the propagation effect, the image of the real sample is almost lost, and the recorded image becomes an interference pattern. This is the region in which we place the sample to perform phase contrast imaging. In fact, the optimum distance to be sensitive to phase features with typical linear size d is

$$D \approx \frac{d^2}{2\lambda}$$

(2. 117)

as derived in (2. 100).

Fraunhofer region

The Fraunhofer approximation is fulfilled for distances D from the object such that $D \gg D_F$. The larger is the defocusing distance and the more the diffracted image losses resemblance with the object. Indeed, in the Fraunhofer region, the image field has the particularly simple form of the Fourier transform of the object transmission function.

Factors Affecting Spatial Resolution

Spatial resolution is the ability of producing distinct images of two close objects. It is a measure for the smallest structure that can be reliably detected under given imaging circumstances. The main factors which affect spatial resolution are detector resolution, source coherence, and diffraction limit.

Detector resolution

The image formation on the detector is described by the *Point Spread Function* (PSF), which defines the response of an imaging system to a point source.

In a space-invariant system, i.e. where the PSF is the same in each point of the image space, the intensity distribution on the detector is the result of the convolution between the coherent intensity of the incident signal Iin with the PSF of the detector:

$$Idetector = (PSF) \otimes I_{in} \tag{2. 118}$$

that in Fourier space is

$$\tilde{I}_{detector} = (\widetilde{PSF}) \otimes \tilde{I}_{in} \tag{2. 119}$$

An ideal PSF is assumed to be Gaussian and its Fourier transform can be approximated:

$$\widetilde{PSF} = e^{(-f^2 \cdot 2(\pi\sigma)^2)} e^{(-f^2 \cdot 2(\pi w/2.35)^2)} \tag{2. 120}$$

where w describes the *full width at half maximum* (FWHM) of the Fourier transform of the PSF function.

Although real point-spread functions show very often long tails due to various effects, by defining the PSF via the FWHM of the Gaussian, the detector resolution is usually taken as:

$$r_{det} = w$$

(2. 121)

Diffraction limit

The diffraction limit is an effect introduced by the defect of focus. Since the propagation introduces interference effects, by widening the object-detector distance, the diffracted image increasingly loses its resemblance to the object. This loss of resolution depends on the amount of defocus introduced.

By using the first Fresnel zone $r_1 = \sqrt{\lambda D}$ it is possible to define a resolution limit due to diffraction. If two details in the sample are separated by a distance larger than r_1, then the beams diffracted from these two details will not interfere in the image plane located in D and they can be resolved separately. All the other details closer than r_1 produce interference in D and the diffraction fringes blur the image in the image plane.

This is the reason why usually the imaging is performed at the focus position. For example, in the case of absorption imaging - where the image directly represents the object - the detector is localized at $D = 0$ to avoid blurring at the edges due to the interference. On the other hand, the blurring arising from the interference of the diffracted beams is at the very basis of the phase contrast method which exploits the blurred (i.e. rich of fringes) interference patterns to finely reconstruct the object.

Source coherence

A non-coherent source that illuminates an object produces an image blurring because all the points of the source add up incoherently. To avoid that the coherence of the source limits the spatial resolution, the resolution due to the source coherence must be less than the detector resolution

$$w = r_{source} < r_{detector}$$

(2. 122)

Considering a source of size s at distance z_{os} from the object and defocusing distance D, the requirements turns into

$$s < \frac{z_{os}}{D} r_{detector}$$

(2. 123)

This condition becomes more and more stringent as the distance of defocusing D increases. However, it is still possible to achieve a good resolution if you increase the source-object distance z_{os} at the same time.

Coherence Requirements

The not complete coherence of the incident beam (partial coherence) has two important consequences: the spatial resolution is lowered, and the image contrast is deteriorated. In partial coherence imaging, the maximum spatial resolution that can be achieved for a given source of size s and distance z_1 from the object is defined by

$$w = \frac{sD}{z_1}$$

(2. 124)

where D is the object-detector distance.

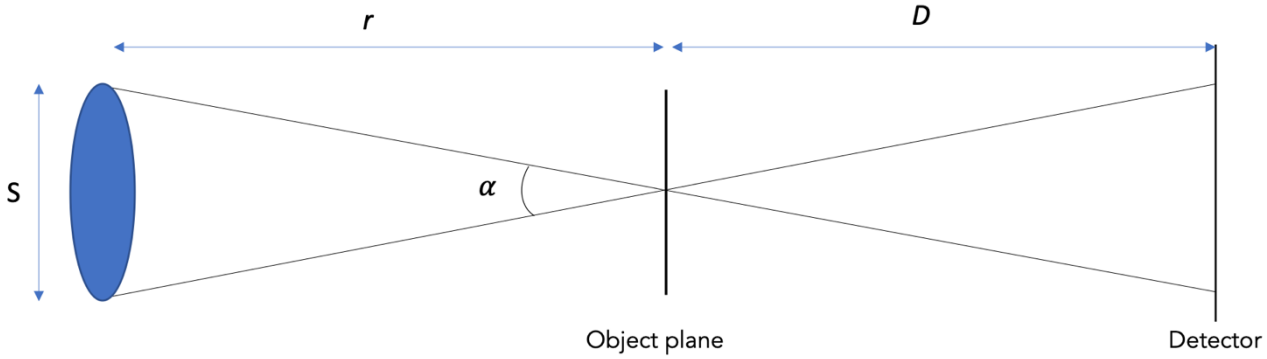

Fig. 2. 7 Blurring in partial coherence imaging.

It turns out that, as discussed in the previous section, blurring in the recorded image is reduced by moving the detector as close as possible to the object (low defocusing distance D). The phase-contrast method exploits instead the propagation and the blurring produced by the diffraction, requiring a high degree of spatial coherence, i.e. a small value for the ratio $\frac{s}{z_1}$ or a large coherence length ($l_t = \frac{r\lambda}{z_1}$).

The condition for observation of a spatial frequency f is:

$$s\frac{D}{z_1} < \frac{1}{f}$$

(2. 125)

which describes as the maximum spatial resolution must be less than the distance between the details to be resolved.

Therefore, from equation $f_{max} = \frac{1}{\sqrt{2D\lambda}}$ which describes the condition to obtain maximum phase contrast and minimum absorption we derive

$$\frac{\lambda}{\alpha} > \frac{\sqrt{D\lambda}}{\sqrt{2}}$$

(2. 126)

where $\alpha = \frac{s}{z_1}$ is the angular source size.

Therefore, it is sufficient that the beam incident on the object is coherent over the first Fresnel zone and not necessarily over the whole object.

A low degree of coherence would reduce the interference effects during the propagation so that the image contrast would result lower. Loss in contrast is more severe for higher spatial frequencies, which are normally less modulated so that very often reduced contrast results in a reduced spatial resolution.

Phase contrast imaging requires an incident beam with a high degree of coherence, which is necessary, anyway, as soon as a high-resolution is demanded. The blurring implies that the phase imaging is difficult to perform with classical X-ray sources, but the coherence request is not problematic for the third-generation synchrotron sources.

Phase Retrieval

Phase contrast imaging provides information on both absorption and refraction. However, none of the phase contrast methods does perform a direct measurement of the phase, which must be recovered numerically. Experimentally, in fact, only the intensity is directly measured and therefore it is necessary to solve the inverse problem, i.e. "recovering" the information about the phase (and the amplitude) from the measurements of recorded intensities [72]. The in-line phase contrast imaging method requires the most demanding procedure of “phase retrieval”; the advantage represented by the experimental simplicity is balanced by a more complex data processing.

There are different algorithms to recover the phase; the choice depends on the experimental conditions, such as the set-up, the propagation distance or the energy range.

For the methods that require only one image at each projection angle is possible to identify a common basic structure, as follows:

- The algorithm takes as input the intensity $I(r_\perp)$ on the image plane measured as a function of the transverse coordinates on the detector $r_\perp$.

- A function $g(I(r_\perp))$, depending on the method used, and often corresponding to a normalization, is calculated.

- $g(I(r_\perp))$ is filtered in the frequency domain. Filtering can be thought of as deconvolution of the diffraction integral. This process takes place by Fourier-transforming $g(I(r_\perp))$ and then multiplying it by an appropriate Hp(w) filter, where w are the frequency coordinates.

- The Fourier transform is inverted to obtain the quantity filtered $g_F(r_\perp)$)

- A function $f(g_F)$ is used to obtain a two-dimensional distribution of the phase on a plane immediately after the object.

For in-line phase tomography, the phase is retrieved for all images, and three-dimensional tomographic reconstruction can be performed on the retrieved phase.

The two methods for phase retrieval that I illustrate are those used to analyze the data acquired during the experiments: Paganin's algorithm has been used in case of single defocused image in free-space propagation, and multiple-distance method in case of in-line holotomography.

Multiple Distances

The contrast changes as the distance varies and the intensity generated by the absorption and by the phase propagates in different ways. Therefore, the requirement for phase retrieval of at least two intensity measurements taken at two different distances from the source allows to separate the contributions of phase and absorption. Thus, from a set of Fresnel diffraction patterns recorded at different sample-detector distances, it is possible to extract a complete quantitative information on amplitude and phase of the wave interacting with the object.

The phase retrieval for multiple-distance method that we are going to illustrate is the one described by Zabler et al. [54] for the in-line holotomography.

Let us start from the expression of the wave propagating just downstream of the object:

$$E(x, y, z = 0) = T(x, y)E_{in}(x, y)$$

(2. 127)

where $E_{in}(x, y)$ is the incident wave, propagating along z axis and $T(x, y)$ is the transmission function

$$T(x, y) = e^{-\mu_z(x,y)} e^{i\phi(x,y)}$$

(2. 128)

where we defined the phase shift $\phi(x, y)\ in\ terms\ of\ \delta$ and the attenuation coefficient $\mu_z(x, y)$ in terms of β

$$\phi(x, y) = -\frac{2\pi}{\lambda} \int \delta(x, y, z)\, dz$$

(2. 129)

$$\mu_z(x, y) = \frac{2\pi}{\lambda} \int \beta(x, y, z)\, dz$$

(2. 130)

The wave propagates over a finite distance along the z axis after the object plane.

In the Fresnel approximation, this phenomenon is described by convolution with a complex function, which we will refer to as the propagator P. We write the final expression of the wave in direct space

$$E_z(x, y) = (P_z * E(x, y, z = 0))_{x,y}$$

(2. 131)

$$P_z(x, y) = \frac{1}{i\lambda z} exp(i\pi \frac{x^2 + y^2}{\lambda z})$$

(2. 132)

$z > 0$ being the effective propagation distance $z = lD/(l + D)$ with l the source-sample distance and D the sample-detector distance. We are able to simplify this expression by writing it out in reciprocal space where the convolution integral turns into a simple multiplication

$$\tilde{E}_z(u, v) = \tilde{P}_z(u, v)\tilde{E}_{z=0}(u, v)$$

(2. 133)

where u and v are the spatial frequencies. However, the measured observable is intensity. Since in direct space intensity is calculated by $I(x, y) = |E(x, y)|^2$, in reciprocal space it becomes (considering only one dimension for simplicity)

$$\tilde{I}_z(u) = \left(\tilde{E}_z(u) * \tilde{E}^*{}_z(u)\right) = e^{-i\pi\lambda z u^2} \int_{-\infty}^{\infty} d\eta e^{i2\pi\eta u} T(\eta) T^*(\eta - \lambda z u)$$

(2. 134)

To reduce the expression to a linear relation between the Fourier transform of the phase and the Fourier transform of the recorded intensity distribution of the Fresnel diffraction images, we assume the slowly varying phase (SPV) approximation, also known as the weak-phase approximation

$$|\phi(\eta) - \phi(\eta - \lambda z u)| \ll 1$$

(2. 135)

Which implies

$$T(\eta)T^*(\eta - \lambda z u) \sim 1 + i(\phi(\eta) - \phi(\eta - \lambda z u))$$

(2. 136)

Considering the absorption negligible compared to the phase, the expression of the intensity in reciprocal space can be reduced to a linear relation between intensity and phase in reciprocal space

$$\tilde{I}_z(u) \sim \delta(u) + 2\ sin\ sin\ (\pi\lambda z u^2)\ \ \tilde{\phi}(u)$$

(2. 137)

where δ is the Dirac distribution at $u = 0$. We derived equation (2. 137) through an approximation. To minimize the error, we define the cost function in reciprocal space as a function of the difference between the experimental intensity and the result of the SVP approximation

$$S_c = \frac{1}{N}\sum_{m=1}^{N}\int du \left|\tilde{I}_{z_m}{}^{exp}(u) - \tilde{I}_{z_m}{}^{approx}(u)\right|^2$$

(2. 138)

The summation over $m = 1 \ldots N$ needs to be applied when we process N images taken at N different propagation distances $z = z_1 \ldots z_N$. We calculate the minimum of (2. 138), computing the value of $\tilde{\phi}$ for which $\frac{\partial S_c}{\partial \tilde{\phi}} = 0$

$$\tilde{\phi}(u) = \frac{\sum_m \tilde{I}_{z_m}{}^{exp}(u)\ sin\ sin\ (\pi\lambda z u^2)}{\sum_m 2(\pi\lambda z u^2)}$$

(2. 139)

Assuming a weak absorption $\mu_z(x, y) \ll 1$, we obtain an expression similar to (2. 137) with an extra cosine term for the absorption

$$\tilde{I}_z(u) \sim \delta(u) + 2\ sin\ sin\ (\pi\lambda z u^2)\ \ \tilde{\phi}(u) - 2\ cos\ cos\ (\pi\lambda z u^2)\ \ \widetilde{\mu_z}(u)$$

(2. 140)

By applying the least square minimization, this time with respect to $\tilde{\phi}(u)$ and $\widetilde{\mu_z}(u)$, finally we obtain the retrieval formulas for phase and absorption separately in reciprocal space:

$$\widetilde{\mu_z}(u) = \frac{1}{2\Delta}(A\sum_m \tilde{I}_{z_m}{}^{exp}(u)sin\,(\pi\lambda z u^2) \; - B\sum_m \tilde{I}_{z_m}{}^{exp}(u)cos\,(\pi\lambda z u^2)\,) \tag{2. 141}$$

$$\tilde{\phi}(u) = \frac{1}{2\Delta}(C\sum_m \tilde{I}_{z_m}{}^{exp}(u)sin\,(\pi\lambda z u^2) \; - A\sum_m \tilde{I}_{z_m}{}^{exp}(u)cos\,(\pi\lambda z u^2)\,) \tag{2. 142}$$

where

$$A = \sum_m sin\,(\pi\lambda z u^2)\,cos\,(\pi\lambda z u^2) \tag{2. 143}$$

$$B = \sum_m (\pi\lambda z u^2) \tag{2. 144}$$

$$C = \sum_m (\pi\lambda z u^2) \tag{2. 145}$$

$$\Delta = BC - A^2 \tag{2. 146}$$

Single distance: Paganin's Algorithm

In the case of propagation-based imaging, Paganin's algorithm allows the simultaneous extraction of phase and amplitude of the wave from a single phase-contrast image [73]. The method overcomes the

limitation of multiple-distance approach which requires at least two images to obtain information on the phase. This condition permits to speed up the processing time and reduce the complexity of the experiment. On the other hand, what we really deduce by using this algorithm is the ratio $\frac{\delta}{\beta}$ and we cannot extract separately the values for these two parameters. In other words, it is not possible to decouple the contributions due to the phase and the absorption.

Before starting to derive the expression of Paganin's algorithm it is necessary to stress that we will consider the following approximations:

- the irradiated object is considered as composed of a single material (approximation of homogeneous object), that means that absorption is proportional to phase, i.e. the $\frac{\delta}{\beta}$ -ratio is constant across the whole object;
- Fresnel approximation (or paraxial approximation) is assumed;
- the near-field regime (Fresnel number $N_F \gg 1$), i.e. short distance of propagation

Let us start from the expression of intensity transport equation, which describes the evolution of the intensity of a paraxial monochromatic wave:

$$\nabla_\perp \cdot \left(I(r_\perp, z)\nabla_\perp \varphi(r_\perp, z)\right) = -\frac{2\pi}{\lambda}\frac{\partial}{\partial z} I(r_\perp, z) \qquad (2.\ 147)$$

where $I(r_\perp, z)$ represents the intensity of the beam, $\varphi(r_\perp, z)$ the phase, λ the wavelength of the radiation. The coordinates $r_\perp$ identify the plane orthogonal to the optical axis, z is the direction of propagation and $\nabla_\perp$ the gradient in the plane containing $r_\perp$.

In first instance, to simply the discussion, we will consider the approximation of collimated beam and plane wave front, assuming the X-ray source as placed at a distance $R \to \infty$ from the object. The result will then be generalized to the case of point source.

For a normally incident plane wave radiation with uniform intensity over the object plane, we assume that the intensity of the radiation on the plane just downstream of the object ($z = 0$) can be described by the Lambert-Beer's law

$$I(r_\perp) = I_{in} e^{-\int \mu(r_\perp, z) dz} \tag{2. 148}$$

where I_{in} represents the intensity of radiation incident on the sample and $\mu(r_\perp, z)$ is the linear absorption coefficient. In this condition the phase is

$$\varphi(r_\perp) = -\frac{2\pi}{\lambda} \int \delta(r_\perp, z)\, dz \tag{2. 149}$$

where δ is deviation from the unity of the real part of the refractive index of the material whom the sample is made by.

For a homogeneous material, these equations become

$$I(r_\perp, z = 0) = I_{in} e^{-\mu T(r_\perp)} \tag{2. 150}$$

$$\varphi(r_\perp, z = 0) = -\frac{2\pi}{\lambda} \delta T(r_\perp) \tag{2. 151}$$

where $T(r_\perp)$ represents the projected thickness of the homogeneous object on the plane in which the image is acquired.

Replacing (2. 150) and (2. 151) in (2. 147) an equation non-linear in $T(r_\perp)$ is obtained:

$$I_{in}\delta\ [\ \nabla_\perp\left(e^{-\mu T(r_\perp)}\nabla_\perp T(r_\perp)\right)\ ] = \frac{\partial}{\partial z} I(r_\perp, z=0) \tag{2. 152}$$

Recognizing that

$$\left(e^{-\mu T(r_\perp)}\nabla_\perp T(r_\perp)\right) = -\frac{1}{\mu}\nabla_\perp(e^{-\mu T(r_\perp)}) \tag{2. 153}$$

it is possible to derive an equation linear in $e^{-\mu T(r_\perp)}$

$$-\frac{\delta}{\mu} I_{in}\nabla_\perp^2\left(e^{-\mu T(r_\perp)}\right) = \frac{\partial}{\partial z} I(r_\perp, z=0). \tag{2. 154}$$

It is possible to obtain the second term of the (2. 154) by using the intensity measured on two planes separated by a small distance R

$$\frac{\partial}{\partial z} I(r_\perp, z=0) \sim \frac{I(r_\perp, z=R) - I(r_\perp, z=0)}{R} = \frac{I(r_\perp, z=R) - e^{-\mu T(r_\perp)}}{R} \tag{2. 155}$$

Replacing (2. 155) in (2. 154)

$$-\frac{\delta}{\mu}R(\nabla_{\perp}^{2}+1)\left(e^{-\mu T(r_{\perp})}\right)=\frac{I(r_{\perp},z=R)}{I_{in}}$$

(2. 156)

If the image acquired in $z=0$ and the phase contrast image acquired in $z=R$ are expressed as Fourier integrals as follows

$$I(r_{\perp},z=0)=I_{in}e^{-\mu T(r_{\perp})}=\frac{I_{in}}{2\pi}\iint F(e^{-\mu T(r_{\perp})})e^{-k_{\perp}r_{\perp}}dk_{\perp}$$

(2. 157)

$$I(r_{\perp},z=R)=\frac{1}{2\pi}\iint F(I(r_{\perp},z=R))e^{-k_{\perp}r_{\perp}}dk_{\perp}$$

(2. 158)

after replacing these terms in (2. 156) then we obtain the Fourier transform

$$F\left(e^{-\mu T(r_{\perp})}\right)=\mu\frac{F(I(r_{\perp},z=R))}{I_{in}}\frac{1}{R\delta|k_{\perp}|^{2}+\mu}$$

(2. 159)

Taking the inverse Fourier transform and solving for $T(r_{\perp})$

$$T(r_{\perp})=-\frac{1}{\mu}ln\left(F^{-1}\left(\mu\frac{F\left(I(r_{\perp},z=R)\right)}{I_{in}}\frac{1}{R\delta|k_{\perp}|^{2}+\mu}\right)\right)$$

(2. 160)

which represents the solution to the intensity transport equation for a projected thickness of a homogeneous sample using an image acquired over a single distance of defocusing. Through this derivation we showed how the projected thickness is related to the phase, which depends on δ, and to the intensity, which, in turn, is function of the attenuation coefficient μ.

Rewriting the term which appears as the argument of the inverse Fourier transform

$$\left(\mu\frac{F\big(I(r_\perp, z=R)\big)}{I_{in}}\frac{1}{R\delta|k_\perp|^2+\mu}\right)=\left(\frac{F\big(I(r_\perp, z=R)\big)}{I_{in}}\frac{1}{R\frac{\delta}{\mu}|k_\perp|^2+1}\right)$$

(2. 161)

we want to point out that actually we cannot extract separately the information on phase and amplitude, but we can obtain the relation between the projected thickness and the ratio $\frac{\delta}{\mu}$ or, apart from constants and factors, the ratio $\frac{\delta}{\beta}$.

So far, we assumed that the source of X-rays is at infinite distance from the object; however, it is possible to generalize the result for the case of a point source localized at distance R_1. In particular, in paraxial approximation, we can use the Fresnel–Kirchhoff integral to derive that the plane wave intensity I_∞ can be used to express I_{R_1}, that describes the intensity due to a radiation coming from a point source at distance R_1 from the object plane

$$I_{R_1}(r_\perp, z)=\frac{1}{M^2}I_\infty(\frac{r_\perp}{M};\frac{z}{M})$$

(2. 162)

where $M=(R_1+R_2)/R_2$ is the magnification factor due to the point-like nature of the source.

R_1 is the distance of the object plane from the source, R_2 is the distance of the image plane. For $R_2 \ll R_1$ this reduces essentially to the plane-wave case. Making a substitution in 2.160

we obtain the final expression of the solution to the intensity transport equation in the case of a point source.

$$T(r_\perp) = -\frac{1}{\mu} ln\left(F^{-1}\left(\frac{F\left(M^2 I(r_\perp, z = R_2)\right)}{I_{in}} \frac{1}{R_2 \frac{\delta}{\mu} |k_\perp|^2 / M + 1} \right) \right)$$

(2. 163)

The condition of homogeneous object on which Paganin's algorithm is based on, may seem too tight. However, it can be demonstrated that for hard X-rays and biological tissues this condition is always met. It provides good qualitative results also in cases when the object is not strictly homogeneous but can be approximated as quasi-homogeneous.

To conclude, let us make a last observation. To derive the solution of the intensity transport equation as a function of the ratio of delta over beta, we considered the approximation of homogeneous object. This assumption can be seen from another point of view: instead of considering the object as made up by a single material but with an irregular lateral profile, we may think of an inhomogeneous sample of constant thickness. In these two cases the effect of the sample on the incident radiation will be the same.

2.2.2 Phase Contrast Imaging VS Absorption Contrast Imaging

By exploiting the properties of the X-rays and by using the considerations made on the absorption coefficient μ, absorption imaging has been developed. This powerful technique, which is also referred to with the term of conventional X-ray imaging, is used in industrial testing, in material science and in medicine to image local features. The absorption imaging (radiography) consists of a two-dimensional projection of the three-dimensional object obtained as a distribution map of the absorption coefficients of the material. The incident radiation amplitude is attenuated in proportion to the absorption coefficient and is recorded by a detector. Objects or features with high electron

density produce high attenuation of the incident field and bright images. On the contrary, materials with low electron density produce a smaller attenuation and result darker in the recorded image. Strong differences in electron density produce high contrast.

Absorption imaging can be performed by using a perfectly incoherent source, which makes the image only sensitive to the absorption part of the object transmission, to avoid interference effects. On the other hand, commonly absorption imaging is performed by placing the detector just downstream of the object, i.e. reducing the defocusing distance to zero, so that there is no wave propagation.

In conventional imaging the main contribution to contrast is due to photoelectric absorption. The X-rays transmitted through the object along different paths meet different absorption coefficients due to the inhomogeneities of the sample and they are differently absorbed. The emerging intensity pattern records the absorption coefficient distribution of the object and therefore it gives an image of the object itself.

In previous paragraphs it was analyzed how the absorption term decreases rapidly as the photon energy increases. The contrast obtained with the absorption is therefore limited by this trend, which becomes particularly relevant when one wants to analyze a low-absorbent object or wants to discriminate two details within the object with similar electron densities. Returning to the refractive index, it is defined as

$$n(\omega) = 1 - \delta + i\beta$$

(2. 164)

where δ and β are related to the phase shift and the attenuation respectively [74]. δ decreases slower than β as energy increases (equations (2. 24) and (2. 25)). In the hard X-ray region, the ratio δ/β increases with energy to huge values: δ results to be from 100 to 1200 times greater than β, in

particular for elements with a small atomic number Z, which are the principal components of biological samples. In the light of these considerations, in the imaging of biological samples the phase variation will be a predominant effect compared to absorption. These results show that, if properly exploited, a phase-contrast imaging is far more sensitive than a mechanism based on absorption.

X-ray imaging has been boosted by the advent of phase-contrast imaging. As said, in the conventional X-ray imaging the image contrast is generated by the absorption of radiation by the sample. On the contrary, phase contrast is due to the refraction of wave fronts that, after interacting with the sample, undergo different phase variations and interfere producing intensity modulations recorded by the detector. For this reason, phase-contrast imaging is more suitable to visualize weakly absorbing details of soft tissues, as those from biological samples, that may not be detected with absorption imaging. The phase signal is superimposed on the absorption image increasing the contrast of the contours and internal structures of the sample. The main advantage of phase contrast imaging is that, through a single image acquisition, it allows the measurement of the ratio between the two complementary signals: the phase variation and the attenuation (absorption).

The setup of the propagation-based phase-contrast imaging is identical to the absorption imaging one, except for the distance between the sample and the detector. In the case of absorption imaging, the detector is placed close to the sample, so as to exclude the effects of interference that would blur the image. On the other hand, what we exploit to obtain phase contrast is precisely diffraction, since the occurrence of contrast is due to the interference between parts of the wavefront that have suffered slightly different angular deviations associated to different phase gradients. The superposition between different wavefront parts is only possible after propagation over a certain distance. Therefore, compared to the setup configuration of absorption imaging, we move the detector away from the sample in the phase-contrast setup.

2.3 K-Edge Subtraction Imaging

K-edge subtraction is a technique that originated in the 1950s from the need to have medical x-ray imaging with acceptable radiation dose levels for patients.

This technique exploits the difference in absorption coefficient of elements at higher and lower energies than K-edge. Basically, in K-edge subtraction (KES) imaging two images are acquired at two energies bracketing the K-edge of the contrast agent used, are subtracted and, for small energy differences, the resulting image shows only the distribution of the contrast agent, canceling out the contribution of all other t issues not perfused with the contrast agent or bones.

Formally, given the two energies used (E_- and E_+), the number of photons impinging on a detector pixel is

$$N(E_\pm) = N_0(E_\pm)exp[-\sum_j(\frac{\mu}{\rho}(E_\pm)(\rho t)_j] + D$$

(2. 165)

where $N_0(E_\pm)$ is the number of incident photon per pixel, j represents the different tissues and materials, $\frac{\mu}{\rho}(E_\pm)$ the energy-dependent mass attenuation coefficient, ρ is the density of the material, t the traversed path length and D is the dark noise of the detector.

assuming the object composed of two basis materials, contrast agent and tissue, the (2.165) is linearizable by taking logarithms

$$ln\frac{N_0}{N}(E_\pm) = [\frac{\mu}{\rho}(E_\pm)(\rho t)]_{contrast} + [\frac{\mu}{\rho}(E_\pm)(\rho t)]_{tissue}$$

(2. 166)

and the mass densities can be calculated pixel by pixel using

$$(\rho t)_{contrast} = \frac{[\frac{\mu}{\rho}(E_-)]_{tissue} ln\frac{N_0}{N}(E_+) - [\frac{\mu}{\rho}(E_+)]_{tissue} ln\frac{N_0}{N}(E_-)}{[\frac{\mu}{\rho}(E_-)]_{tissue}[\frac{\mu}{\rho}(E_+)]_{contrast} - [\frac{\mu}{\rho}(E_+)]_{tissue}[\frac{\mu}{\rho}(E_-)]_{contrast}}$$

(2.167)

$$(\rho t)_{tissue} = \frac{[\frac{\mu}{\rho}(E_+)]_{contrast} ln\frac{N_0}{N}(E_-) - [\frac{\mu}{\rho}(E_-)]_{contrast} ln\frac{N_0}{N}(E_-)}{[\frac{\mu}{\rho}(E_-)]_{tissue}[\frac{\mu}{\rho}(E_+)]_{contrast} - [\frac{\mu}{\rho}(E_+)]_{tissue}[\frac{\mu}{\rho}(E_-)]_{contrast}}$$

(2.168)

Ideal case approximation involves that the tissue attenuation coefficient is the same for E_+ and E_- , reducing the (2.167) at

$$(\rho t)_{contrast} = \frac{ln\frac{N_0}{N}(E_+) - ln\frac{N_0}{N}(E_-)}{\Delta(\frac{\mu}{\rho})_{contrast}}$$

(2.169)

where $\Delta(\frac{\mu}{\rho})_{contrast}$ is the gap of the mass attenuation coefficient of the contrast agent at the absorption edge [19].

Coronary angiography is the medical application that first prompted the development of KES imaging, but, since then, there have been numerous medical fields that have benefited from this technique, such as bone growth and functional imaging [75].

This discussion is also valid for the case of L-Edge subtraction (LES) imaging.

2.4 Synchrotron radiation characteristics

The high degree of spatial coherence required by the propagation-based method makes synchrotron light the ideal source to perform phase contrast tomography experiments. In addition, synchrotron light offers many advantages, such as high intensity and brilliance, and covers a wide range of

frequencies through the electromagnetic spectrum from the infrared, through the ultraviolet, to the X-ray region, allowing also time-resolved experiments in the sub-nanosecond range.

Synchrotron radiation (SR) is an electromagnetic radiation produced when relativistic particles, such as electrons or positrons, are forced to move along a curved trajectory by an applied magnetic field [76]. Thanks to the technology achieved, it is now possible to produce a spectrum of SR ranging from infrared to hard X-rays. By virtue of its peculiarities, SR is one of the most effective tools to investigate the properties of matter in very different areas: atomic and molecular physics, biology, medicine, nanotechnology. Thanks to continuous development we have now reached the 4th generation machines.

A synchrotron machine consists of a combination of different structures. As shown in Figure 2.8.1, the principal ones are storage ring, Linac (linear accelerator), booster and beamlines. The electrons that will produce SR are firstly accelerated in the Linac and then in the booster up to the work energy. At this point they enter into the storage ring, where they circulate at a speed close to the speed of light. In the storage ring, the electrons are kept on the circular trajectory by a system of bending magnets. Each electron of the beam undergoes a Lorentz force applied perpendicularly to its velocity vector; the force does not do any work, leaving the energy unchanged, but it causes a centripetal acceleration that changes the direction of the velocity, forcing the electron to the curve trajectory. A charged particle, when accelerated, emits radiation and consequently loses part of its energy. Circulating electrons must have a constant energy to ensure their trajectory stability. The energy loss is compensated by radiofrequency cavities (RFC), which provide an energy boost and confine the beam longitudinally on their orbit by applying an electric field in phase with the passage of the charged particles.

Although bending magnets would also be X-ray sources, actually in the storage rings of the 3rd generation most of the beamlines use radiation produced by insertion devices (ID), localized along the straight sections of the ring. There are two classes of IDs: wigglers and undulators. An ID

consists of a periodic series of magnets forcing the electron to modulate a sinusoidal trajectory in the transverse direction.

The SR produced by the IDs is collected by the beamlines, constructed tangentially to the storage ring. The beamlines are physical spaces within the experimental hall consisting of an optics cabin, an experimental cabin, and a control cabin, aligned in a row. They are usually designed to be used with a specific set of techniques. The radiation provided by the accelerator is optically processed by specialized mirrors and crystal optics to focus the beam and to select the energy desired. The beam is eventually sent into the experimental cabin where it interacts with the sample being studied.

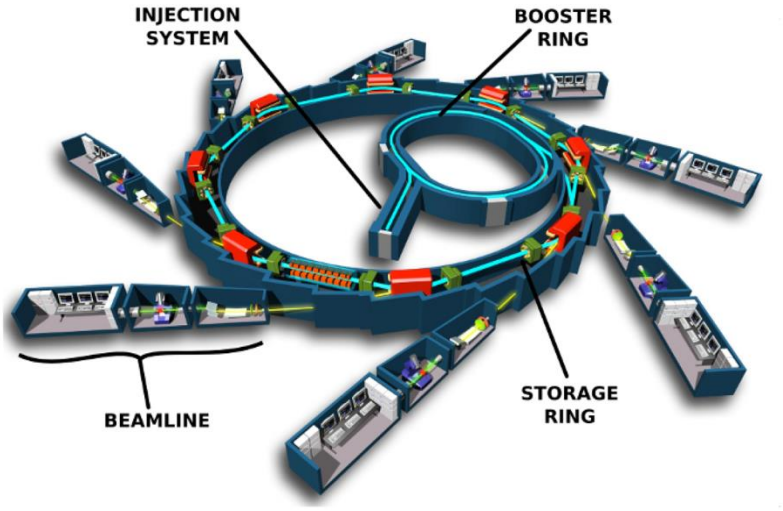

Figure 2.8.1 The principal structures of a synchrotron: injection system (Linac), booster ring, storage ring, beamlines. Image credit: "Schéma de principe du synchrotron.jpg", EPSIM 3D/JF Santarelli, Synchrotron Soleil.

2.4.1 Synchrotron Light

SR is characterized by:

- wide and continuous spectral range (from infrared to hard X-rays);
- high intensity;
- high collimation, small angular divergence of the beam;
- high brightness;
- high degree of polarization of electromagnetic radiation;

- pulsed temporal structure (ns);
- ultra-high vacuum environment where the beam is very stable.

A charged particle moving at a non-relativistic speed emits radiation with a pattern similar to that of an oscillating dipole, whose maximum intensity results in the perpendicular direction to the acceleration and does not depend on the velocity of the electron.

The equations of the synchrotron radiation emission are derived by the Lienard-Wiechert potential, that, in turn, is derived by the relativistic formulation of Maxwell's equations.

The power W emitted by a concentrated electric charge e moving at speed v along a curve trajectory of radius R, regardless the cause of the motion, is described by

$$W = \frac{2}{3}\frac{e^2 c}{R^2}\beta^4\gamma^4$$

where $\beta = \frac{v}{c}$ and $\gamma = \frac{1}{\sqrt{1-\beta^2}} = \frac{E_{el}}{m_o c^2}$ is the relativistic factor.

When the velocities result close to a significant fraction of c, due to relativistic effects the emission angles in the electron reference frame are squeezed into a narrow cone in the direction of motion, when seen in the laboratory reference frame. For relativistic velocities, the emission cone is of the order of $\frac{1}{\gamma}$, since the vertical half-opening angle is

$$\psi = \frac{E_{el}}{m_o c^2} \approx \frac{1}{\gamma}$$

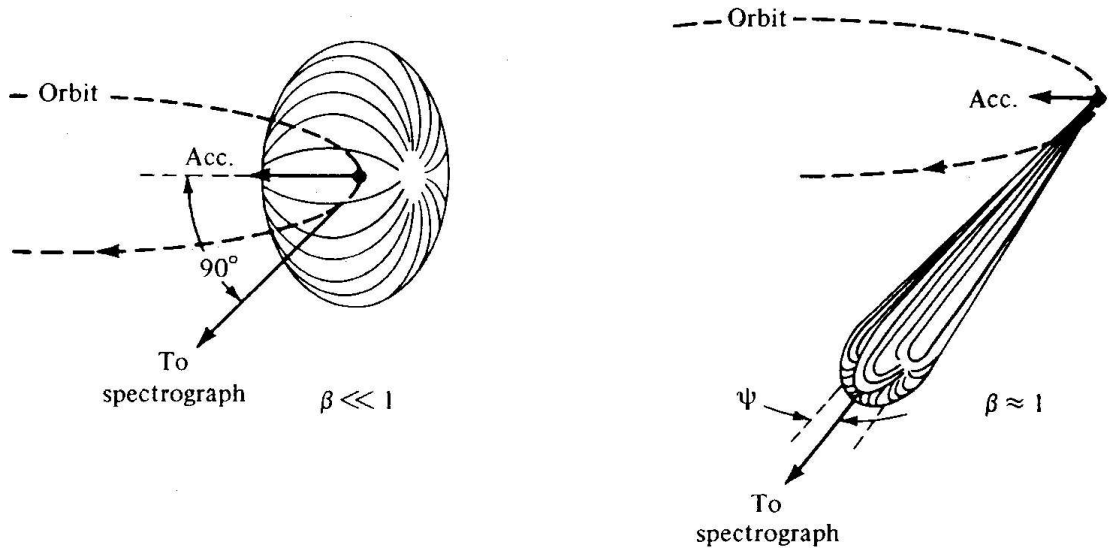

Figure 2.8. Qualitative radiation patterns related to charged particles moving in a circular orbit. The dipole pattern achieved for slow particles (left) ($\beta = \frac{v}{c} \ll 1$) is distorted into a narrow cone when $\beta \approx 1$(right). Image adapted from Mobilio and Balerna. 2003 [77].

For a typical electron storage ring with energy $mc^2 = 2\ GeV$, we have $\gamma \approx 3.9$: the collimation angle is around $0.5\ mrad$, and the beam is extremely collimated. Collimation conserves energy: the emission is concentrated in a small cone and this directly affects brightness, which is inversely proportional to angular dispersion. A collimated beam is easier to use when one wants to concentrate a strong intensity in a small area.

Brightness and Brilliance

The quality of the X-ray beam produced by an X-ray source is determined by several factors. The contributions of these quantities can be combined into a single parameter - brightness or brilliance - permitting to compare the quality of X-ray beams produced by different sources. Mobilio et al. [77] defined brightness as the number of photons per second in a spectral bandwidth $\Delta\lambda/\lambda$ = 0.1%, into a unit solid angle; brilliance is instead the number of photons emitted per second, in a spectral bandwidth $\Delta\lambda/\lambda$ = 0.1%, per unit source area and per unit of solid angle. Though their meaning is not exactly the same, often brightness and brilliance are used alternatively, also because other authors consider slightly different definitions for the two units

As reported before, brilliance is proportional to the total flux F (number of photons per second) divided by the area Σ of the source and the solid angle Ω

$$b \propto \frac{F}{\Omega\Sigma}$$

Spectral brightness is the brightness at a given wavelength band of width Δλ, corresponding to a relative bandwidth $\Delta\lambda/\lambda$

$$b_\lambda \propto \frac{F(\lambda)}{\Omega(\Delta\lambda/\lambda)\Sigma}$$

In many cases (e.g. for bending magnets, wigglers) the horizontal and vertical directions x and y are not equivalent. It is thus preferable to explicit the specific contribution of the spectral brightness of each direction:

$$b_\lambda \propto \frac{F(\lambda)}{\Omega(\Delta\lambda/\lambda)\sigma_x\sigma_y\sigma_\xi\sigma_\psi}$$

where σ_x is the beam size along x, σ_{ξ} the angular beam divergence in the plane xz, σ_y the beam size along y and σ_{ψ} the angular beam divergence in the plane xy.

The products $\varepsilon_x = \sigma_x \sigma_{\xi}$ and $\varepsilon_x = \sigma_y \sigma_{\psi}$ are the so-called *horizontal* and *vertical electron emittances* respectively for the directions x and y. The beam emittance is the distribution of particles in a bunch, constant along the ring. Therefore, a "low-emittance" source is a synonym of a source with high brightness (brilliance). While emittances are constant along the ring, beam sizes and divergences may vary [78].

2.4.2 Spectral Distribution

The spectral distribution of SR is a continuous function, extending from the X-rays to the infrared region, defined as the number of photons emitted by the electrons in the storage ring in all the vertical angles, in a band of width $\Delta\lambda/\lambda$ centered at λ while moving along an arc of length $R\Delta\theta$:

$$N(\lambda) = \frac{3^{1/2}}{2\pi}\frac{e^2}{hR}\gamma G_1 \frac{\Delta\lambda}{\lambda}\Delta\theta$$

where G_1 is known as the universal synchrotron radiation function [77].

The spectral distribution, whose representation is shown in Figure 2.9, is characterized by a critical length given by

$$\lambda_c = \frac{4}{3}\pi R \gamma^{-3}$$

The critical wavelength divides the spectrum into two parts of equal radiated power: 50% of the total power is radiated at wavelengths shorter than λ_c and 50% at wavelengths longer than λ_c.

For $\lambda \ll \lambda_c$ the spectral distribution falls off exponentially while for $\lambda \gg \lambda_c$ it decreases slowly, and it is practically independent from the energy of the electrons; its value is mainly determined by the current of the machine.

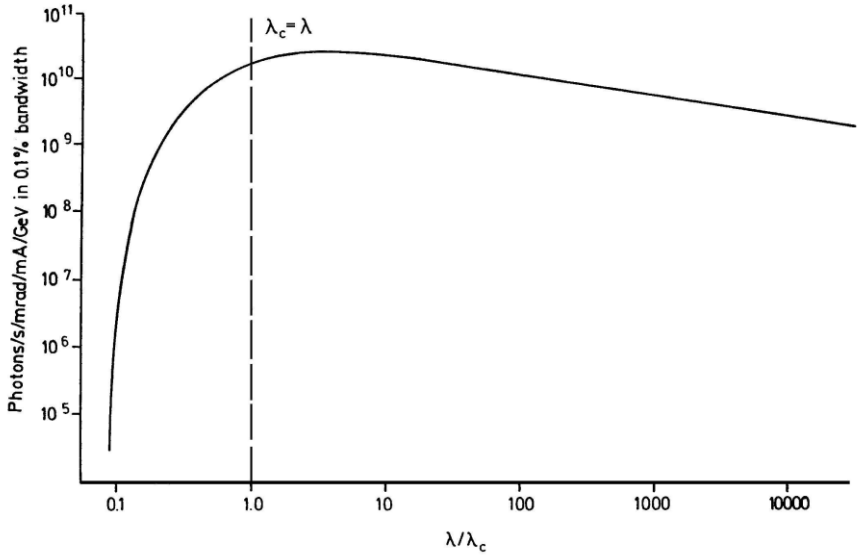

Figure 2.9. Spectral distribution of synchrotron radiation as function of λ/λ_c. Image from Mobilio and Balerna. 2003 [77]].

The photon flux is frequently expressed as a function of energy. In this case we define a critical energy as follows:

$$\varepsilon_c = 3hc\gamma^3$$

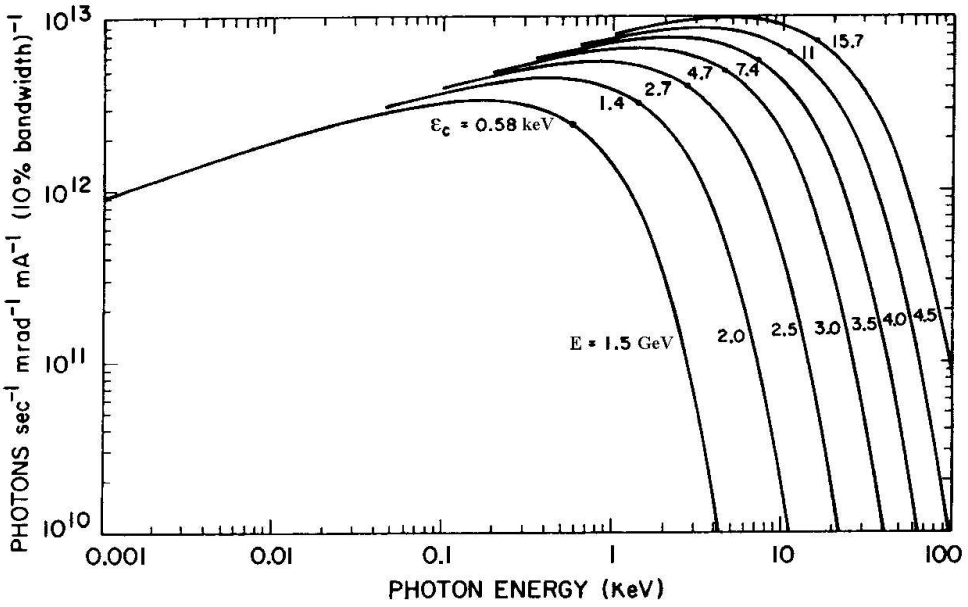

Figure 2.10. Spectral distribution of synchrotron radiation as a function of ε_c of the storage ring. Image from Mobilio and Balerna. 2003[77].

Bending Magnets

Bending magnets are also a source of SR. The system consists of 1- or 2-meter-long vacuum tube in which electrons are forced to move along a circular path by magnetic dipoles and hence they emit radiation as a result of acceleration. A fixed magnetic field is applied perpendicularly to the trajectory of the charged particle, whose acceleration and radiated power result to be

$$\frac{d\vec{p}}{dt} = e(\vec{E} + \frac{\vec{v} \times \vec{B}}{c})$$

$$P_e = \iint P(\lambda, \psi) d\lambda d\psi = \frac{2}{3}\frac{e^2 c}{R^2}\left(\frac{E}{mc^2}\right)^4$$

where λ is the wavelength of the emitted radiation, and ψ is the vertical half-opening angle perpendicular to the trajectory plane. By multiplying for the number of circulating electrons in the storage ring, the total power is obtained.

The expression of the radiated power shows that to keep the value of the parameter P within reasonable values and to increase the energy E in the storage ring it is necessary to increase the radius R of the trajectory. Considering the velocity of the electron close to c, the rotation time will be

$$T = \frac{2\pi R}{c}$$

with a loss of energy per revolution, and therefore per revolution time equal to:

$$\Delta E_e = \frac{4\pi}{3}\frac{e^2}{R}\left(\frac{E}{mc^2}\right)^4$$

In order to keep the electron energy constant, it is necessary to compensate for this energy loss by using radio frequency cavities.

The spectral distribution of a bending magnet is not an infinitely narrow peak but a band of finite width. If we analyze the peak of the emission spectrum, centered at

$$h\nu = h\gamma^2\frac{eB}{\pi m_0}$$

and we consider the pulse duration for a single electron $\delta t \approx r/(2c\gamma^3)$, according to the uncertainty principle, we can calculate the ratio between the bandwidth and the peak energy of radiation emitted by a bending magnet

$$\frac{\Delta h\nu}{h\nu_c} \approx 1$$

which shows that the emitted radiation is broadband, i.e. it includes photons with many different energies: the spectrum is continuous.

The radiation intensity is low with respect to that achievable by insertion devices.

For bending magnets the horizontal collimation is lost because the electron moves on a flat orbit, along the arc of trajectory corresponding to $\Delta\vartheta$, and the radiation is added incoherently, and then it is collected through a slit of amplitude w placed at distance D from the electron orbit and corresponding to an angle

$$\Delta\vartheta = \frac{w}{D} \gg \psi$$

Thus, the collimation of the radiation is preserved only in the direction perpendicular to the plane of the orbit.

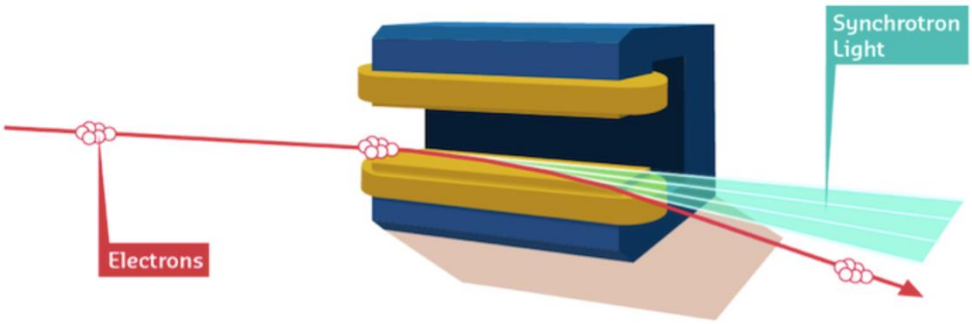

Figure 2.11. Schematic of a bending magnet. Image credit: https://www.esrf.eu/about/synchrotron-science/synchrotron.

2.4.3 Insertion Devices

The insertion devices (IDs) consist in a periodic arrangement of alternating polarity bending magnets which drive the electrons on a sinusoidal trajectory, i.e. the particles are forced to "wiggle" in the transverse direction [79]. The electrons are therefore accelerated and emit SR. The advantage of using IDs can be summed as follows:

- critical energy is moved toward higher values due to reduced radius compared to bending magnets;
- radiation intensity is increased by cumulating many sources;
- spectral brightness significantly increases.

By using IDs, it is possible to increase the brightness with respect to that achievable with bending magnets. As already earlier introduced, there are two kinds of IDs, wigglers and undulators.
IDs are inserted in the straight sections of the storage ring. We consider the case where the magnetic field *B* varies sinusoidally and is oriented in the vertical direction:

$$B(z) = B_0 cos(\frac{2\pi z}{L})$$

where *z* is the distance along the wiggler axis, B_0 the peak of the magnetic field, and L the magnetic period. The motion of the electrons is also sinusoidal and lies in the horizontal plane. A relevant parameter characterizing the motion is the *deflection parameter K* given by

$$K = \frac{eB_0\lambda_u}{2\pi mc}$$

K is the ratio of the wiggling angle of the electron trajectory over the radiation natural divergence of SR, $1/\gamma$. In terms of *K*, the wiggling angle, i.e. the maximum angular deflection of the orbit, is $\alpha = K/\gamma$. The value of K is the actual distinction between wigglers and undulators. For $K \leq 1$, radiation from the various magnetic periods can exhibit strong interference phenomena, because the angular excursions of the electrons are within the nominal $1/\gamma$ radiation cone; in this case, the ID is referred to as an undulator. In the case $K \geq 1$, interference effects are less important, and the structure is referred to as a wiggler.

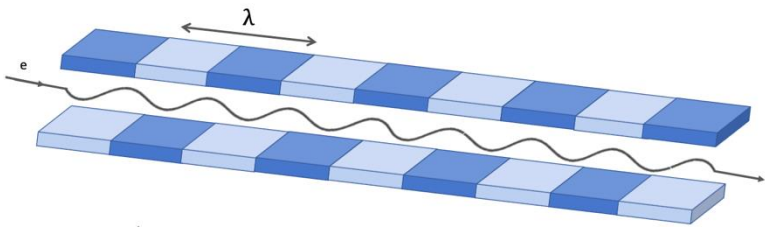

Figure 2.12 . Scheme of an insertion device. The periodic arrangement of bending magnets with alternating polarity drives the electron e- on a sinusoidal trajectory. λ is the magnetic period of the device.

Wiggler

A wiggler is a multipole magnet made up of a periodic arrangement of N magnets of period length λ_u whose magnetic field forces electrons to wiggle around the orbit. The alternating magnetic field is applied in the vertical direction, so the sinusoidal trajectory of the electron beam lies in the horizontal plane.

K is large (typically ≥ 10) because the transverse oscillations of the electrons are very large and the wiggling angle $\alpha=K/\gamma$ is much wider than the opening angle of the radiation ($1/\gamma$). It derives that radiation from different parts of the electron trajectory adds incoherently, i.e. there is no interference between the emission from different poles, and the total emission is given by the sum of the emission of the different poles. It follows that the overall characteristics of the beam are the same as those of a bending magnet with the same magnetic field but with an intensity enhanced by the factor N, the number of poles. Compared to bending magnets, the spectral distribution does not change, but the overall intensity is increased since the wiggler acts as a combination of several bending magnets. Flux and brightness scale with $2N$.

Unlike the bending magnets, the magnetic field of the wiggler and therefore the emission peak can be selected by the user. The magnetic field can be adjusted up to a maximum value, by reducing the distance between the dipoles. Moreover, in the wiggler, higher magnetic fields than those of bending magnets can be used. Therefore, the critical energy achievable is increased and the spectral range of a storage ring is extended towards higher energies.

The horizontal beam divergence is about 1 mrad, smaller than the one of bending magnets.

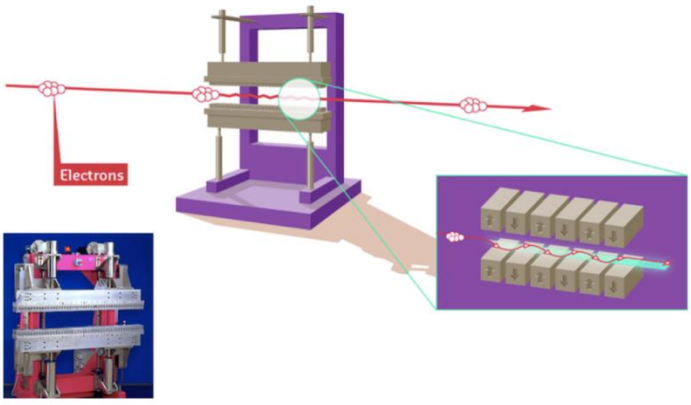

Figure 2.13. Schematic of an undulator. Image credit: https://www.esrf.eu/about/synchrotron-science/synchrotron.

Undulator

An undulator is very similar to a wiggler, i.e. it is a periodic sequence of small magnetic dipoles. As for the wriggler the radiation properties can be modified by varying the magnetic field of the dipoles by reducing the distance between them.

Unlike the wriggler, an undulator has K<1, which means that the wiggling angle is smaller than, or close to, the natural emission angle of the radiation. In this case interference occurs between the radiation emitted by the electrons at different points along the trajectory. The amplitudes of the fields radiated by each individual period of the undulator add up coherently, so the intensity increases with N^2, while in a wiggler it increases only as $2N$. Therefore, the total emitted density flux and brilliance are higher than in the wriggler.

An undulator of period λ_u causes the emission of SR with a certain wavelength. Considering the phase differences between the photons emitted at different points along the sinusoidal orbit, and observing the radiation at an angle θ from the axis of the undulator, constructive interference occurs for the wavelength described as

$$\lambda = \frac{\lambda_u}{2\gamma^2}\left(1 + \frac{K^2}{2} + \gamma^2\theta^2\right)$$

For small K the field is sinusoidal with the spectrum dominated by a single peak at the fundamental harmonic frequency. In addition to this fundamental wavelength, also higher harmonics of shorter wavelength $\lambda_u = \frac{\lambda}{n}$ are emitted. Their number and intensity increase with K; on the axis $\theta = 0$ only odd harmonics are emitted.

In terms of photon energy, the first-order energy peak is given by

$$h\nu \approx \frac{2\gamma^2 hc}{\lambda_u(1+\frac{K^2}{2}+\gamma^2\theta^2)}$$

Since K is proportional to the magnetic field through $K = \frac{eB_0\lambda_u}{2\pi mc}$, it can be derived by changing the magnetic field, for example by modifying the gap between the magnets, it is possible to tune the emission peak.

Each harmonic has a limited wavelength bandwidth approximately given by

$$\frac{\Delta\lambda}{\lambda} \approx \gamma^2\theta^2 \approx \frac{1}{nN}$$

Values of 10^{-2} for $\frac{\Delta\lambda}{\lambda}$ can be easily achieved. The relative bandwidth is such to make the undulator spectrum quasi-monochromatic. Note that the relative bandwidth is inversely proportional to the number of periods of the undulator and to the harmonic number n.

It can be demonstrated that the angular distribution of the n-th harmonic is limited in a narrow cone in both the horizontal and vertical directions. The cone aperture is smaller than the natural emission cone $1/\gamma$ of the radiation and decreases as the square root of nN.

The horizontal beam divergence is about $\frac{2}{\gamma}$; the vertical beam divergence is about $\frac{2}{\sqrt{N}\gamma}$ where N is the number of poles.

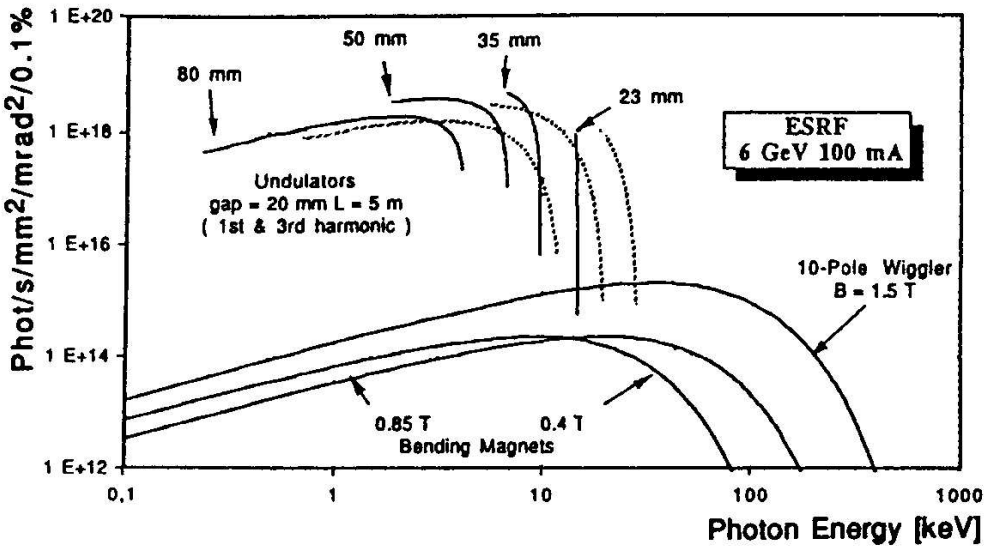

Figure 2.14. Comparison of the brilliancies of beams emitted by undulators, wigglers and bending magnets at ESRF. Image from Mobilio and Balerna. 2003[77].

2.5 X-Ray Fluorescence

X-ray fluorescence (XRF) is a non destructive technique used in different fields. It enables the elemental composition identification of the sample, useful information for a wide range of disciplines such as forensic science, archaeology, geochemistry, art projects, life science and many others. In the X-ray fluorescence technique the sample is irradiated by a high-energy primary X-ray source and emits fluorescent X-rays, also known as characteristic secondary X-rays. The interaction between the primary beam and the material causes the ejection of core-shell electrons as photoelectrons. The hole is filled by an electron from a higher-energy neighboring orbital, leading to the emission of X-ray fluorescence photons. The emitted X-rays have an energy corresponding to the binding energy difference of the two shells involved in this transition. The uniqueness of the photon energy of each element allows for efficient multi-element analysis [80].

If synchrotron light is used as the X-ray source, measurements with greater sensitivity and precision are obtained. The implementation of this technique has led to a broadening of the field of application of x-ray fluorescence, enabling accurate elemental analysis of a vast number of materials and samples [81].

2.6 Confocal microscopy

Confocal microscopy is a technique born in 1955 from an idea developed and patented by Marvin Minsky. It provides high-quality images by illuminating the sample with visible light, allowing the visualization of the details within the specimen. Compared to conventional microscopy, confocal microscopy permits the study of virtual sections without the need of mechanically slicing the sample and supplies a virtual 3D image starting from the different analyzed sections [82, 83].

An excitation beam is focused inside the sample through an objective to a small spot, light reflected or emitted by the tissue passes through the same objective and is then projected.

To avoid the phenomenon of blurring due to scattering of reflected or emitted light typical of conventional microscopy, in confocal microscopy a pinhole is introduced to select only the beam emitted from the point of interest of the sample. The pinhole is on a focal plane conjugate to that of the tissue under examination, hence the term confocal, and a photomultiplier or another light-sensitive detector is placed on the other side of the pinhole and the sample is imaged point by point.

A scheme is shown in Figure 2.15.

The focal spot is scanned in the horizontal plane and the image one pixel at a time is constructed. Thanks to the virtual sectioning, it is possible to obtain a three dimensional image of small thickness, a stack at high contrast.

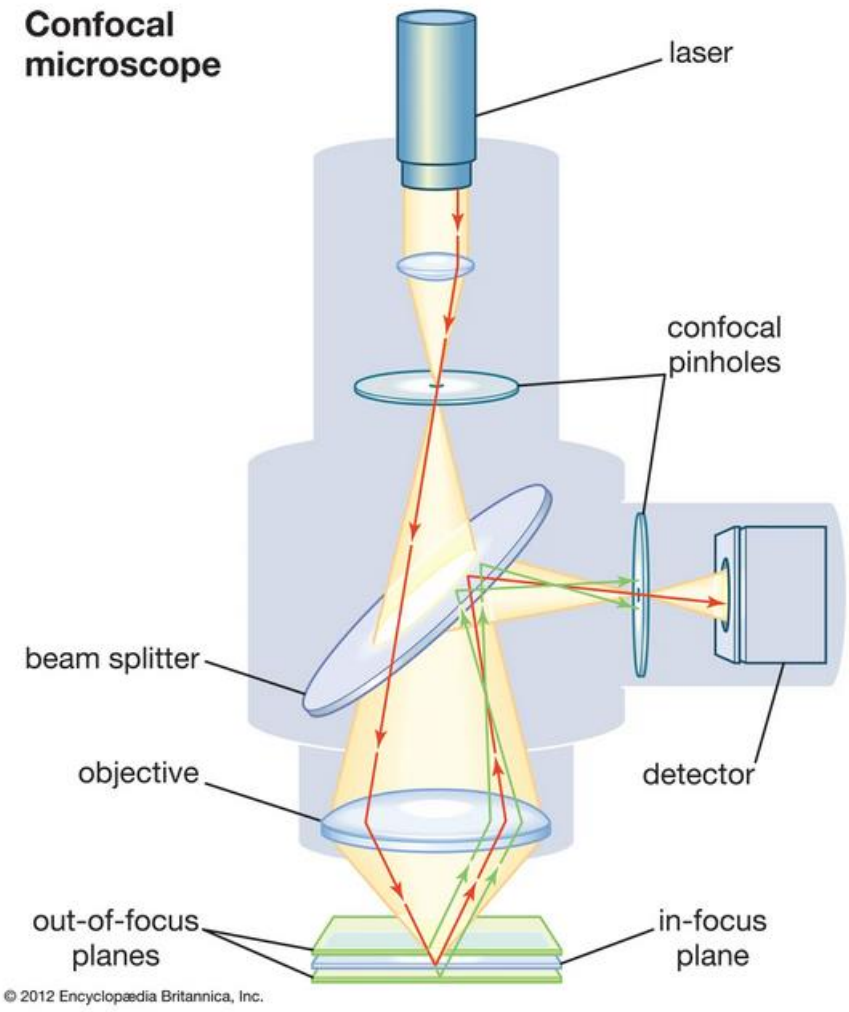

Figure 2.15 Confocal microscope scheme.

2.6.1 Fluorescence confocal microscopy

In fluorescence confocal microscopy, the incident beam, usually a laser beam, impinges on the sample to which fluorophores have been added. There are specific fluorophores for the targeting and identification of different biological components (nuclei, cytoplasm, mitochondria, etc.) and by changing the wavelength of the exciting or emitting light, it is possible to identify different fluorophores within the sample. The light from the laser and the light emitted by the sample pass

through a dichroic mirror that lets only the latter pass through to the detector. As described above, a pinhole is used to cancel out the contribution of scattered light. A limitation of fluorescence microscopy is the phenomenon of photobleaching: fluorophores tend to fade or react irreversibly when exposed to excitation light. Various strategies are being explored to minimize this problem.

2.7 Nanoparticles and binding ligands

In 1959, the physicist Richard Feynman predicted the advent of nanomaterials. In recent years, these materials with unique properties have been widely used in various fields, from biotechnology to medicine, via electronics and optics to food and agriculture [84, 85]. Among the most frequently exploited nanomaterials are nanoparticles, with dimensions typically ranging from 1 to 100 nm.

Nanoparticles can be composed of different materials, such as metal, polymers, carbon-based materials, metal-oxide, showing different optical, electrical, catalytic, thermal and mechanical properties.

In the present work, metal nanoparticles were used. This class of nanoparticles presents peculiar optical properties due to the localized surface plasmon resonance (LSPR) phenomenon, a collective oscillation of the conduction electrons in the metal nanoparticle when excited by light, leading to enhanced absorption and scattering [86, 87]. This property combined with the high surface area-to-volume ratio makes metal nanoparticles of great interest in different fields; they are used in electronics for applications like flexible displays, conductive inks and printable electronics, in catalytic processes, enabling increased reaction rates and selectivity, but also in energy-related fields and for biomedical applications, in which their properties are exploited for sensitive detection biomarkers and drug delivery[88].

Nanoparticles can be functionalized or modified by attaching specific molecules known as binding ligands onto their surfaces. These ligands play a crucial role in enhancing the stability, dispersibility, and functionality of nanoparticles, opening up a wide range of applications. Here are some key points regarding nanoparticles and binding ligands:

1. Stability and dispersibility: binding ligands as part of the nanoparticle coating help to stabilize nanoparticles by forming a protective layer around them, preventing aggregation or precipitation. This stabilization is especially important in colloidal suspensions or biological environments. Ligands can have hydrophobic or hydrophilic properties, allowing nanoparticles to disperse uniformly in solvents or biological fluids.
2. Surface modification: binding ligands enable the functionalization of nanoparticle surfaces, providing a means to tailor their properties and interactions. By selecting appropriate ligands, nanoparticles can be compatible with specific biological systems, allowing targeted delivery, imaging, or sensing. Ligands can be coupled by specific functionalities at the surface of the nanoparticle and can be antibodies, peptides, or small molecules. Nanoparticles functionalized with binding ligands can exhibit improved stability and biocompatibility in biological systems. Ligands can shield the nanoparticle surface, reducing non-specific interactions with biomolecules and reducing the likelihood of immune responses. This property is critical for applications such as drug delivery, biosensing, and bioimaging.
3. Bioconjugation and targeting: binding ligands can be designed to recognize specific biomarkers, receptors, and therefore specific cells, facilitating targeted delivery in biomedical applications. For instance, ligands can be engineered to bind to cancer cells, enabling the selective delivery of drugs or imaging agents to tumors. This approach enhances therapeutic efficacy while minimizing off-target effects.

4. Multifunctionality and synergistic effects: nanoparticles can be functionalized with multiple types of binding ligands, leading to the creation of multifunctional systems. By combining different ligands, nanoparticles can exhibit synergistic effects, such as enhanced targeting, improved stability, or amplified signal detection, making them highly versatile in various fields.

Nanoparticles and binding ligands have revolutionized several areas of research and technology, including drug delivery, diagnostics, imaging, and nanomedicine. The choice of ligands and their appropriate design is crucial for achieving desired properties, stability, and functionality of the nanoparticles in specific applications.

It is important to note that the design and selection of binding ligands must consider factors such as biocompatibility, toxicity, stability, and the desired interactions with targetted molecules or systems. Comprehensive characterization and optimization are essential to ensure the successful integration of nanoparticles and binding ligands in various applications [89, 90].

Among the different binding ligands, nanobodies are widely used for biomedical purposes. In the next paragraph their characteristics will be analyzed.

2.7.1 Nanobodies

Antibodies are composed of two heavy chains and two light chains. Each heavy chain consists of three constant domains (CH1, CH2, CH3) and a variable domain (VH), each light chain of two domains, the constant one (CL) and the variable one (VL) (Figure 2.16) [91].

In 1989, in animals of the camelid family, antibodies were discovered that lacked the CH1 domain, and consequently only formed from the heavy chain. This kind of antibodies are referred to as heavy-

chain only antibodies (HCAb). Variable antigen-binding (VHH) domains shown by HCAb take the name of nanobodies (Nbs) and over the last 30 years have attracted great interest in various fields of study, including diagnostics and therapeutic applications.

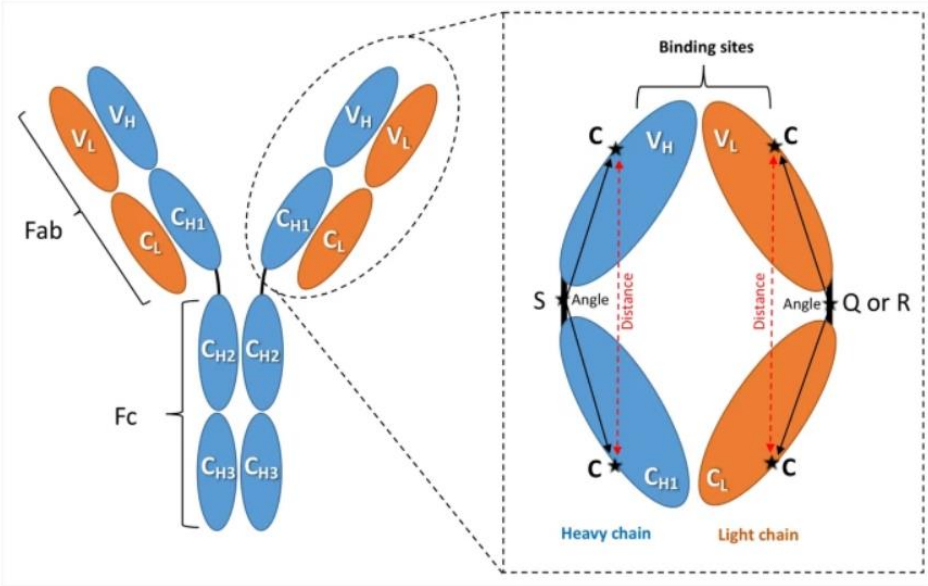

Figure 1 Antibody structure scheme. Image from Al Qaraghuli, M.M., Kubiak-Ossowska, K., Ferro, V.A. et al. Antibody-protein binding and conformational changes: identifying allosteric signalling pathways to engineer a better effector response. Sci Rep 10, 13696 (2020)

Heavy chain only antibodies present a fragment crystallizable (Fc) region directly joined to a fragment antigen-binding (Fab) region consisting of a single VHH domain . The molecular mass of a HCAb is about 90 kDa, compared to the 150 kDa of conventional antibodies, while the VHH fragment of a HCAb has a molecular weight of 15 kDa and can be expressed as a monomeric Nb able to bind a wide antigen repertoire. Nanobodies consist of four conserved framework regions (FR), and three hypervariable complementarity-determining regions (CDR) responsible for determining antigen specificity. These regions fold into two β-sheets with the CDRs located in between them and gathered at the N-terminal of the Nb to form the antigen-binding site, also referred to as the paratope.

Unique features of the nanobodies, such as the size and the convex shape, allow them to bind to antigen sections considered not accessible to conventional antibodies. Size also contributes to easier tissue penetration and blood-brain-barrier crossing, making nanobodies good candidates for drug

delivery, diagnostic and therapeutic applications. In addition to the advantages conferred by the shape, Nbs present particular biochemical characteristics, such as the stability at high temperatures for prolonged periods and the resistance to pH changes. To the described features it is useful to add that the processes of modification, production and purification are easier in Nbs than in conventional Abs.

Despite all the advantages listed so far, the characteristics of the Nbs can lead to unwanted side effects in some situations. First disadvantage is the need to be modified in order to increase their valence and thus their diagnostic and therapeutic capacities.

Additionally, the generation of Nbs requires the use of camelids, and consequently more housing space than the production of mAbs which are commonly generated by immunizing mice. The required use of camelids also presents the drawback of requiring humanization strategies for therapeutic Nbs to minimize the risk of adverse immunogenic side reactions. This, however, comes with the risk of losing their desirable refolding ability advantage or sacrificing antigen binding affinity. Lastly, nanobodies are excellent candidates to recognize concave/hidden epitopes, but can be less proficient at recognizing flat/linear ones, reducing the epitopes range to bind to.

Diagnostic and therapeutic applications of nanobodies

The advent of nanobodies is bringing about a revolution in diagnostics and therapy.

The unique characteristics of nanobodies have made them excellent candidates for various techniques and in different fields.

One of the applications of nanobodies in the diagnostic field is lateral flow immunoassay (LFIA) component. LFIA is a diagnostic test that detects the presence of an antigen of interest within a mixture. In this use the nanobodies replace the conventional antibodies providing high stability and

heat resistance, thereby allowing for longer storage, greater paratope repertoire, allowing for binding to usually inaccessible epitopes as well as preventing competition with host antibodies, and preventing any possible cross-reactions with host antibodies within the sample.

A new application of nanobodies is in the field of biosensor development. A biosensor is composed of a bioreceptor specific to a target antigen; the binding between the receptor and the target antigen generates an electric potential change then converted into a measurable signal. The results provided by these devices are instantaneous, in the scale of seconds. Nanobodies are used as bioreceptors exploiting their ability to withstand high temperatures and pH changes [92].

The fundamental field of application of nanobodies is diagnostic imaging. Techniques such as PET (positron emission tomography), SPECT (single photon emission computed tomography) or infra-red imaging use radioactively- and fluorescently- labeled antibodies to observe and monitor changes in masses or organs in the body. Thanks to their described properties, nanobodies appear as optimal candidates for this aim. Easy tissue penetration and rapid blood clearance are, in fact, important requests in the diagnostic field. When combined with contrast agents, nanobodies can be used for magnetic resonance imaging (MRI) to enhance the contrast of tissue details; when conjugated with high-absorbing nanoparticles, however, Nbs are exploited by computed tomography (CT) for specific molecular imaging. In general, Nbs can be combined with different contrast agents and imaging modalities to obtain multimodal imaging, providing complementary information and diagnostic accuracy.

In therapy, nanobodies have taken hold in the field of oncology, exploiting their targeting specificity capacity and for drug delivery. Different trials are ongoing or approved, such as the ones for breast carcinoma or for multiple myeloma, and the hope is to harness the incredible properties of nanobodies to treat an increasing number of cancers. The therapeutic area where Nbs reached greatest interest is the autoimmune diseases treatment. Studies on different disorders such as multiple sclerosis,

inflammatory bowel disease, rheumatoid arthritis and systemic lupus erythematosus have shown interesting results. Of course the way to obtain an approved drug is long, but the research is promising. An area of application in which there is still little development is the use of nanobodies in the treatment of infectious diseases. It should be underscored, however, how the advent of the COVID-19 pandemic has greatly increased the number of studies and publications featuring Nbs. To complete, the use of nanobodies against toxins and venoms is reported.

Tomography and image processing

Tomography (from the Greek $\tau\acute{o}\mu o\varsigma$, "layer, section", and $\gamma\rho\acute{\alpha}\varphi\omega$, "to write") in general indicates an imaging technique which represents the investigated object in layers or sections through the use of any kind of penetrating wave, as opposed to conventional radiography which has all the thickness of the object projected on the two-dimensional planes. The method is used in a multitude of science areas, like radiology, biology, astrophysics, atmospheric science, geophysics, materials science, conservation science, etc.

3.1 From 2D to 3D

Computed tomography is an investigation method based on the analysis and reconstruction of a multidimensional signal that allows the inspection of an entire three-dimensional object. The image formation process is based on the following procedure: the sample is irradiated by an X-ray beam and the outgoing radiation is measured by a detector. The emitted radiation represents a map of the local X-ray transmission, determined by the absorption coefficients μ of the analyzed object; alternatively, it can be seen as an interference figure from which it is possible to derive the refractive index of the object, as described in the previous chapters. The single image acquired represents a two-dimensional projection (radiograph) of the object and does not allow to obtain information about its three-dimensionality. The principal limitation of 2D radiography is basically the fact that it returns an image that is an overlay of the signal throughout the entire thickness of the sample, not allowing an analysis of the spatial distribution of the features inside the object. To better visualize this concept, let's consider the general case of an X-ray beam irradiating an object composed by different layers of materials with diverse attenuation coefficients μ, as shown in Figure 3.1.

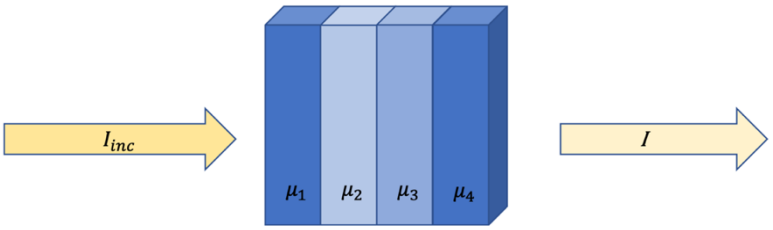

Figure 3.1. An incident X-ray beam irradiates an object composed by different layers of materials with diverse attenuation coefficients μ.

As described by Beer's law, in the case of pure absorption contrast, the intensity of the radiation on the plane just downstream of the object plane is expressed by

$$I(x,y) = I_{in} e^{-\int \mu(x,y,r)dr} \tag{3. 1}$$

where the integral extends over the depth of the sample. The measured attenuation A, also referred to as log-corrected data

$$A = -\ln \frac{I}{I_{in}} = \int \mu(x,y)\, dr \tag{3. 2}$$

is nothing but the *projection* of the function $\mu(x,y)$.

A projection $P_\vartheta(t)$ of a function $f(x,y)$ is defined by the linear integral

$$P_\vartheta(t) = \int f(x,y)\, dr \tag{3. 3}$$

along $S_{\vartheta,t}$, which is the straight line at angle ϑ to the y axis and at distance t to the coordinate origin $(x,y) = (0,0)$ so that

$$S_{\vartheta,t} : (cos\ \vartheta\ , sen\ \vartheta) \cdot (x, y) = t$$

(3. 4)

In general, $f(x, y)$ is a function that describes a slice of the object to study, in the plane parallel to the direction of probing rays. Then, in our case

$$f(x, y) = \mu(x, y).$$

Returning to the specific case schematized in Figure 3.1, the intensity equation (3.1) becomes

$$I = I_{in} e^{-[(\mu_1+\mu_2+\mu_3+\mu_4)l]}$$

(3. 5)

where I_{in} is the intensity of the incident beam and l is the length traveled by the beam. Therefore, the projection function is

$$P_{\vartheta}(x) = \sum_{i=1}^{4} \mu_i$$

(3. 6)

i.e the projection function corresponds to the summation of the attenuation coefficients along the direction of beam propagation. In light of this discussion, it is clear that from a single 2D image (or projection) overlapping structures cannot be discerned.

Tomography has made it possible to exceed this limitation: radiographs acquired at different angles of beam incidence are processed by an algorithm which allows to reconstruct the image, i.e. the spatial distribution of attenuation coefficients. This imaging method allows obtaining three-dimensional images of the object which can be visualized, through a virtual "cutting", as cross-sections, commonly called “slices”, whose gray-scale distribution is proportional to the

attenuation properties of the sample ["Fundamentals of Medical Imaging Second Edition"]. The sample is divided into units of volume (voxels) and the variation suffered by the beam is calculated for every voxel.

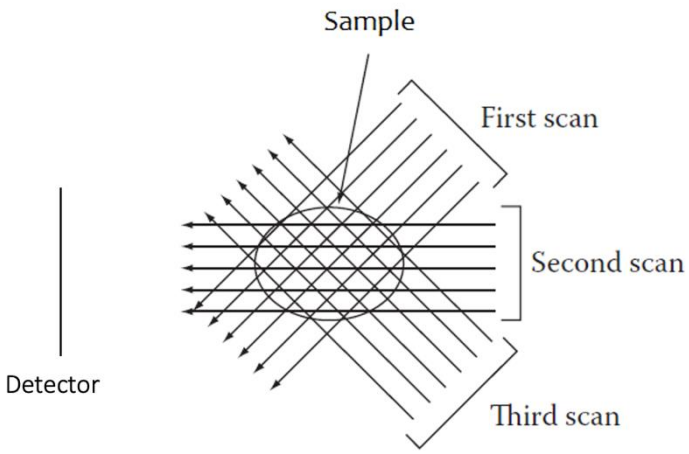

Figure 3.2 . Schematic representation of tomographic procedure of acquisition for a parallel beam. Image adapted from «Webb's Physics of Medical Imaging» 2nd Edition [93].

By recording on the detector, the intensity for different angular positions of the sample with respect to the direction of probing beam, we obtain the line integral of $\mu(x, y)$ - or, in other words, the projection - along the beam direction for each acquisition angle. Now, what we have to do, is to solve an inverse problem: starting from the projections, reconstructing the spatial distribution of $\mu(x, y)$. That is the meaning of tomography by mathematical definition: tomography is just the reconstruction of a function $f(x, y)$ from its line integral. For this purpose, we use *Radon transform* – which associates to each point in the Cartesian plane ((x, y) the set of its line integrals in the so-called Radon's plane - or more properly its inversion.

It is important to note that in the parallel beam geometry, such as that provided by synchrotron light sources, the slices of the sample corresponding to different heights in the sample can be treated independently. Then, in the following description we assume it to work with parallel beam geometry.

3.1.1 Radon Transform

The Radon transform [94] of a two-dimensional and continuous function $f(x,y)$ corresponds to the value of the integral of $f(x,y)$ along the line $y = px + \tau$ where p is the slope and τ is the value of the intersection with the y-axis

$$Rf = \check{f}(p,\tau) = \int_{-\infty}^{\infty} f(x, px+\tau)\, dx \tag{3. 7}$$

The Radon transform is function of the parametrization of the line in the plane (x,y).

Considering the Dirac delta function, the equation can be rewritten as

$$\check{f}(p,\tau) = \int_{-\infty}^{\infty}\int_{-\infty}^{\infty} f(x,y)\delta(y-px-\tau)\, dxdy \tag{3. 8}$$

where the link between the transformation and the line in the plane (x,y) is evident.

Since in computed tomography the sample is irradiated at different angular positions and the signal is collected for all these directions, it is useful to introduce polar coordinates, with reference to the origin of the Cartesian plane; each line is associated with the angle ϑ and the modulus t of the normal vector to the line itself.

The relation between the pairs of coordinates will be given by

$$|t\ s\ | = |cos\vartheta\ sin\vartheta\ \ - sin\vartheta\ cos\vartheta\ ||x\ y\ |$$

(3. 9)

Using the parametrization in polar coordinates, the transform is referred to as *normal Radon transform* and assumes the expression

$$f(\vartheta, t) = \int_{-\infty}^{\infty}\int_{-\infty}^{\infty} f(x,y)\delta(t - x\ cos\vartheta - y\ sin\vartheta)\ dxdy$$

(3. 10)

or, considering s as the linear variable along the line

$$f(\vartheta, t) = \int_{-\infty}^{\infty} f(t\ cos\vartheta - s\ sin\vartheta, t\ sin\vartheta + s\ cos\vartheta)\ ds$$

(3. 11)

An important property of the normal Radon transform is that it allows to represent in the Radon plane (ϑ, t) each line of the plane (x, y) without limiting the variability range of ϑ and t, which belong to the intervals $0 \leq \vartheta \leq \pi$ and $-t_{max} \leq t \leq t_{max}$.

In the context of medical imaging, f represents the spatial distribution of the attenuation coefficients $\mu(x, y)$ and therefore its Radon transform corresponds to the projection function $P_{\vartheta}(t)$.

$$P(\vartheta, t) = \int_{-\infty}^{\infty} \mu(t\ cos\vartheta - t\ sin\vartheta, t\ sin\vartheta + t\ cos\vartheta)\ ds$$

(3. 12)

$P(\vartheta, t)$ can be measured for all ϑ from 0 to 2π, but projections collected from opposite angles lead to the formation of identical images: it is therefore sufficient to measure $P(\vartheta, t)$ in a range from 0 to π.

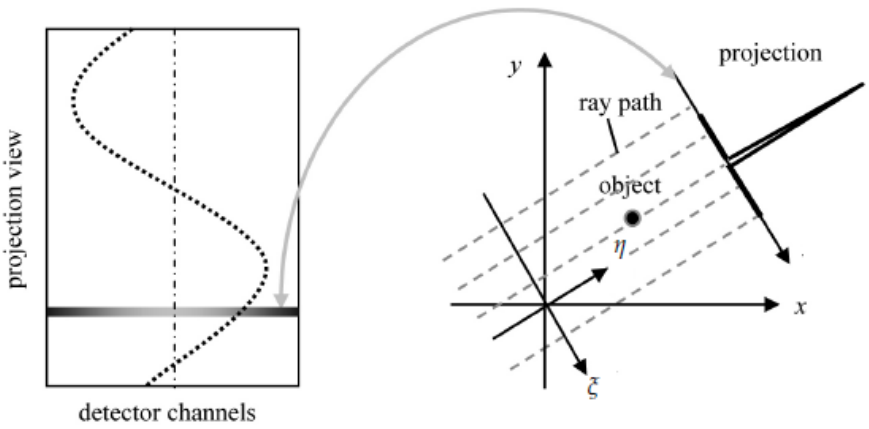

Figure 3.3. Illustration of mapping between the object space and the sinogram space (left). A sinogram is formed by stacking all of the projections of different views, so that a single projection is represented by a horizontal line in the sinogram. The projection of a single point forms a sinusoidal curve in the sinogram space. Image from «Computed tomography : principles, design, artifacts, and recent advances», 2nd Edition. [50].

An experimental sample of $P(\vartheta, t)$ over the ϑ range from 0 to π is called *sinogram*. This name reflects the fact that a point in the xy plane is mapped onto a sinusoidal trajectory in the transformed plane.

The reconstruction of $\mu(x, y)$ from a sinogram $P(\vartheta, t)$, as said above, is an inverse problem and requires finding a mathematical expression for Radon's inverse transformation

$$\mu(x, y) = R^{-1}[P(\vartheta, t)] \tag{3. 13}$$

The most common method of inversion is the *Filtered Back-Projection* (FBP) which provides a good compromise between image quality and calculation time. The FBP is a combination of

filtering and integration and it will be derived in the following. It is based on the Fourier Slice theorem that will be discussed in the following section.

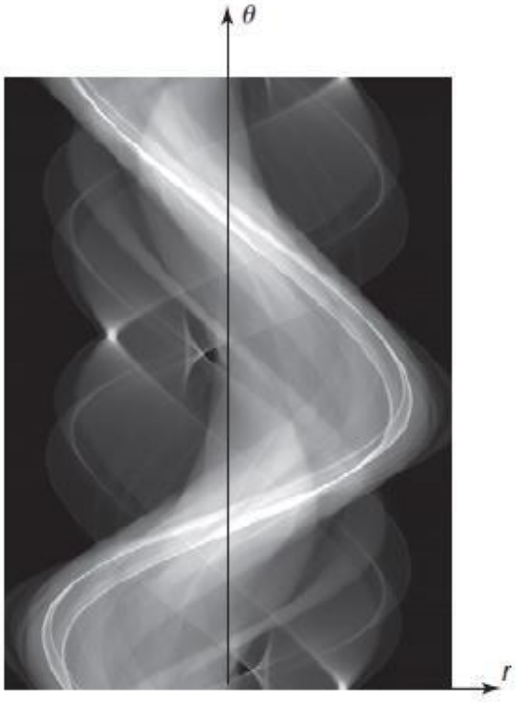

Figure 3.4. A sinogram is a representation of an experimental sample of the projection function $P(\vartheta, t)$ over the ϑ range from 0 to π. Image adapted from «Webb's Physics of Medical Imaging» 2nd Edition [93].

3.1.2 Fourier Slice Theorem

The Fourier slice theorem states that the one-dimensional Fourier transform (FT) of the Radon transformation of a generic two-dimensional $f(x,y)$ function corresponds to a slice - through the origin, parallel to the projection line - of the two-dimensional FT of the same $f(x,y)$ function.

$$F_{2D}f(\omega\, cos\vartheta, \omega\, sin\vartheta) = F(Rf)(\omega,\vartheta) \tag{3. 14}$$

The validity of the Fourier slice theorem can be easily verified.

The 2D Fourier transform of $f(x,y)$ is given by:

$$F_{2D}f(x,y) = \tilde{f}(k_x,k_y) = \iint f(x,y)e^{-2i\pi\,(k_x x + k_y y)}dxdy \tag{3. 15}$$

and for completeness' sake, the inverse FT is

$$f(x,y) = \iint \tilde{f}(k_x,k_y)e^{2i\pi\,(k_x x + k_y y)}dk_x dk_y \tag{3. 16}$$

If we take the slice $s(k_x) = \tilde{f}(k_x,0)$, we obtain

$$s(k_x) = \iint f(x,y)e^{-2i\pi\,(k_x x)}dxdy = \int_{-\infty}^{\infty}[\int_{-\infty}^{\infty} f(x,y)dy]e^{-2i\pi\,(k_x x)}\,dx$$

$$= \int_{-\infty}^{\infty}[Rf(x,y)]\,e^{-2i\pi\,(k_x x)}\,dx \tag{3. 17}$$

where the last term is just the Fourier transform of the Radon transform of $f(x,y)$.

It has been obtained that to make explicit the function $f(x,y)$, which corresponds to the inverse Radon transform, it is necessary to calculate the two-dimensional inverse Fourier transform of the spectrum of the Radon transformation. In two steps:

- FT of the Radon transform of $f(x, y)$

$$\tilde{f}(k_x, k_y) = \tilde{f}(\omega\, cos\vartheta, \omega\, sin\vartheta) = \int_{-\infty}^{\infty} f(\vartheta, t) e^{-2i\pi\, \omega t} dt = \tilde{P}_{\vartheta}(\omega)$$

(3. 18)

here expressed by using polar parametrization described as follows

$$\left| k_x\, k_y \right| = \omega |cos\vartheta\, sin\vartheta\,|$$

(3. 19)

- Inverse FT of $\tilde{f}(\omega\, cos\vartheta, \omega\, sin\vartheta) = \tilde{f}(k_x, k_y)$

$$f(x, y) = \iint \tilde{f}(k_x, k_y) e^{2i\pi\, (k_x x + k_y y)} dk_x dk_y$$

(3. 20)

In the context of medical imaging, it should then be possible to reconstruct the object function $\mu(x, y)$ for each point (x, y) by collecting the projections $P_{\vartheta}(t)$ over an angular range $\theta \in [0, \pi)$ and firstly calculating a 1D FT on each projection, and then using a 2D inverse FT.

There are two problems with this approach. The first problem depends on the fact that the amount of measurements, in practice, is finite. Under ideal conditions, assuming an infinite number of projections in the range $(0, \pi)$, the value of the function $P_{\vartheta}(t)$ would then be known in all points and $\mu(x, y)$ could be perfectly calculated. In real conditions, the number of projections is, however, finished, which leads to a Fourier domain that is sampled in a difficult way to work with; the data $\tilde{f}(k_x, k_y)$ - collected on the detector - lie on a radial grid, while the practical algorithms which perform the inverse transformation, such as the Fast Fourier transform, require them on a Cartesian grid. This means that we'll have to apply interpolation in the Fourier domain which causes strong reconstruction artifacts.

The second problem is due to the fact that the sampling distribution of the Fourier domain is much denser near the origin than it is for the outer regions. Therefore, for the lowest frequencies - which lie close to the origin - there is a big amount of data available, meaning that these low frequencies will be reconstructed fairly accurately. On the other hand, the high frequencies – which is where most of the finer details of the object are located – are under-sampled and will not be accurately reconstructed after the inverse Fourier transform: this will lead to very blurry images.

The reconstruction method called *filtered backprojection* (FBP), based on the Fourier slice theorem, overcomes these drawbacks: it avoids the artifacts by interpolating the data in real space and introduces an additional filtering step. In the following, this practical approach, yet related, will be described.

3.1.3 Filtered Backprojection

We are now finally ready to make an attempt at recovering the object function by means of filtered backprojection, which involves two steps: a filtering and a backprojection step.

Let us define the backprojection of a function $h(t,\vartheta)$ at a point (x,y) as

$$Bh(x,y) = \int_0^{\pi} h(t,\vartheta)\, d\vartheta \tag{3. 21}$$

Applying this backprojection formula to the Radon transform, we obtain the following

$$B(Rf(x,y)) = \int_0^{\pi} Rf(t,\vartheta)\, d\vartheta \tag{3. 22}$$

where, as usual, in the context of medical imaging, f represents the attenuation coefficient function. During backprojection one attributes the value of the projection $P_\vartheta(t) = Rf(t,\vartheta)$ to every point (x,y) which is projected onto point x of the detector. This is repeated for each

projection. However, the result of a simple backprojection is a blurred version of the spatial distribution of the object distribution. To correct for this, filtering steps have been introduced.

Let us rewrite the object function $f(x,y)$ via the inverse FT

$$f(x,y) = \int_{-\infty}^{\infty} dk_x \int_{-\infty}^{\infty} dk_y \, \tilde{f}(k_x,k_y) e^{2i\pi\,(k_x x + k_y y)} \tag{3. 23}$$

In polar coordinate system, by substitutions

$$\{k_x = \omega\, cos\vartheta \; k_y = \omega\, sin\vartheta$$

which tells us that $dk_x\, dk_y = \omega\, d\omega\, d\vartheta$, equation 3.23 becomes

$$f(x,y) = \int_0^{2\pi} d\vartheta \int_0^{\infty} \tilde{f}(\omega\, cos\vartheta, \omega\, sin\vartheta)\, e^{2i\pi\,\omega\,(x\, cos\vartheta + y\, sin\vartheta)} \omega d\omega \tag{3. 24}$$

Now we exploit the Fourier Slice Theorem which allows to replace $\tilde{f}(\omega\, cos\vartheta, \omega\, sin\vartheta)$ with $\widetilde{P}_\vartheta(\omega)$, where $\widetilde{P}_\vartheta(\omega)$ is the Fourier transform of the projection $P_\vartheta(t)$ with respect to t. The equation 3.24 becomes

$$\begin{aligned} f(x,y) &= \int_0^{2\pi} d\vartheta \int_0^{\infty} \tilde{P}_\vartheta(\omega)\, e^{2i\pi\,\omega\,(x\, cos\vartheta + y\, sin\vartheta)} \omega d\omega = \\ &= \int_0^{\pi} d\vartheta \int_0^{\infty} \tilde{P}_\vartheta(\omega)\, e^{2i\pi\,\omega\,(x\, cos\vartheta + y\, sin\vartheta)} \omega d\omega \\ &\quad + \int_0^{\pi} d\vartheta \int_0^{\infty} \tilde{P}_\vartheta(\omega)\, e^{-2i\pi\,\omega\,(x\, cos\vartheta + y\, sin\vartheta)} \omega d\omega \end{aligned} \tag{3. 25}$$

Observing that $\tilde{P}_{\vartheta+\pi}(\omega) = \tilde{P}_\vartheta(-\omega)$, the equation (3.25) assumes the form

$$f(x,y) = \int_0^{\pi} d\vartheta \int_{-\infty}^{\infty} \tilde{P}_{\vartheta}(\omega)\, e^{2i\pi\,\omega t} |\omega| d\omega$$

(3. 26)

where we have simplified the expression by setting $t = (x\,cos\vartheta + y\,sin\vartheta)$. We have obtained a relation between the projections and the image to be reconstructed. To spot from this equation is that the projections are multiplied by $|\omega|$ in the Fourier domain. In other words, the projections are filtered by the $|\omega|$ function before moving back into the time domain; through the filtering step low frequencies are suppressed in favor of high frequencies.

Defining filtered projection in the direct domain as

$$P'_{\vartheta}(t) = \int_{-\infty}^{\infty} \tilde{P}_{\vartheta}(\omega)\, e^{2i\pi\,\omega t} |\omega| d\omega$$

(3. 27)

the object function can be written as

$$f(x,y) = \int_0^{\pi} d\vartheta\, P'_{\vartheta}(t)$$

(3. 28)

which is referred to as backprojection of the function $P'_{\vartheta}(t)$. It shows that the reconstructed image $f(x,y)$ is the sum of all the filtered projections passing for (x,y).

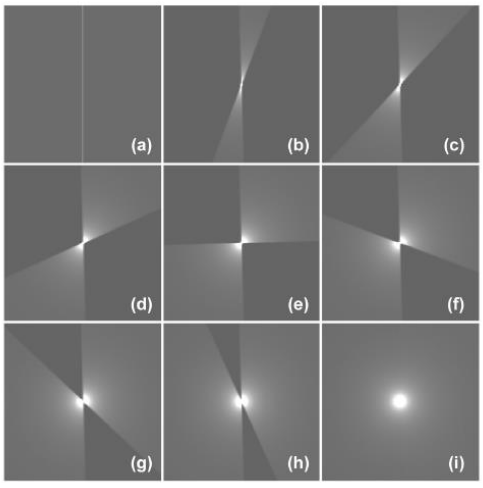

Figure 3.5. Backprojection process of a single point. (a) Backprojected image of a single projection. (b)–(i) Backprojection of views covering: (b) 0 to 22.5 deg; (c) 0 to 45 deg; (d) 0 to 67.5 deg; (e) 0 to 90 deg; (f) 0 to 112.5 deg; (g) 0 to 135 deg; (h) 0 to 157.5 deg; and (i) 0 to 180 deg. Image from «Computed tomography : principles, design, artifacts, and recent advances», 2nd ed.[50].

The filter $|\omega|$ amplifies the high frequencies and consequently the high frequency noise. The parameter ω has the dimensions of a frequency; therefore, theoretically, the integral (4.29) should be calculated for every possible frequency. In practice, however, the energy contained in the components of the Fourier transform beyond a certain frequency is negligible, so it is possible to integrate (4.29) within a limited range of frequencies $(-W, W)$

$$P'_{\vartheta}(t) = \int_{-W}^{W} \tilde{P}_{\vartheta}(\omega)\, e^{2i\pi\,\omega t} |\omega| d\omega \qquad (3.\ 29)$$

Suppose that the projection data is sampled with a sampling rate $\frac{1}{s_p}$, where s_p is the pixel size of the detector. If there is no aliasing, it implies that the spectrum of the projections and the reconstruction may be limited to a maximum frequency

$$W = \frac{1}{2s_p}$$

known from the Nyquist frequency, which describes the sufficient condition for a perfect reconstruction. It follows that the original function |ω| can be replaced by the function

$$H(\omega) = |\omega| g(\omega)$$

where

$$g(\omega) = \{1\ for\ |\omega| < W \quad 0\ otherwise$$

The function is shown in Figure

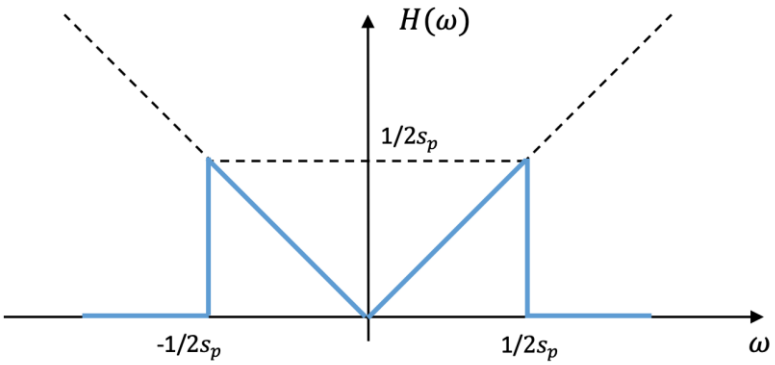

Figure 3.6. Function $H(\omega)$, used to filter the frequencies in the backprojection algorithm, is a band-limited ramp filter, highlighted in blue.

The introduction of a filter is essential because of the tomographic setup of projection acquisition; as said before, the Fourier domain of the object is sampled in such a way that low frequencies are sampled much more densely than the high frequencies. The result is a reconstructed image which appears to be extremely blurred because in image processing the low frequencies take care of the smooth surfaces and the high frequencies take care of the details and the sharp edges. Since the high frequencies are underrepresented the resulting back projection is indeed severely unsharp.
By multiplying the projections functions by $|\omega|$, we apply a high-pass filter on the detector function: low frequencies will be suppressed such that they will not result in an overly blurred back-projected image and high frequencies will gain relative importance.

The complete filtered back projection algorithm can be summed by the following steps:

- FT of projection $P_\vartheta(t)$:

$$FP_\vartheta(t) = \tilde{P}_\vartheta(\omega) \tag{3. 30}$$

- Multiplication by frequency filter $|\omega|$

$$\tilde{P}_\vartheta(\omega)|\omega| = \widetilde{P'}_\vartheta(\omega) \tag{3. 31}$$

- Inverse Fourier transformation

$$\int_{-\infty}^{\infty} \tilde{P}_\vartheta(\omega)\, e^{2i\pi\,\omega t}|\omega| d\omega = P'_\vartheta(t) \tag{3. 32}$$

- Backprojection

$$f(x,y) = \int_0^\pi d\vartheta\, P'_\vartheta(t) \tag{3. 33}$$

Backprojecting in only a few directions ϑ is an incredibly inaccurate way of recreating even a simple object, so it is necessary to significantly increase the number of projections used to reconstruct the object function (1000 directions and more). If the sampling rates in the x and ω directions are sufficient, analytical methods such as backprojecting are superior with respect to the speed and the quality of the reconstruction than the iterative methods, which are slower and can diverge in presence of noise.

3.1.4 Holotomography

Holotomography is a technique which combines in-line holography and tomography [95]. A holographic reconstruction procedure combines a set of Fresnel diffraction patterns taken at different distances from the sample. Varying the distance is important to avoid indeterminacy in the phase retrieval problem (discussed in previous chapter with the name of multiple-distance phase retrieval), because at given distances the image is blind for some frequency components of the object. Zabler et al. [54] calculated the phase from combinations with different numbers of Fresnel diffracted images; in particular they compared the phase retrieval obtained from $N = 1,2,4,8$ propagation distances. They observed that the quality of the retrieved phase increases a lot from 1 to 2 and from 2 to 4 distances, while there is not a significant improvement from 4 to 8 distances. In the light of this, they concluded that the optimal compromise between quality and experiment duration is obtained by using four propagation distances.

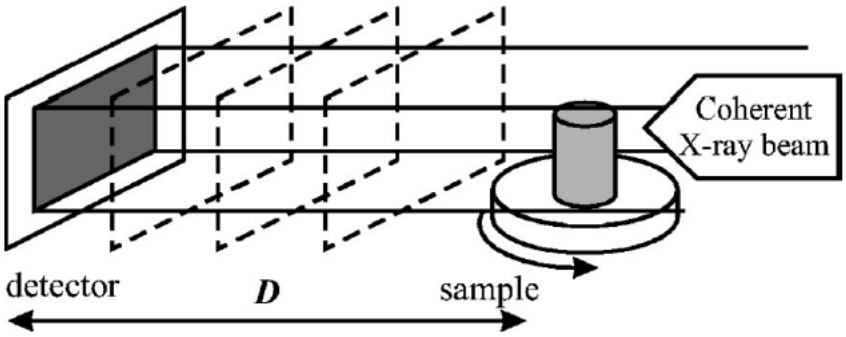

Figure 3.7. Setup scheme of holotomography. For each angle of acquisition, images are recorded at different distances (three, in the case of the drawing) and combined to retrieve the phase of the beam after the interaction with the sample. Figure from Cloetens, et al. 1999[95].

Holotomography results in quantitative phase mapping and, through association with three-dimensional reconstruction, the complete three-dimensional mapping of the density in a sample. The complete reconstruction requires two steps. In the first, the phase modulation is recovered for every projection from a set of in-line acquisitions, according to the procedure of multiple-distance phase retrieval. In the second step the set of retrieved projections is processed by means of a filtered backprojection algorithm.

3.2 Image processing

X-ray phase contrast tomography, as well as computed tomography, requires a significant amount of computational work [96]. All the acquired tomographic projections need to be digitally processed to obtain the images that make up the 3D virtual volume. This process, defined as tomographic reconstruction, generally includes calculation steps added before or after the execution of the actual reconstruction algorithm. Most of these steps aim at improving image quality, especially in terms of artifact removal and noise reduction. To prevent misinterpretation of images, it is important to recognize the artifacts, usually due to experimental conditions or computational reconstruction. A deep understanding of these elements is essential to optimize the entire workflow that starts from sample preparation and leads to the results extrapolated from the quantitative and qualitative image investigation. I will present an overview of the most frequent artifacts I have dealt with and the strategies I have employed to remove or attenuate them.

To extract qualitative and quantitative information, other operations of image post-processing are required.

3.2.1 Tools

For computational image processing I used several software, of which the main ones will be described below. *SYRMEP Tomo Project* is a software developed for tomographic reconstruction which allows the user to customize the reconstruction process and to obtain a more refined processing by eliminating artifacts and improving image quality.

ImageJ is a digital image processing software, used to improve the image quality and to perform quantitative analyses.

VGStudio Max is a platform for visualizing, manipulating, segmenting and analyzing CT-data.

SYRMEP Tomo Project (STP)

Usually a preliminary reconstruction and visualization of the data is performed during the beamtime, to allow a rapid feedback on data quality and experimental conditions as well as sample preparation and positioning onto the rotating stage. For this purpose, the beamline provides software to apply a standard reconstruction algorithm composed by flat-field correction, Paganin's phase retrieval and FBP. The provided software is designed to meet the characteristic of the beam and the set-up of the beamline for which it has been developed. For this reason, it can include particular procedures or filters to correct artefacts and distortions introduced by the actual beamline set-up, e.g. by the optic elements. So, if on the one hand the software is optimized for the beamline, on the other hand the user usually cannot adapt it according to his needs, and his personal contribution reduces to determine the proper center of rotation [97] and tune the parameter δ/β of the phase retrieval step, that are procedures requiring some trials with visual supervision.

A further limitation in using the beamline software is represented by the fact that post-beamtime refinements and optimizations on the reconstruction can be performed only if the facility offers access to a remote computing infrastructure.

When necessary, we use SYRMEP Tomo Project (STP), an open-source software with a graphical user interface (GUI) designed to allow customized tomographic reconstruction process[98]. The software has been developed in collaboration with the University of Trieste (http://www.units.it) and CNR Nanotec. First of all, STP allows the tomographic reconstruction of the acquired data at a later stage at user's home institution. This possibility enables the users to focus their attention and efforts during the beamtime in the optimization of the acquisition parameters (e.g., beam energy, sample-to-detector distance, number of acquired projections, exposure time) and in the

maximization of the number of scanned samples. Secondly, though STP it is possible to explore different strategies of reconstruction, e.g. testing different algorithms of phase retrieval, ring-artifact compensation or reconstruction approaches, in order to obtain the best image quality achievable. For example, without being bound to a standard reconstruction pipeline, we can decide to proceed with de-ringing through pre-processing procedures provided by STP and working on sinograms or mitigate the artifacts during the post-processing with other algorithms working on reconstructed images.

ImageJ

ImageJ is a digital image processing software, developed by National Institutes of Health of the United States of America[99]. The software is based on an open-source structure, with a Java compiler and a plug-in editor.

There are "ad hoc" plugins available for the acquisition, analysis and processing of images, which can be visualized as "stacks", i.e. stacked slices of a cubic section. The data can have 8, 16 or 32 bits per pixel. The data are stored as a single file, which can then be highlighted, transformed, turned or deformed according to different criteria.

ImageJ can measure distances, areas and angles; it can calculate statistics of pixel values in user-defined selections and objects segmented according to intensity thresholds. It can create density histograms and draw contour lines (between defined points). It supports standard image processing functions such as logical and arithmetic operations between images, brightness and contrast adjustment, convolution, Fourier analysis, sharpening, smoothing, contour recognition and median filtering, mathematical morphology. It also performs geometric transformations such as scaling, rotation and reflection. The software supports the most common image formats and can open any number of images simultaneously, limited only by the available RAM of the machine.

VG Studio Max

VG studio Max is a software for three-dimensional rendering of CT-data with applications in different industrial and scientific fields, such as biology, bio-medical research, geology or archeology. It is a platform for visualizing, manipulating, segmenting and analyzing volume data. The software is an excellent tool for 3d visualization of the data and for reporting and presentation functions but offers limited options for quantitative analysis, although it provides additional packages with functions dedicated to particular applications.

3.2.2 Image processing

Flat field correction

When we deal with real sources and real detector, fluctuations and non-ideal functioning must be considered. The complex system of image acquisition is composed by detector, scintillator screen and readout system. Each of these components may suffer of non-ideal functioning, resulting in gain variations of the detector response due to inhomogeneities in the photon conversion yield, losses in charge transport, charge trapping, or variations in the performance of the readout. Also, the scintillator screen may accumulate dust and/or scratches on its surface and in the bulk.

Consequently, acquired projections generally undergo a fixed-pattern noise, which is one of the limiting factors of image quality such as spatial resolution. The conventional method that can compensate this effect is called flat field correction (FFC). A certain number of "flat" images are acquired during the experiment and used as a reference. Flat images are images collected with the sample outside of the field of view, with and without the X-ray beam turned on, which are referred to as flat fields I_{flat} and dark fields I_{dark}. I_{dark} include the nonuniform sensitivity of the charge-coupled device (CCD) pixels, the non-uniform response of the scintillator screen. I_{flat} mainly

corrects the inhomogeneities of the incident X-ray beam and the detector response. Based on the acquired flat and dark fields, the measured projection images $I_{acquired}$ with sample are then normalized according to:

$$I_{corr} = \frac{I_{acquired} - I_{dark}}{I_{flat} - I_{dark}}$$

Flat fields are often far from stationary, resulting in significant systematic errors in intensity normalization. The simplest method is to calculate the average of I_{dark} and I_{flat} and substituting them in expression of I_{corr}. An alternative approach was proposed by Vincent Van Nieuwenhove in 2015 [100] using eigen flat fields. This procedure named Dynamic Flat Field Correction (DFFC) has been transposed in a MATLAB code and has been applied to images acquired at SLS during this project.

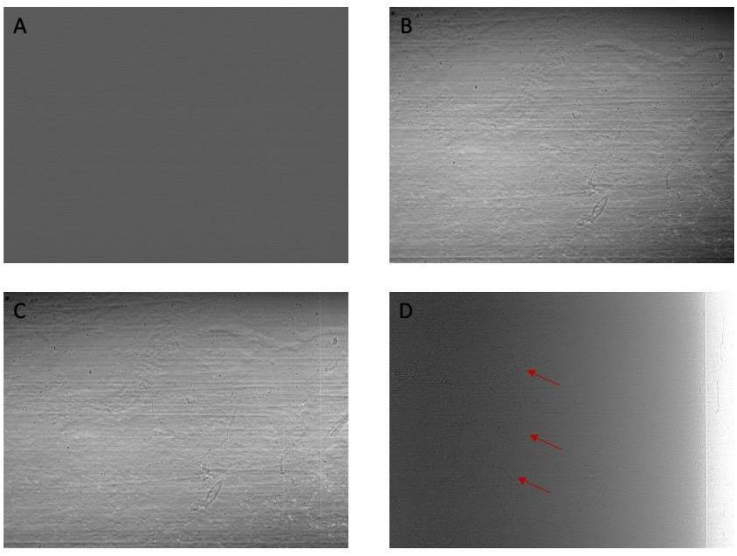

Figure 3.8 Dark field (A), Flat field (B), Projection (C) and corrected image with FFC (D). Details of sample are barely visible (red arrows) since phase information are not yet retrieved.

Volume Reconstruction and Phase Retrieval

CT reconstruction is the process that allows to transform a collection of 2D projections into a tomographic 3D volume. It can be performed through several methods such as iterative method or Filtered Back Projection, as pointed out above.

Paganin algorithm was applied as well to extract phase information from acquired radiographies.

Both stages were performed with STP software described in previous section.

Image Post Processing Pipeline

There are, however, inhomogeneities in the experimental apparatus that are not constant in time and that cannot be corrected by FFC. In fact, anomalies in the response of the single detector pixel and temporal variations in the intensity of the beam may generate concentric rings around the center of rotation of the sample.

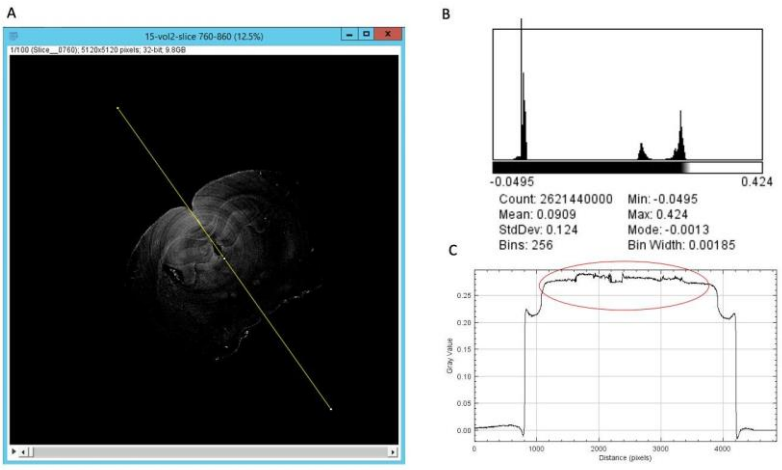

Figure 3.9 A slice from a tomographic volume of mouse brain. Plots on the right show the pixel intensity distribution for the entire slice, on the top, and intensity distribution of the pixel from the slice along the corresponding yellow line.

The so-called rings artifacts originate from the rear projection of line-shaped artifacts present in the sinogram. Artefacts suppression can be addressed with pre-processing algorithms, applied before the actual tomographic reconstruction process.

However, pre-processing artefacts removal may not always be effective even introducing new artifacts and distortions. Moreover, oscillations in the beam intensity may cause variation in slice contrast resulting in a mean value fluctuation of pixel intensity.

Images post reconstruction process suffer from problems originated by the dynamic range of the detector. In fact, abrupt variations in the refractive index inside the FOV saturates grey-scale values available for detected objects. As shown in Fig.3.9 the interfaces between air-sample and samples air produces the first and the last of the three visible peaks on the image histogram. If the grey value is plotted as a function of the distance calculated along the yellow line, it can be observed that the signal from the sample comes from the region inside the red circle. In the light of the above, contrast from detail of interest in images is reduced.

The amount of data collected for each acquisition push me to develop a pipeline for automatic image post-processing through ImageJ macro. This pipeline is aimed to enhance the contrast of details of interest while removing ring artefacts starting from the reconstructed tomographic slices.

The macro consists in several steps, illustrated below:

1. Maximum and minimum. They are settled to an established value. This step is fundamental to set the extremes for image normalization.
2. Cartesian-to-polar conversion. In polar coordinates, ring artefacts appear as stripes parallel, and it is easier to separate their contribution from the image.

3. Filtering. The macro includes a filter with data-depending size *N* to be applied on the columns to attenuate the stripes. After testing, we assessed that the best choice for our images is given by median filter, set to replace each pixel of the column with the median of the pixels within a certain distance.
4. Polar-to-Cartesian conversion. Coordinate transformation is performed to conclude the de-ringing process. The evaluation of the efficacy of a filter was done, as usually, through visual inspection of the output image.

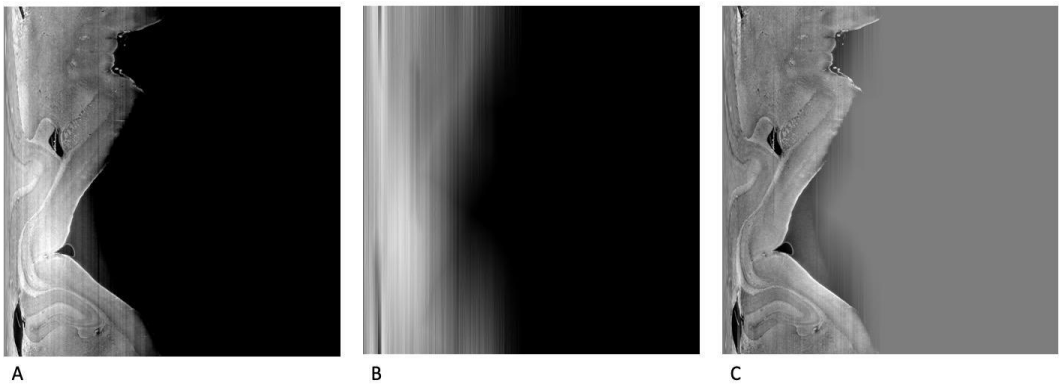

Figure 3.10 Ring artefacts removal in polar coordinate space. (A) the original slice in polar coordinates, (B) fast filtered subtracted image which highlight rings in the new space, (C) image resulting from correction A-B.

5. Normalization to the background. The normalization to the background is a step that we cannot prescind from because it allows us to make histograms of images acquired in different stack comparable for the further analyses.

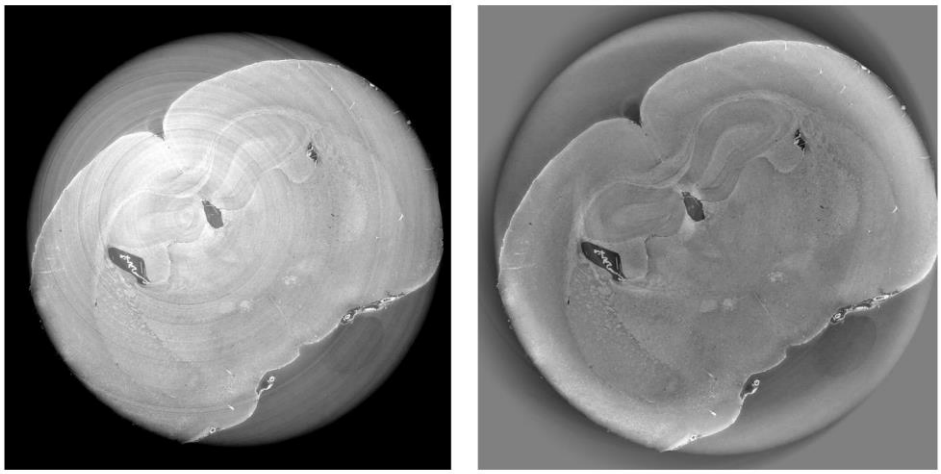

Figure 3.11. Tomographic slice before and after ring removal

All the images have been treated with my customized de-ringing macro, adjusting parameters as needed.

Movement Artefacts

Unfortunately, is not possible to adjust artefacts which are due to unwanted experimental defections as in the case of movement artefacts. Even though the sample is stuck during the measurements by an embedding medium or glue, samples or parts of samples may move during measurements. If not well fixed, the rotation itself, which is necessary for tomographic measurement, may cause an unintended displacement of the sample. Moreover, the exposure to X-ray beam and air during the measurement may cause changes in the sample shape during acquisition due to dehydration of the sample or heating or shrinkage of the medium containing the object.

Dealing with very high spatial resolution, even a very small displacement affects the success of the measurement. The displacement in the order of the pixel size produces artifacts shown in Fig. 3.12.

If a detail inside the sample moves during tomography, it no longer draws a complete sinogram, but the corresponding pixel has more than one fragmented sinogram. This displacement varies smoothly with angular position, causing point-like features appear as banana-shaped artefacts that cannot be removed.

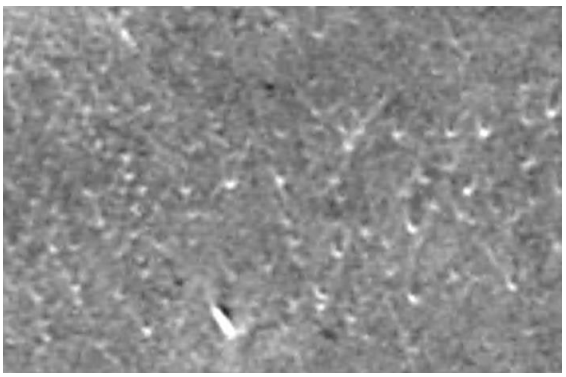

Figure 3.12 Movement artifacts resulting in crescent shaped details.

Experimental results and data analysis

The study of neurodegenerative diseases requires the following of cells of interest, biomarkers and features within the brain, the nervous system and the entire organism. This kind of detail is crucial to understand the mechanisms of the disease, the efficacy of a drug and to intervene at the very early stage of the disorder. Identifying a disease in a pre-symptomatic stage could mean dramatically changing the life of the patient and reducing therapies and costs in the future.

Despite the efforts and the improvements in this field, a single technique able to visualize details of interest together with the organism as a whole is not available. X-ray phase contrast tomography is a novel imaging technique able to provide 3D images of objects at high spatial resolution, allowing the visualization of cells in the physiological or pathological environment, together with the vascular and the neuronal systems. However, the identification of the cells is limited to a morphological speculation and this drawback leads to the need of complementary techniques that validate the XPCT results.

This thesis project stems from the idea of implementing XPCT to obtain a specific technique applicable to *ex-vivo* and *in-vivo* organs and animals without using complementary techniques.

With this aim we introduce a complex we called Nano2 composed by metal nanoparticles and nanobodies; after the administration to mice, Nano2 should spread within the organ, target the selected cells population and be detected trough XPCT thanks to physical properties of the metal nanoparticles. This study requires several validation steps:

- The choice of the metal for the nanoparticles
- The choice of the cell population
- The choice of the nanobody
- The functionalization of the nanoparticles
- The conjugation between the nanoparticles and the nanobody

- The validation of the targeting
- The distribution of the complex in the animal
- Imaging experiments

Of course, each step involves sample preparation tests and feasibility studies.

The first metal we used is gold and we conjugated the nanoparticles with GFAP nanobody able to mark astrocytes, cell population highly activated in neurodegenerative diseases.

In this chapter, I will present and discuss results from the following experiments tests:

- Functionalization of the nanoparticles and preparation of the conjugates
- Nano2 – GFAP binding
- Method of administration of Nano2
- Validation of the targeting
- L-Edge subtraction imaging
- K-Edge subtraction imaging
- XPCT imaging
- Holo-nano- tomography imaging.

4.1 Experiments

First experiments were performed in the EAE (experimental autoimmune encephalomyelitis) mice model of multiple sclerosis human disease. In this mice model there is an altered blood-brain barrier which we exploited to assure that the NPs cross the barrier and spread through the brain.

In Figure 4.1, a 3D-rendering of 3D XPCT image of mice spinal cord, acquired post-mortem, is shown. We can identify localized extravasated material (bright gray) in panel A; in panel B, the 3D-rendering of the lesion shows the difference between the small cells (white) surrounding the vessel (red) and the morphologically neuron-like cells (purple). “Clouds” of extravasated

material reflecting BBB dysfunction together with accumulation of cells are also observed in the volume from the cervical region of the spinal cord up to the brain stem, and cerebellum of the same EAE-affected mouse.

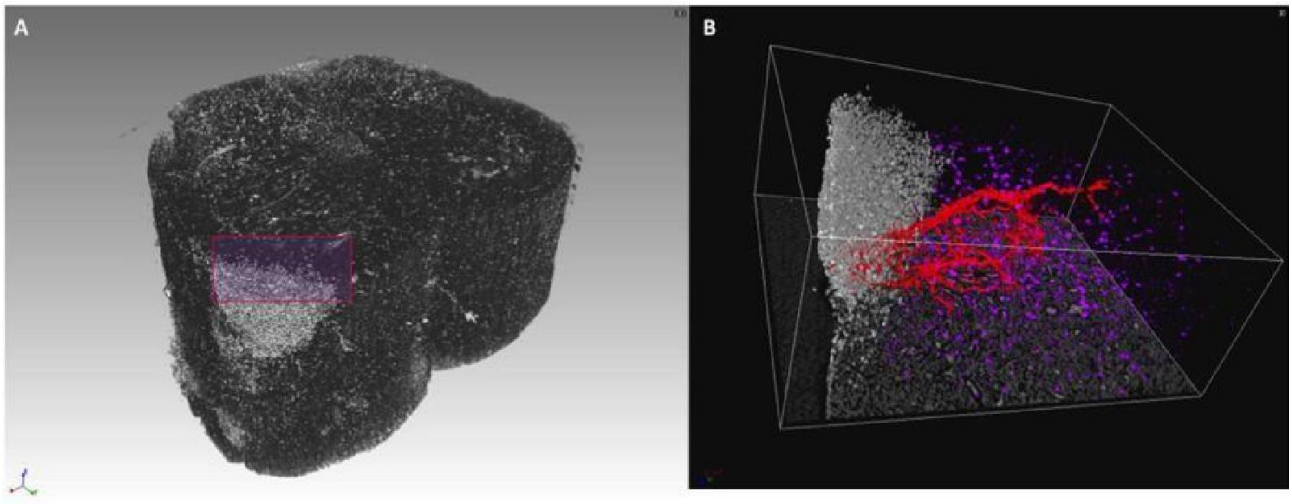

Figure 4.1: 3D rendering of lumbar spinal cord lesion in EAE-affected mouse. (A) 3D rendering of a lumbar spinal cord volume (about 1-mm in length) of EAE-affected mouse imaged with micro-XPCT at ANATOMIX, Soleil. (B) Detail of a lesion from (A) rendered and segmented.

As the first cell population to be marked, we chose astrocytes, cells involved in numerous neurodegenerative processes. For this purpose, GFAP nanobodies were purchased, conjugated ‘with gold nanoparticles of 2.5 nm in diameter, and coated with PEG molecules with a terminal carboxyl group.

4.1.1 Experimental Autoimmune encephalomyelitis (EAE) induction in mice and sample preparation

To enhance the BBB crossing by the Nano2, the mice used in this study were induced to develop experimental autoimmune encephalomyelitis, a murine model of multiple sclerosis presenting an altered BBB. This alteration, in turn, increases the permeability of the blood brain barrier and allows its crossing. Female C57BL/6 J mice (n = 14), 6–8 weeks old, weighing 18.5 g ± 0.8 g, purchased from Harlan Italy, were immunized by subcutaneous injection (200 mL total) at two sites in the flank with an emulsion of 200 mg myelin oligodendrocyte glycoprotein peptide 35–55 (Espikem) in incomplete Freund adjuvant (Difco) containing 600 mg *Mycobacterium tuberculosis* (strain H37Ra; Difco). The mice were injected (100 mL total) in the tail vein with 400 ng pertussis toxin (Sigma-Aldrich) immediately and 48 h after immunization.

Either unconjugated AuNPs or Nano2 were administered *in-vivo* either by i) intranasal or by ii) intravenous routes or *ex-vivo* locally in the cerebellum for the positive control. The mice were sacrificed by CO2 inhalation and brains were extracted at 1 and 24 h after administration. Samples designated to the XPCT measurements were dehydrated through a graded ethanol series (70/95/100%, 30 min for each step), put in propylene oxide, and finally included in paraffin. Samples designated to the confocal microscopy and X-ray LES/KES experiments were fixed in 4% paraformaldehyde for 24 h, then stored in 70% ethanol. Samples designated to the confocal microscopy were cut in the axial plan at different levels to obtain 3 to 5 sections per hemisphere. All animals were housed in pathogen-free conditions and treated according to the Italian and European guidelines (Decreto Legislativo 4 marzo 2014, n. 26, legislative transposition of Directive 2010/63/EU of the European Parliament and of the Council of 22 September 2010 on the protection of animals used for scientific purposes), with food and water *ad libitum*. The research protocol was approved by the Ethical Committee for Animal Experimentation of the University of Genoa (Prot. 319).

4.1.2 Preparation of the nanoconjugates

The surface of the ultrasmall AuNPs was first passivated with a PEG shell and then coated with Nα, Nα-Bis(carboxymethyl)-L-lysine (4.2). The nickel coordination chemistry was used to bind the anti-GFAP nanobodies, bearing a histidine tag [101]. The average number of nanobodies linked per nanoparticle was kept close to 1 in order to associate each nanoparticle to a single bio-targeting unit. The final nanoconjugate was henceforth referred to as Nano2.

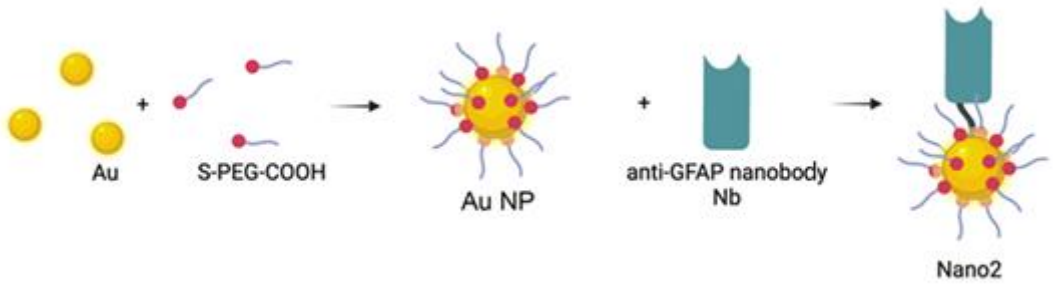

Figure 4.2 Pictorial representation of the Nano2 building blocks. Created with Biorender.com.

Table 1 reports the size (as determined by TEM and DLS measurements), the surface charge of the nanoparticles before and after conjugation of the nanobody, and the number of nanobodies linked per nanoparticle (estimated by BCA assay). Furthermore, Figure 4.3 shows the TEM image of the PEG-coated NPs, the size distribution curves and the gel electrophoretic migration of the nanoparticles with and without the nanobody attached. The DLS curve and the migration pattern confirm that the conjugation of the anti-GFAP nanobody led to a slight increase of the overall size of the nanoparticles (from 11.28 ± 0.56 to 13.97 ± 0.79 nm).

	TEM size (nm)	Hydrodynamic size (nm)	Surface charge (mV)	Number of Nb/NP
Au-PEG (2 nm)	1.67 ± 0.22	7.30 ± 0.61	- 0.14 ± 0.01	//
Au-Nb (2 nm)	1.67 ± 0.22	9.80 ± 0.57	- 25.57 ± 1.71	1.2

Table 1 Characteristics of the gold nanoparticles prior and after conjugation of the nanobody.

FTIR measures were performed to confirm the attachment of the nanobody to the nanoparticles. Thus, the starting PEG-coated and the nanobody-conjugated nanoparticles were analyzed and compared. The spectra reported in Figure 4.3 show the typical peaks of the lipoic acid-PEG carboxy acid [102] that coats the AuNP. Indeed, the signals at 1.046 and 1.100 cm^{-1} are due to the C-O stretching of the PEG chain, while at 1.405 the bending frequency of the O-H group of carboxylic acid can be observed. The vibrations at 1.565 and 1,640 cm^{-1} can be assigned to C-N stretching and N-H bending, respectively, of the amide group of the lipoic acid anchored to the gold surface. The FTIR spectrum of Nano2 shows more peaks due to the vibrations of the side groups of the aminoacids of the nanobody [103]. The aminoacids sequence and the CDR domains of the nanobody are reported in [101]. The strong peak at 1.106 cm^{-1} is likely due to the C-H bending and the C-N stretching of Histidine, respectively. The signal at 1.245 cm^{-1} is typical of C-N stretching of Glutamine and Arginine, while the peaks at 1,352 and 1.362 cm^{-1} belong to the C-N stretching and C-H bending vibration (CH) of the benzene ring of Trypthophan. The signal at 1.460 cm^{-1} can be assigned to

the C-H bending of Phenylalanine, while the sharp peak at 1.512 cm^{-1} can be related to the C-C stretching and C-H bending CH of the aromatic ring of Tyrosine, respectively.

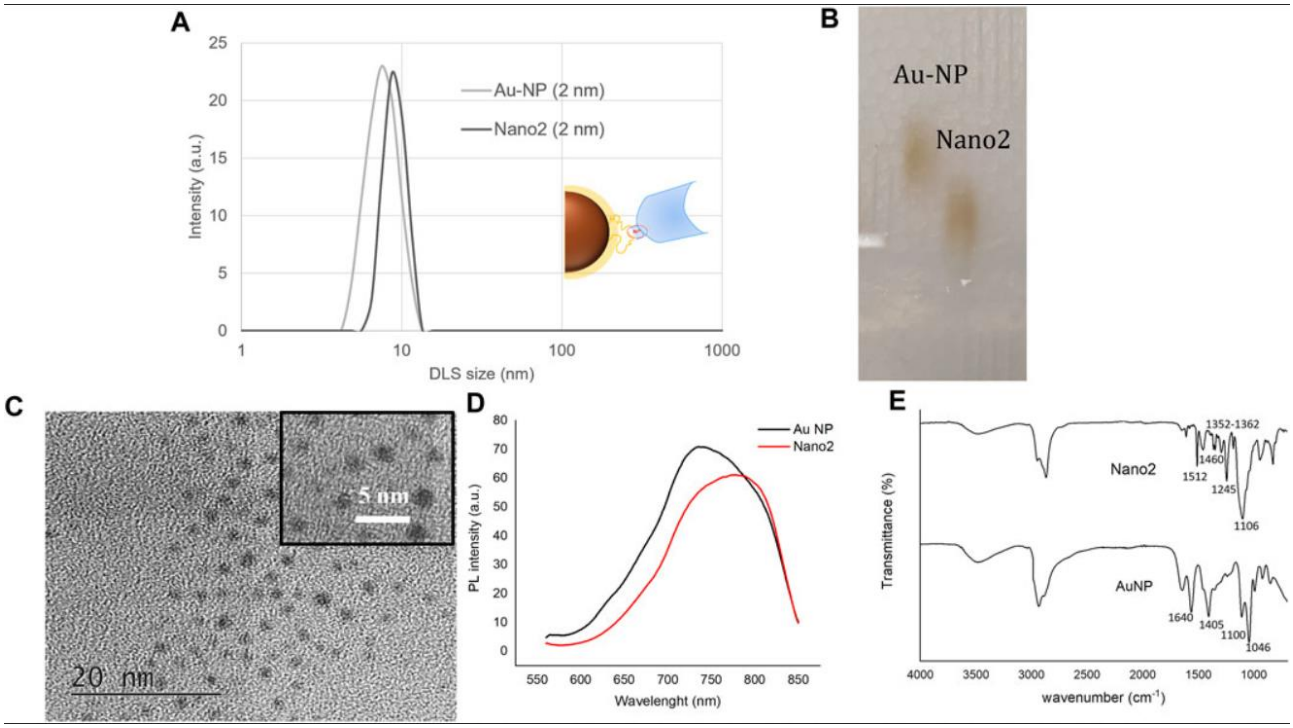

Figure 4.3 (A) Hydrodynamic diameter and (B) electrophoretic mobility of Au NP and Nano2. (C) TEM image of the 2 nm-sized Au NP; (D) Luminescence spectra of Au NP and Nano2, respectively. The Hydrodynamic measures were acquired using a Zetasizer Nano ZS90 Malvern, while a Jeol JEM 1400 and a Cary Eclipse were used for TEM and fluorescence analysis; (E) FTIR spectra of AuNP and Nano2, respectively.

Furthermore, the luminescence spectra of the nanoparticles before and after the nanobody binding were recorded. As shown in Figure 4.3 D, the luminescence peak shifts from 738 nm to 778 nm and the whole curve looks broadened upon nanobody conjugation. The photoluminescence (PL) intensity is also reduced, likely due to energy transfer processes between the Au surface and the nanobody, as already described [104].

4.1.3 Nano2-GFAP binding

The binding specificity of Nano2 to its biological target, the cytoplasmic protein GFAP, was extensively evaluated. To this aim, a simple optical device based on plasmonic localized surface plasmon resonance (LSPR) detection was setup [105]. The measure is based on the local change of the dielectric environment on the metal nanostructure surface [106]. Since the 2 nm-sized gold nanoparticles used throughout this study do not display a plasmon peak due to their small size, larger Au nanoparticles (5.5 nm sized, Abs peak at 525 nm) functionalized with the same chemistry and conjugated to the anti-GFAP nanobody were prepared and characterized.

	TEM size (nm)	Hydrodynamic size (nm)	Surface charge (mV)	Number of Nb/NP
Au-PEG (5.5 nm)	5.59 ± 1.16	11.28 ± 0.56	- 0.11 ± 0.01	//
Au-Nb (5.5 nm)	5.59 ± 1.16	13.97 ± 0.79	- 24.70 ± 1.71	1.4

Table 2 Characteristics of the 5.5 nm-sized gold nanoparticles prior and after conjugation of the nanobody.

Table 2 and Figure 4.4 report the main physicochemical characterization of the NPs.

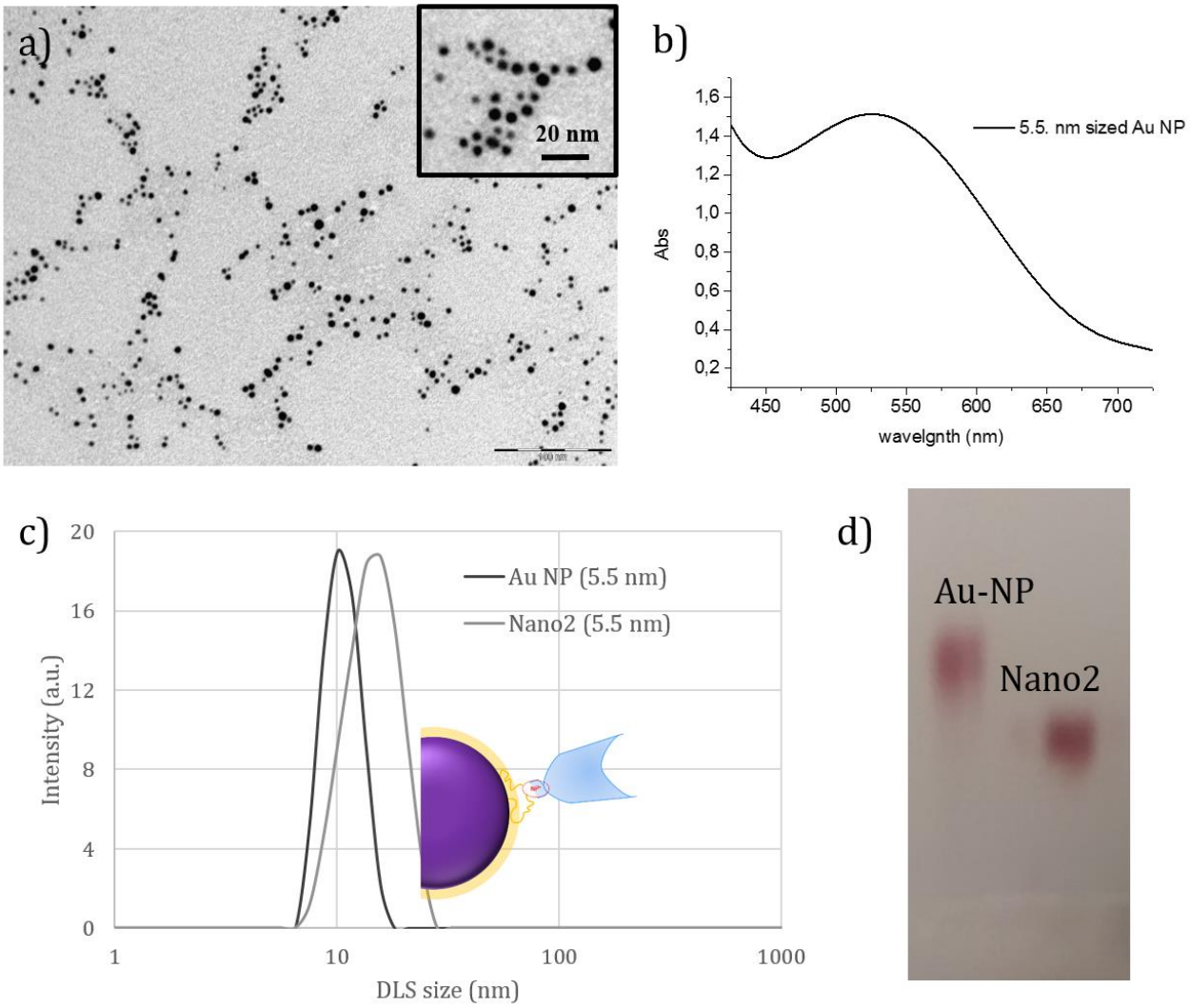

Figure 4.4 (a)-(b) TEM image and absorption spectrum of the 5.5 nm-sized Au NP; c) and d) Hydrodynamic diameter and electrophoretic mobility before and after the nanobody conjugation, respectively. The Hydrodynamic measures were acquired using a Zetasizer Nano ZS90

In detail, glass slides functionalized with the GFAP antigen were incubated with Nano2 (10 nM) for 1 h (sample 1). To evaluate the specific binding between the antigen and Nano2, three other interfaces were analyzed in parallel: glass slide functionalized with GFAP antigen and incubated with 5.5 nm AuNPs (sample 2), and glass slides coated with BSA and incubated with either Nano2 (sample 3) or AuNPs (sample 4), respectively. The extinction curves of the glass slides upon incubation were collected and analyzed. Figure 4.5 reports the plasmon peaks of the samples showing that a red-shift (around 10 nm) is detected only in sample 1, likely due to the establishment of specific interactions

between Nano2 and the immobilized antigen. Finally, the signal to noise ratio was estimated to be 12 times higher in sample 1 than in sample 3.

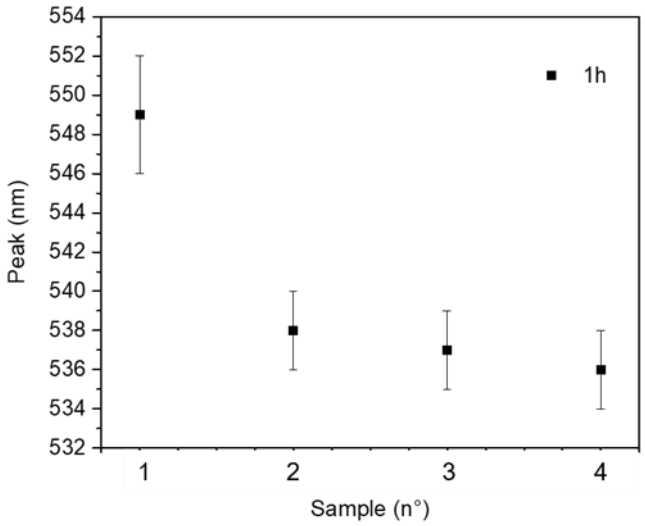

Figure 4.5 Au plasmon peak of Nano2 at glass-GFAP (sample 1), Au-NPs at glass-GFAP (sample 2), Nano2 at glass-BSA (sample 3), AuNPs at glass-BSA (sample 4) after 1 h incubation.

At this point we were sure to have a stable complex composed by Au nanoparticles with a diameter of about 2 nm and GFAP nanobody able to specifically bind the cytoplasmic protein GFAP.

This complex, Nano2, were used for the next tests.

4.1.4 Method of administration of Nano2

We tested two different administration routes of Nano2 in order to find the one leading to the best diffusion and highest retention in the brain. We also compared the NPs and the Nano2 distributions. To facilitate the crossing of Nano2 through the brain, we tested Nano2 in a mouse model of multiple sclerosis, experimental autoimmune encephalomyelitis, characterized by BBB disruption resulting

from neuroinflammation. Experimentally, either unconjugated AuNPs or Nano2 were administered *in-vivo* either by 1) intranasal (IN) or by 2) intravenous (IV) routes or *ex-vivo* locally in the cerebellum for the positive control (CTRL+). For the positive control, naïve mice with intact BBB were used. Figure 4.6 summarizes the analyzed samples. Names of the mice groups are reported in.

A

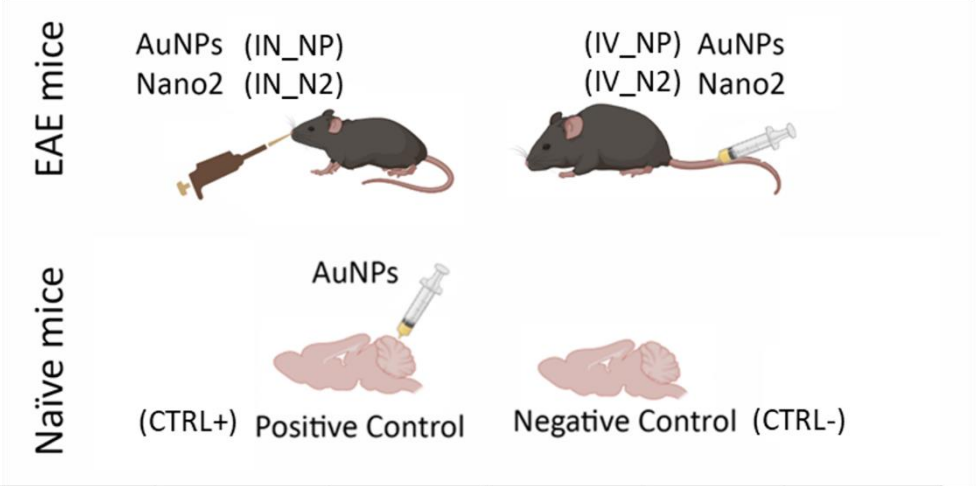

B

IN_NP	IN_N2	IV_NP	IV_N2	CTRL+	CTRL-
EAE mice intranasal administration of Au NPs	EAE mice intranasal administration of Nano2	EAE mice intravenous administration of Au NPs	EAE mice intravenous administration of Nano2	Naïve mice local injection of Au NPs in the cerebellum	Naïve mice without injection

Figure 4.6 The different groups of analyzed mice: (A) The different routes of administration; (B) Details of the groups. Created with Biorender.com.

After the administration of the compounds, brains isolated from the euthanized mice were dissected into two parts: one hemisphere was imaged with LES and KES experiments, the other was analyzed by confocal microscopy. The fluorescence of the AuNPs was mapped in red on sections in which cell nuclei were marked in blue. In control conditions, only 3 sections were analysed, while in the presence of AuNCs (alone or coupled to the nanobody) more than 5 sections were analysed. The AuNCs were mainly localized in a restricted area close to the cerebellum, the hypothalamus and in the first third of the lower part of the brain.

Intranasal administration of Nano2 displayed higher retention in the brain than intravenous injection of Nano2, as shown in Figures 4.7 A, B. After intravenous administration, we managed to find AuNCs on only 1 or 2 sections at one specific part, while they were always presented and diffused after IN administration.

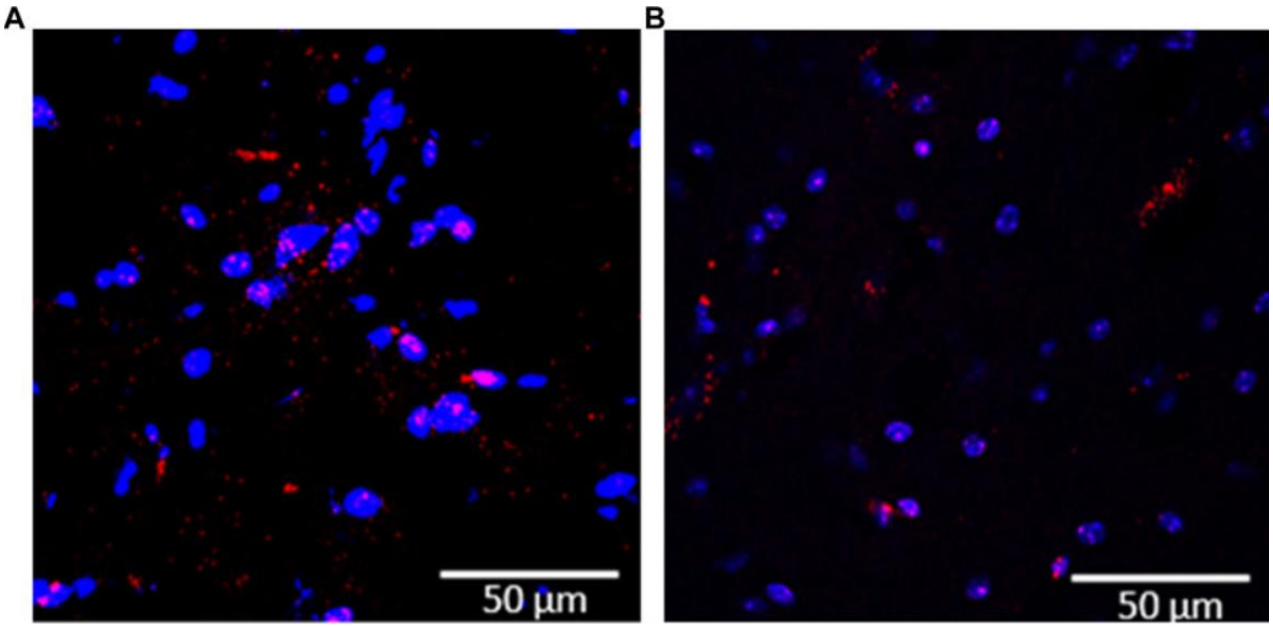

Figure 4.7 Confocal imaging of brain sections from EAE mice. Comparison between intranasal (A) and intravenous (B) administration of Nano2 in the brain. Fluorescence of the AuNPs in red, cells nuclei in blue.

Furthermore, the comparison between intranasal administration of Nano2 and unconjugated NPs (Figure 4.8 A and B respectively) indicated a greatest retention of Nano2 in the brain sections versus unconjugated NPs. NPs alone were very rarely observed in the different sections, regardless of the intranasal or intravenous administration route.

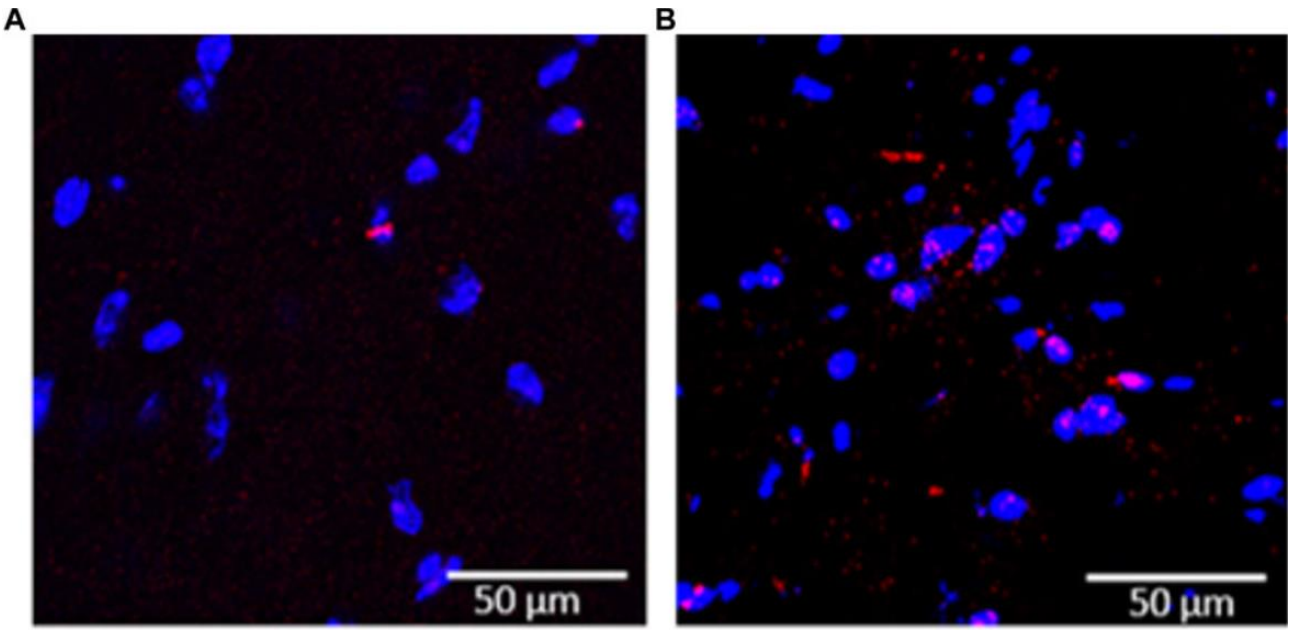

Figure 4.8 Confocal imaging of brain sections from EAE mice. Comparison between intranasal administration of (A) unconjugated NPs and (B) Nano2. Fluorescence of the AuNPs in red, cell nuclei in blue.

Results described indicate that the intranasal administration allows a good distribution of Nano2 in the brain. High retention in the brain increases the possibility to identify the clusters with other imaging techniques. XPCT, for example, requires clusters with micrometric dimensions distributed within the brain to detect them. From these tests intranasal administration was selected for the next steps.

4.1.5 Validation of the targeting

The correct targeting of the astrocytes by Nano2 was validated on brain sections by confocal fluorescence microscopy. The specific AuNPs used in this study are ultra-small NP that naturally emit a tunable fluorescent signal, allowing their detection by confocal fluorescence (Porret et al., 2017). Therefore, by detecting the Au, the anti-astrocyte monoclonal antibody was detected, and thus, the astrocytes could be identified.

In order to verify the targeting capacity of the Nano2, we analyzed the brains of IN_N2 mice, i.e., mice administered with Nano2 intranasally, by confocal microscopy using anti-Glast Nb to mark the astrocytes, as reported in Figure 4.9. Nano2 were detected in the brain sections due to the presence of the AuNPs which are fluorescent in the near infrared optical region after blue light excitation. In Figure 4.9 fluorescence of the AuNPs is shown in red, astrocytes in green and the arrows indicate the colocalization between Nano2 and Glast-expressing cells.

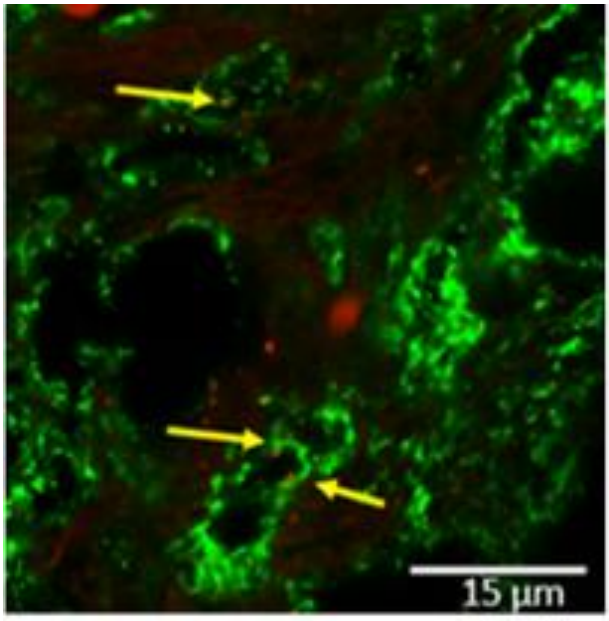

Figure 4.9 Confocal imaging of brain sections from EAE mice of a IN_N2—anti-Glast immunolabelling, the arrows indicate colocalization between Nano2 and Glast-expressing cells. Fluorescence of the AuNPs in red, astrocytes in green.

After intranasal administration of Nano2, colocalizations between Nano2 and Glast-expressing cells were observed, thus indicating the possibility of specifically targeting the astrocytes.

These tests tell us that the complex we created is stable, crosses the BBB and reaches the astrocytes.

The points indicated by the yellow arrows in Figure 4.9 show a colocalization between the nanobody and the Glast-expressing cell; the fact that the colocalization is visible in fluorescence means that the

nanobody is linked to the metal nanoparticle, and so that the nanoconjugate binding is stable and reached the cell of interest.

4.1.6 X-Ray Imaging

As described in the previous sections, the first tests focused on the functionalization and conjugation of gold nanoparticles with nanobodies, to then assess their ability to cross the BBB and reach astrocytes. Once these initial experiments had been carried out, we began to verify the feasibility of detection using x-ray imaging techniques. The final goal of the thesis, indeed, is to identify cells with X-Ray Phase Contrast Tomography exploiting the characteristics of the metal nanoparticles and of the nanobodies. This implemented technique should be applied to *ex-vivo* and *in-vivo* experiments.

L-Edge subtraction experiment

As first test, we performed an L-Edge subtraction experiment.

In agreement with the results obtained from the previous tests, Nano2 complex was intranasally administrated to EAE mice. In this way we were sure to have a good distribution and cells selectivity within the volume. The brains were then extracted and sliced in 16 slabs, 1 mm-thick each.

On these samples we performed an L-Edge subtraction X-Ray phase contrast radiography (XPCR) at ELETTRA beamline SYRMEP. Experimental details are reported in the Appendix at the end of the manuscript and in Table 3.

LES experiment	
Energy	Monochromatic, 11.9-12 keV
Distance	50 cm
Detector	Pco.EDGE 5.5
Optics	/
FOV (HxV)	/
Pixel Size	1.98 μm
# Projections	10
Mode	Radiography
Exposure Time	10 s

Table 3 LES Experiment parameters

As described in the dedicated section, two images are acquired at energies bracketing the L-Edge energy of gold (11.9 keV). The difference in contrast between the two images is mainly due to the different absorption of the metal at the two energies. By subtracting the obtained radiographies, it is possible to highlight the Au presence within the sample.

Figure 4.10 A shows the result obtained after the image subtraction; the yellow arrows indicate white spots of signal from Au that therefore likely represent clusters of Nano2.

On the same sample a confocal microscopy measurement was performed. In Figure 4.10 B the arrows indicate the points where the photoluminescence signal of Au is significant.

ImageJ software was used to co-registrate the XPCR-LES and the confocal microscopy images.

Figure 4.10 C reports the co-registration result, showing the correspondence between the signals coming from the two different techniques.

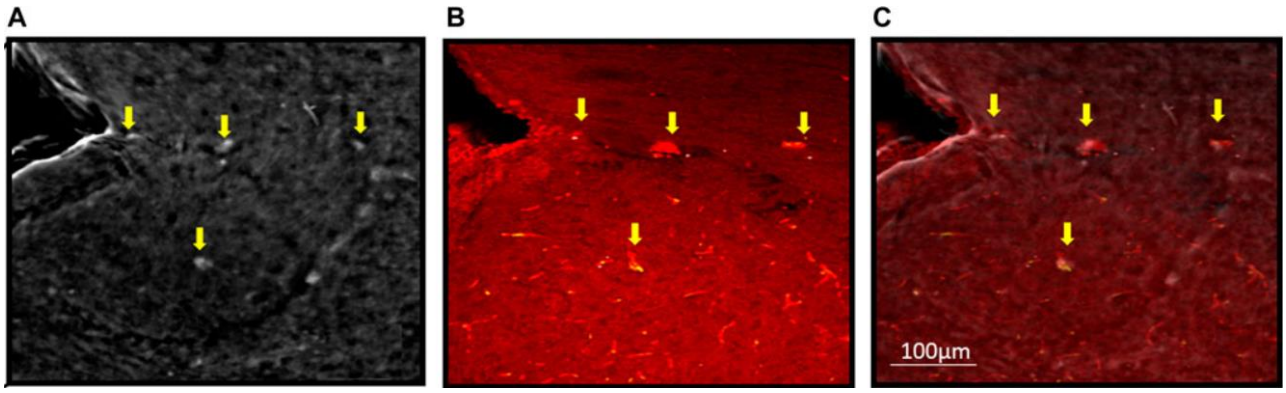

Figure 4.10 (A) X-ray phase contrast radiography (XPCR), the image is obtained by subtracting an image acquired just above and one just below the L-edge of Au. The arrows indicate possible Nano2 accumulations; (B) Confocal microscopy image, in reflection mode of the same slice in Figure (A). The arrows indicate the points with Au significant emission signal; (C) Co-registration of (A) and (B) where the arrows indicate possible Nano2 accumulations, for the co-registration the software ImageJ was used, scale bar: 100 µm.

From this experiment we can see that XPCR is able to detect the signal coming from Au clusters. The source of the signal has two proofs: the first one comes from the LES technique, which only reveals the signal coming from the metal, the second one arrives from the co-registration with the confocal microscopy images, in which we are sure that the photoluminescence signal is the one of the Au.

The information provided by the LES experiment were very useful as starting point for the X-ray imaging exploration. This test also presented me with my first challenges related to subtraction imaging and co-registration. The subtraction between the image acquired above and the one acquired below the Au L-Edge gives information only if it is performed exactly pixel per pixel; if a movement

occurs in the time between the two acquisitions, it is necessary to restore the exact pixel correspondence before the subtraction to obtain a valid result. Regarding the co-registration with the confocal microscopy images, the challenge concerned the acquisition plane. The brain slabs presented irregular surfaces and in the two different techniques acquisitions we were not sure about the perfect orthogonality of the sample with the beam. The first step of the co-registration was, therefore, the plane alignment of the XCPT and of the confocal images.

LES experiment results gave us information about the detectability of Nano2, but they were limited to 2D imaging. Next step involved 3D imaging, to test the technique in the entire brain volume.

K-Edge subtraction experiment

After the LES experiment, in order to evaluate the detectability and the distribution of the Nano2 complex in the volume, brains from EAE mice after an intranasal administration were extracted and measured in a K-Edge subtraction X-Ray phase contrast tomography experiment at ID17 beamline of ESRF. As in the previous experiment, the sample was imaged at two different energies, above and below the K-Edge of gold (80.7 keV), respectively.

The parameters of the experiment are reported in the Appendix at the end of the manuscript and in Table 4.

KES Experiment	
Energy	Monochromatic, above and below 80.7 keV
Distance	2.3 m
Detector	PCO.Edge 5.5
Optics	2x
FOV (HxV)	5.0 mm x 6.0 mm
Pixel Size	3.05 μm
# Projections	3500
Acquisition Mode	180°
Exposure Time per frame	300 ms

Table 4 KES experiment parameters

The subtraction images (Fig 4.11 A) clearly show bright spots, coming from the Au signal. These points can be traced back to the presence of Nano2 clusters. Their distribution along the blood vessels is also visible in the 3D rendering of a mouse brain volume shown in Figure 4.12. The 3D image helps the visualization of the spatial distribution of the Nano2 clusters (yellow) inside the brain and shows their accumulation along the blood vessels (red). This distribution is in accordance with what is reported in literature.

The comparison with the Z-stack confocal microscopy images (B) from the other hemisphere of the same sample supports this interpretation; in fact, in Figure 4.11 B, the Au emission signal (yellow in the color scale) is clearly visible near the vessels.

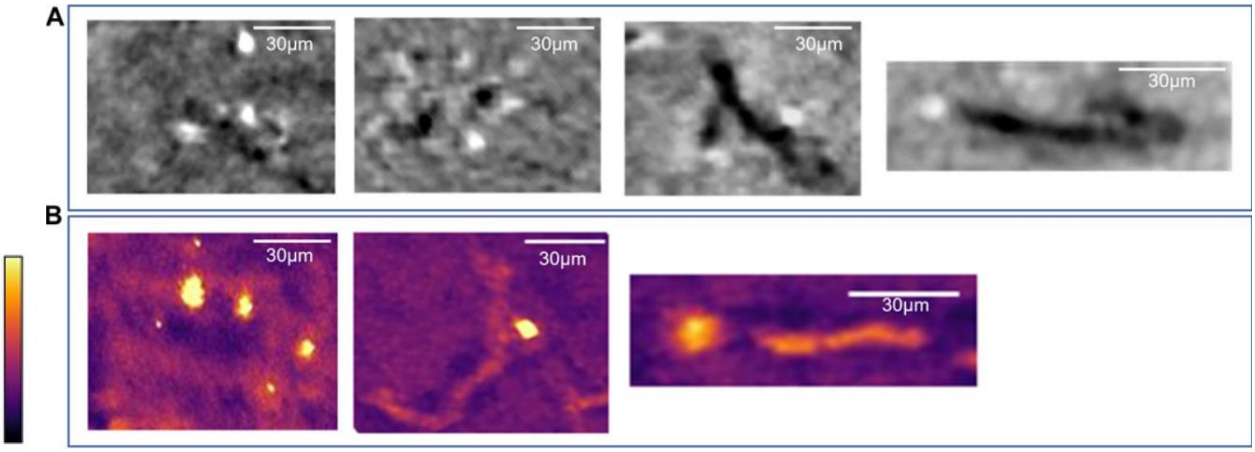

Figure 4.11 Vessels cross sections of a IN_N2 mouse. (A) Tomographic Au-K-edge Subtraction images. (B) Confocal microscopy images. In the color scale the yellow corresponds to the Au emission signal. Scale bar: 30 µm.

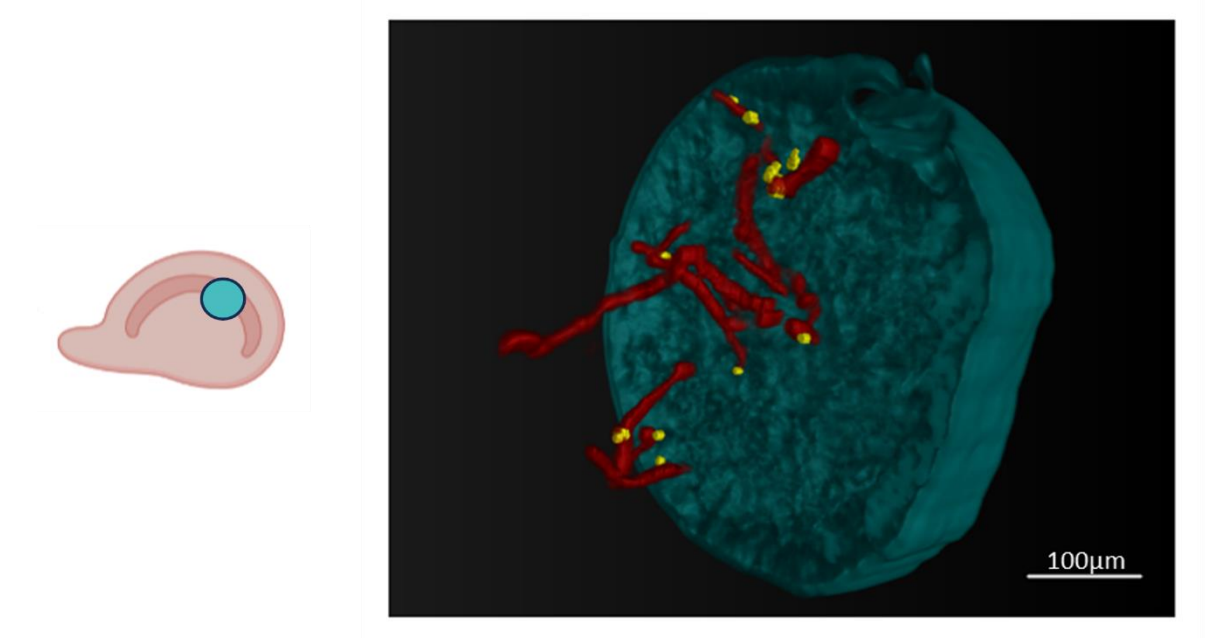

Figure 4.12 3D rendering of a K-Edge subtraction volume from an intranasally administrated sample (IN_N2). Nano2 clusters (yellow) appear near the blood vessels (red). The experiment was performed at the ID17 beamline of the ESRF (Grenoble, France) using two different energies, bracketing the K-edge of the gold, with a voxel size of about 3 µm. Scale bar: 100 µm.

With the KES experiment I faced the volumes alignment problem. The volume imaged above and the one imaged below the Au K-Edge were not perfectly aligned. This problem comes from the fact that the two-energies acquisitions are not simultaneous. Despite the sample wasn't moved between the measurements, the tomography starting point was not exactly the same because of the limited motors' precision. This movement artifact is solvable in the image post processing phase. Another problem is the shrinking of the brain during the measurements. The sample under the beam dries out and this leads to have different sample size and coordinates in the two measurements above and below the K-edge. I avoided this problem performing again the two experiments once the samples were completely dried.

X-Ray phase contrast tomography experiment

LES and KES experiments gave us information about the presence of the Nano2 complex inside the brain. By performing these experiments in phase contrast mode, we also obtained information about the tissue and the vasculature, and consequently we had information about the distribution of the nanobody-conjugate within the organ. Our distribution results are confirmed in literature: nanoparticles lie along the blood vessels and we can find Nano2 in these regions, where astrocytes are present.

In the next step, different X-Ray phase contrast tomography tests were performed in order to assess the optimal procedure to carry out the experiments.

First experiments were conducted at TOMCAT beamline of SLS on EAE mice treated in the following ways:

- Intranasally administered with 5, 10 or 20 µl of nanoparticles
- Intranasally administered with 5, 10 or 20 µl of Nano2
- Intravenously injected with 5, 10 or 20 µl of nanoparticles
- Intravenously injected with 5, 10 or 20 µl of Nano2
- Direct injection of 5, 10 or 20 µl of nanoparticles in the cerebellum.

The parameters of the experiment are reported in the Appendix at the end of the manuscript and in Table 5.

XPCT experiment	
Energy	Monochromatic, 17 keV
Distance	5 cm
Detector	Pco.EDGE 5.5
Optics	4x
FOV (HxV)	4.16 mm x 3.51 mm
Pixel Size	1.625 μm
# Projections	3000
Mode	Half acquisition (360°)
Exposure Time	50 ms

Table 5 XPCT experiment parameters

Figure 4.13 shows the results of the most successful and significative test: intranasal administration of 20 µl of Nano2. With this configuration distribution and signal were optimal.

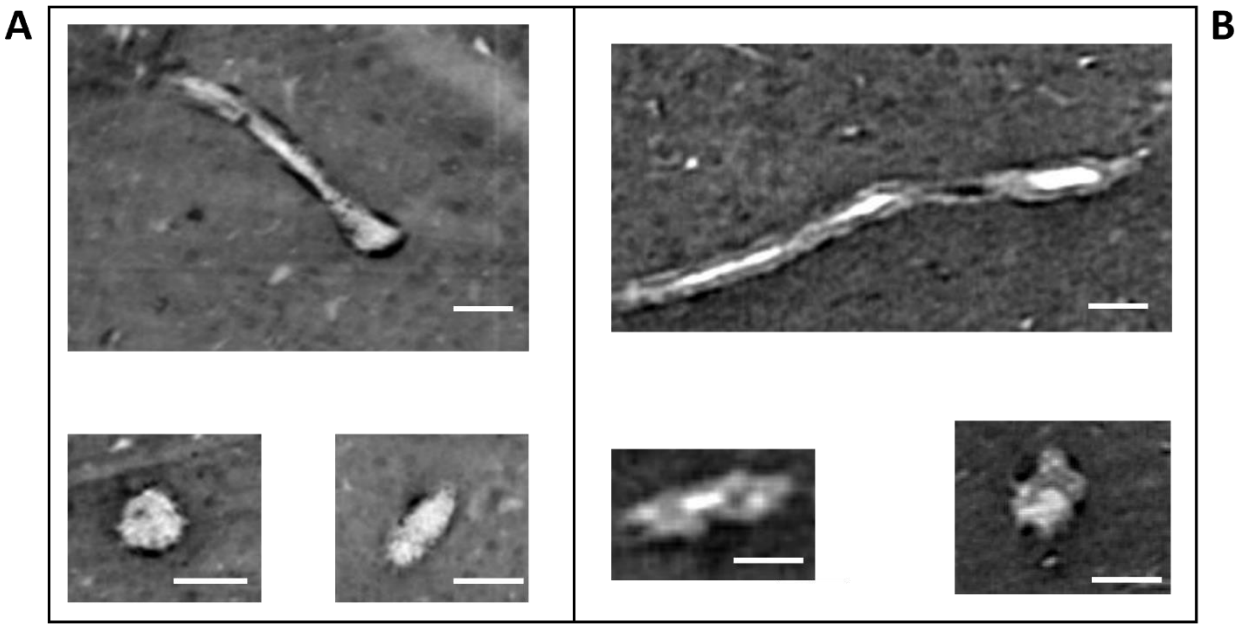

Figure 4.13 (A) Blood vessels XPCT cross sections of control sample, (B) Blood vessels XPCT cross section of Nano2 administered sample. Scale bar 25 µm.

From the comparison between the administrated sample (Fig 4.13 B) and the control one, it is possible to see how in the treated mouse brain the blood vessels present a halo at the edge with some bright spots, not visible in the sample not administrated (Fig 4.13 A).

The same comparison was made on confocal microscopy images.

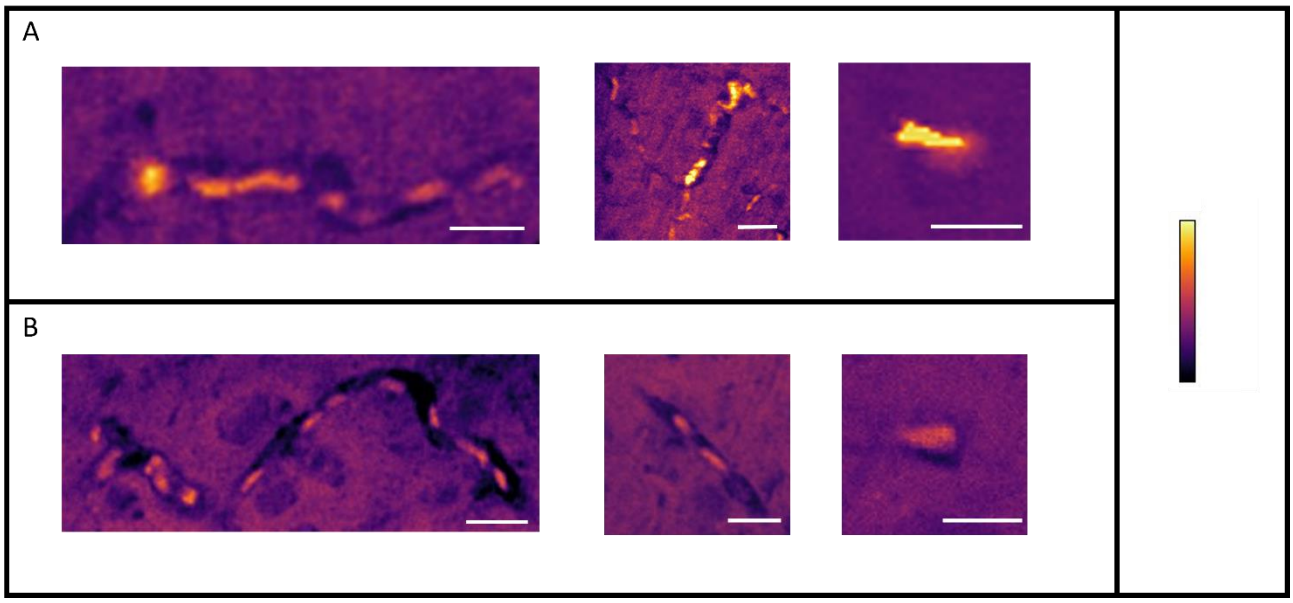

Figure 4.14 (A) Blood vessels confocal microscopy cross sections of control sample, (B) Blood vessels confocal microscopy cross section of Nano2 administered sample. Scale bar 30 µm.

In Figure 4.14 it is possible to appreciate how Au signal (yellow in the color scale) coming from the Nano2 complex is present along the blood vessels in the brain of the administrated mouse and the differences between the two samples.

Next step involved naïve mice, in order to test the capability of the nanobody-conjugate to cross the blood-brain-barrier and to spread within the brain in physiological conditions, without imposed alterations.

I examined mice subjected to the following preparation methods:

- Intravenous injection of 5, 10 or 20 µl of nanoparticles
- Intravenous injection of 5, 10 or 20 µl of Nano2
- Intranasal administration of 5, 10 or 20 µl of nanoparticles
- Intranasal administration of 5, 10 or 20 µl of Nano2
- Direct injection of 5, 10 or 20 µl of nanoparticles in the cerebellum.

In Figure 4.15 the results of an acquisition on a healthy mouse brain extracted after an intranasal administration of 20 µl of Nano2

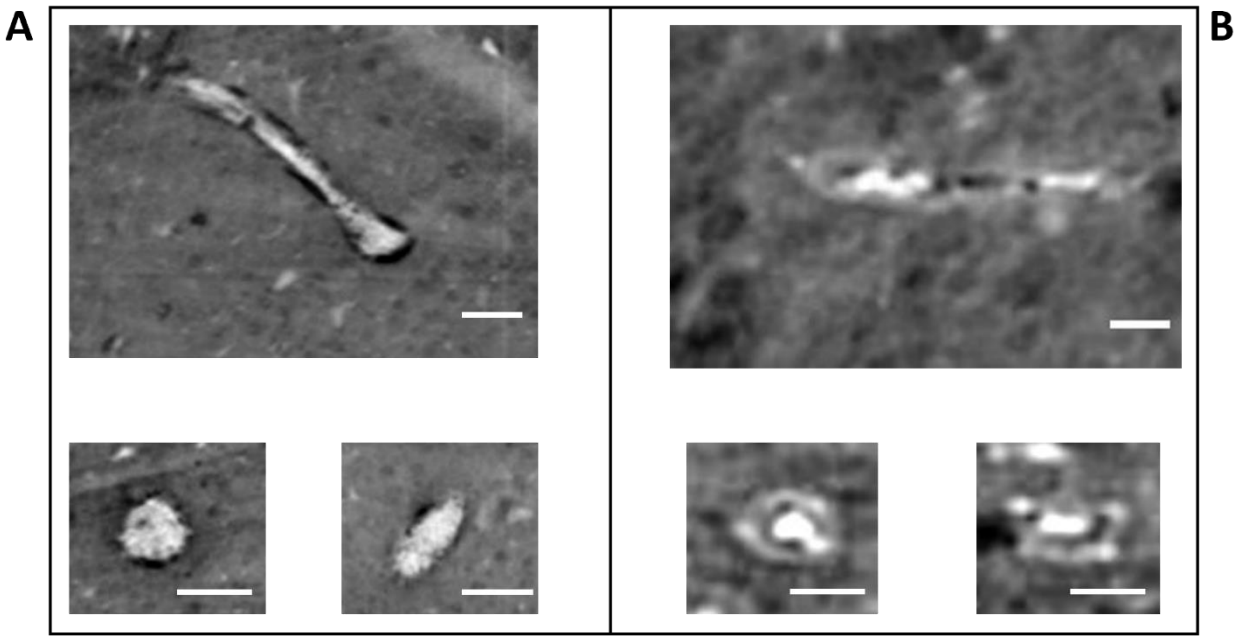

Figure 4.15 (A) Blood vessels XPCT cross sections of control sample, (B) Blood vessels XPCT cross section of Nano2 administered sample. Scale bar 25 µm.

Figure 4.15 (B) shows that also in the mice with a non-altered BBB, after the intranasal administration of 20 µl of Nano2 the blood vessels present a halo at the border with white spots. Bright elements correspond to dense materials, and so we can reconduct this contrast signal to the presence of nanoparticles and consequently of Nano2. The control sample, not administered, doesn't show this blood vessels' behavior. Vessels in Figure 4.15 A have defined edge without any halo, indicating that what we can see in the other sample is due to the Nano2 administration.

This experiment permitted us to understand that Nano2 cross the BBB and spread within the brain also in a non-altered environment and accumulate in the blood vessels' regions, again in accordance with the literature on nanoparticles and astrocytes distribution in the brain.

Despite these initial significant results, the pixel size of 3 µm with which the images described in this section were acquired does not allow for a confident assertion of the presence of Nano2, nor even a correct labeling of cells of interest.

With this motivation we performed other experiments at higher resolution.

Synchrotron radiation holo-nano-tomography

From XPCT experiments we observed that Nano2 cross the BBB when it is altered and when it is intact, allowing the use of this technique in both physiological and pathological condition. With the correct amount of administered complex, we are able to appreciate differences between the treated and the control sample, in fact the presence of a halo surrounding the blood vessels of the Nano2 administered mouse is a visible detail due to the treatment. However, to achieve the purpose of this thesis work, measurements at higher resolution were necessary. From the XPCT results, indeed, we are not able to identify the cells of interest, in this case the astrocytes, and we don't have an unconfutable proof of the presence of Nano2.

First experiment was carried out at ID16 beamline of ESRF on EAE mice intranasally administrated with Nano2. Experimental parameters are reported in the Appendix at the end of the manuscript and in Table 6.

Holo-nano-tomography experiment	
Energy	17 keV *(divergent beam)*
Distance	225mm, 175mm, 75 mm, 45mm
Detector	FReLoN CCD
Optics	multilayer coated Kirkpatrick-Baez mirrors
FOV	/
Pixel Size	190 nm, 40 nm
# Projections	1500

Table 6 Holo-nano-tomography experiment parameters

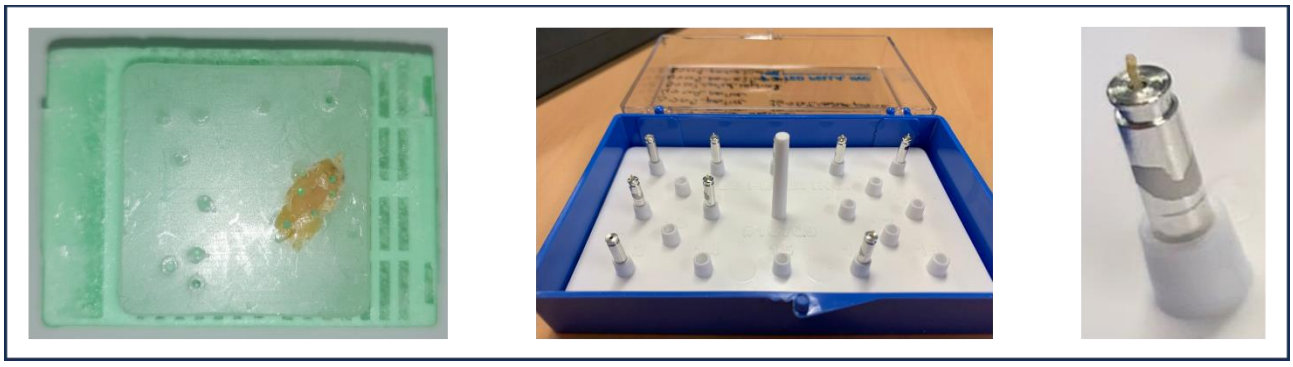

Figure 4.16 Sample preparation pictures. From the left: punched hemibrain embedded in paraffin, samples mounted on metallic pins in a box, detail of the mounted sample.

Cylinder of 500 µm in diameter were punched from a hemibrain embedded in paraffin (Fig 4.16) and measured with two pixel sizes: 190 nm and 40 nm.

Fig 4.17 shows how the images collected in this holo-nano-tomography experiment are fully comparable with histological results. From this comparison it is clear that to validate our technique the nanometric scale is needed. Only with a resolution of nanometers we are able to distinguish cells and nanoclusters.

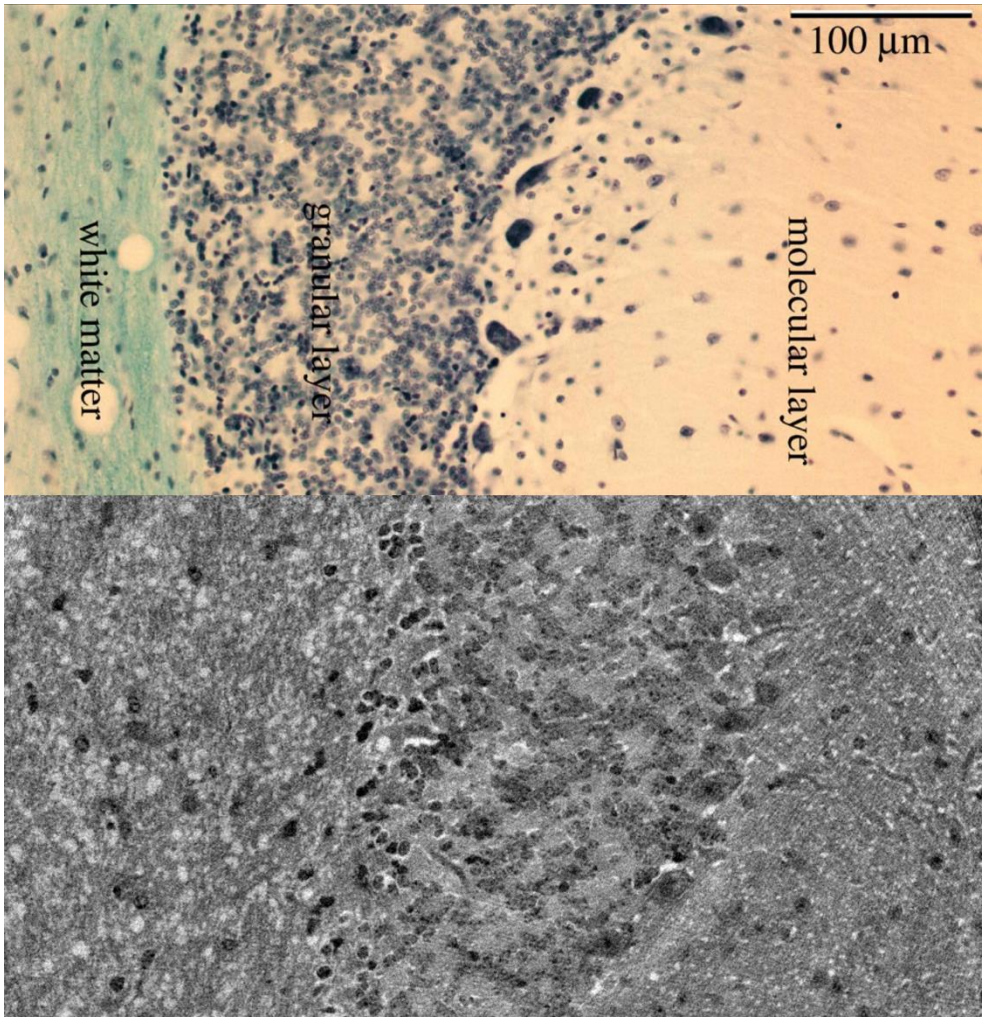

Figure 4.17 Comparison between histological (top) and tomographic (bottom) images of brain tissue. Histological image from http://faculty.cord.edu/todt/336/lab/nervous/cerebellum/cerebellum2.htm

In figure 4.18 there are indicated with arrows some bright spots present in the acquisition at low resolution (190 nm of pixel size) and in the one at high resolution (40 nm of pixel size).

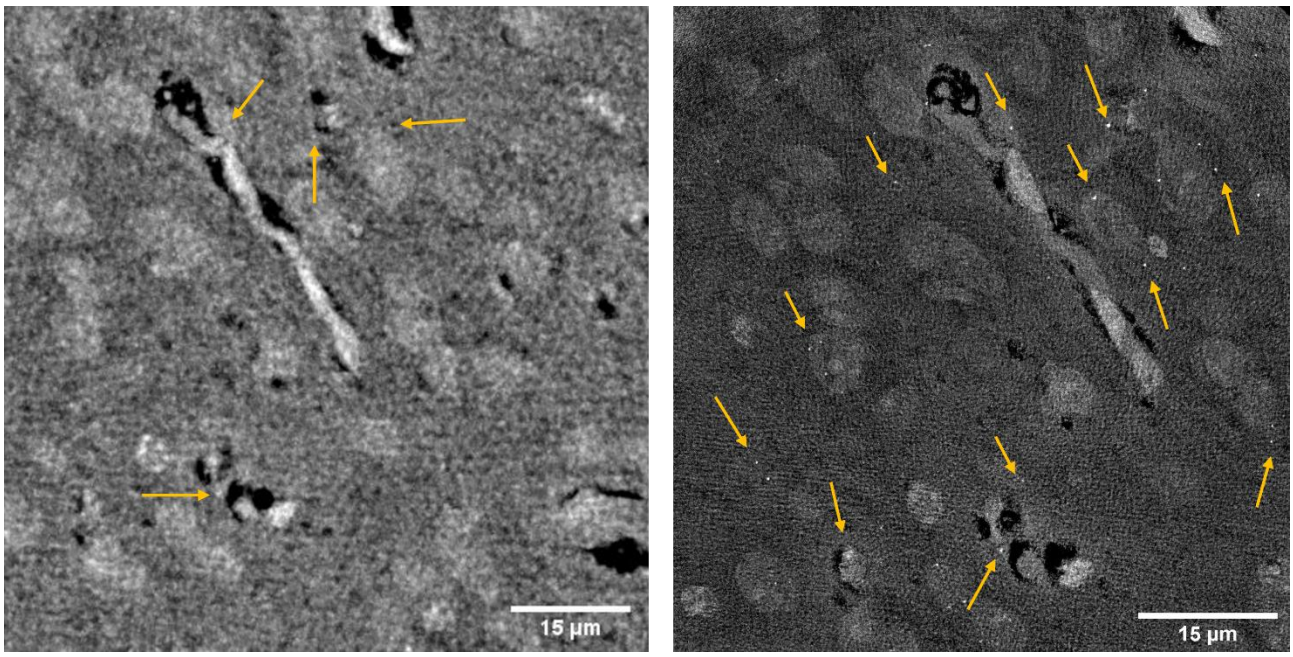

Figure 4.18 Holo-nano-tomographic acquisition on an administrated mouse with 190 nm (left) and 40 nm of pixel size (right). Yellow arrows indicate bright points compatible with the presence of Nano2 clusters.

High resolution image permits to observe different points compatible with the presence of Nano2 clusters. The visualization of these spots is possible after a denoising procedure allowing to remove the background noise and highlight the real signal.

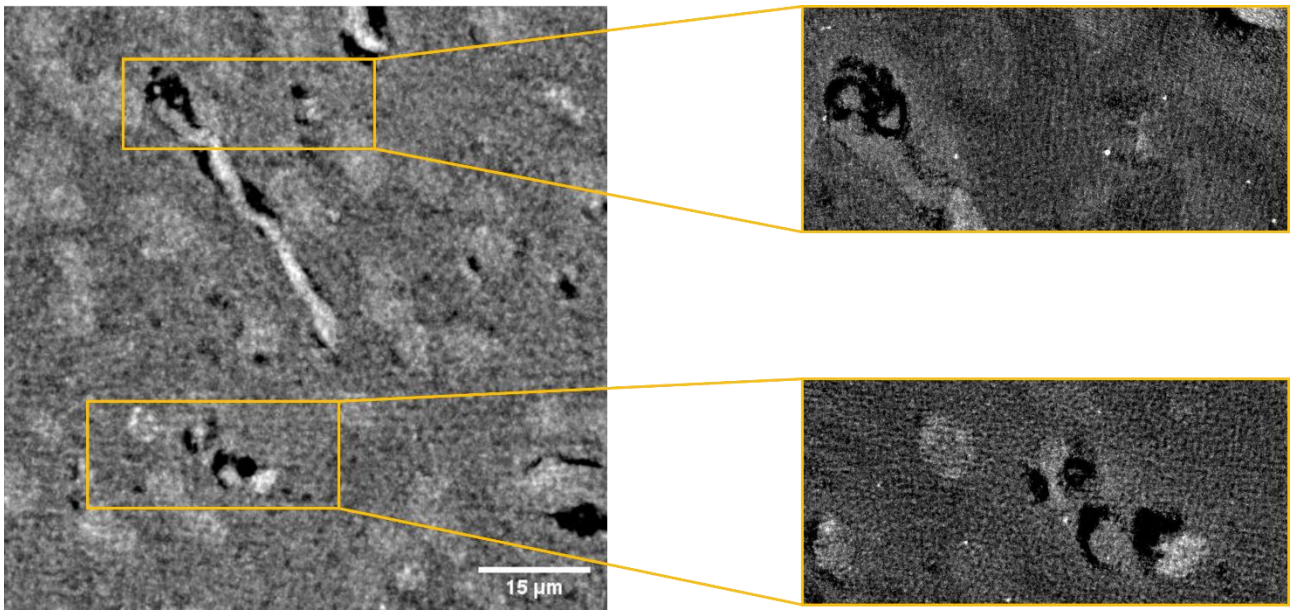

Figure 4.19 Holo-nano-tomographic acquisition on an administrated mouse with 190 nm of pixel size. In the insights (yellow boxes), same areas scanned with 40 nm of pixel size.

In figure 4.20 a segmentation is presented in which white spots are clearly visible with respect to the tissue, segmented in orange, the cells and the blood vessels, segmented in purple.

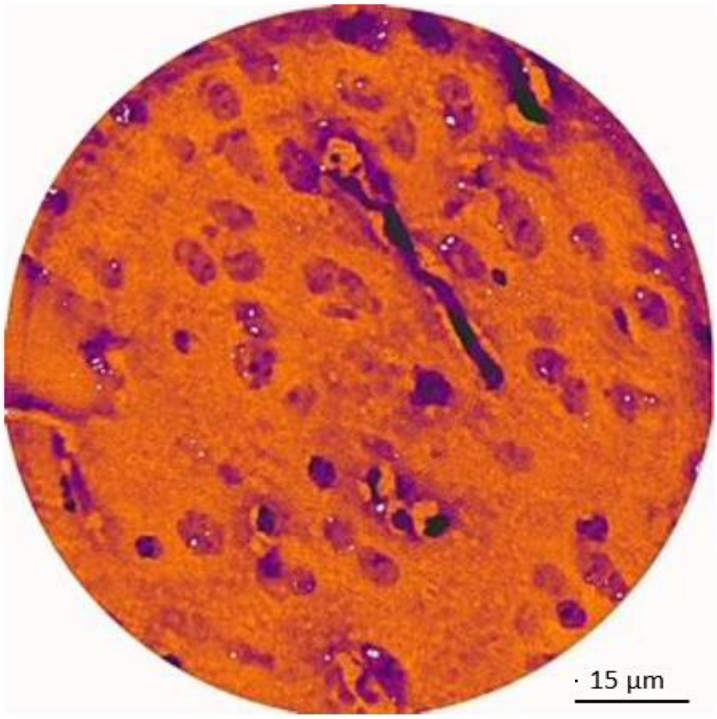

Figure 4.20 Nano-holo-tomography images. Clearly visible cells (purple), a vessel (dark purple) and white spots compatible with the presence of Au-Nano2 clusters. Scale bar 15 μm

On the same brain sample, confocal microscopy measurements were performed and compared with the tomographic images to better understand if the signal in the latter was compatible with the one coming from the gold.

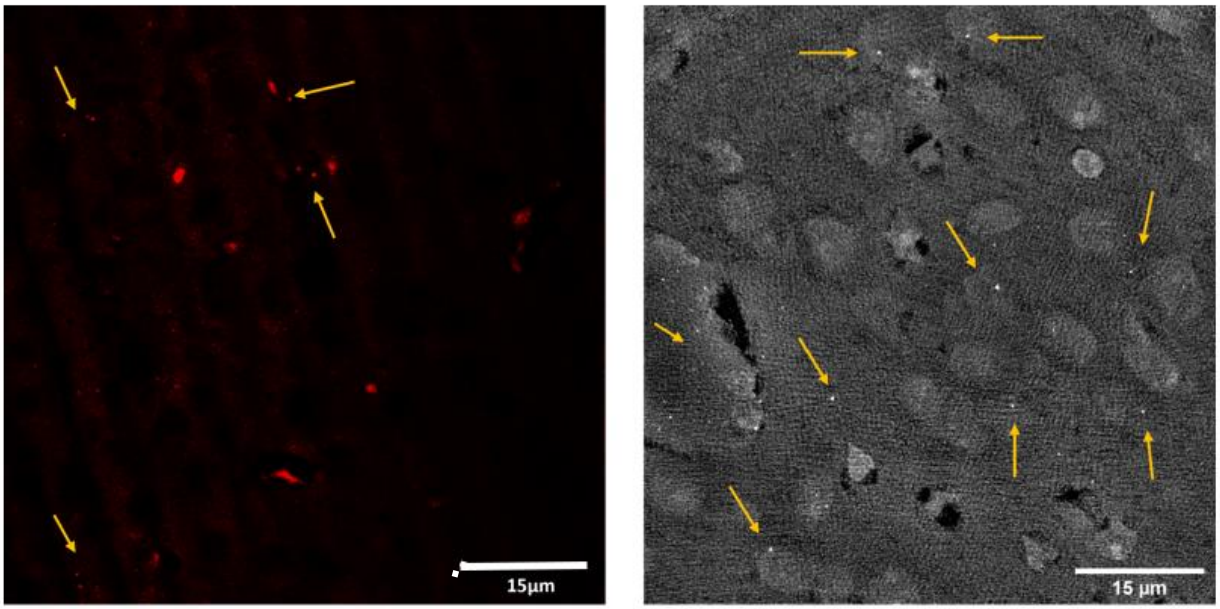

Figure 4.20 On the left, confocal microscopy image on an administered mouse. On the right Holo-nano-tomographic acquisition on an administrated mouse with 40 nm of pixel size (right). Yellow arrows indicate bright points compatible with the presence of Nano2 clusters.

From the comparison between the two signals, information from tomographic acquisition seems to be valuable. Spots present in the two acquisitions are, indeed, comparable in shape, dimension and distribution.

From the results obtained in this experiment we moved on a second nano-holo-tomography experiment with samples from naïve mice intranasally administered with Nano2.

In detail, we studied mice sacrificed at different time points after the administration of the complex:

- 30 minutes after the administration
- 1 hour after the administration
- 2 hours after the administration.

Slices from hemibrains were collected and analyzed with confocal microscopy in order to identify the distribution of the complex within the brain in physiological conditions, with an intact blood-brain-barrier.

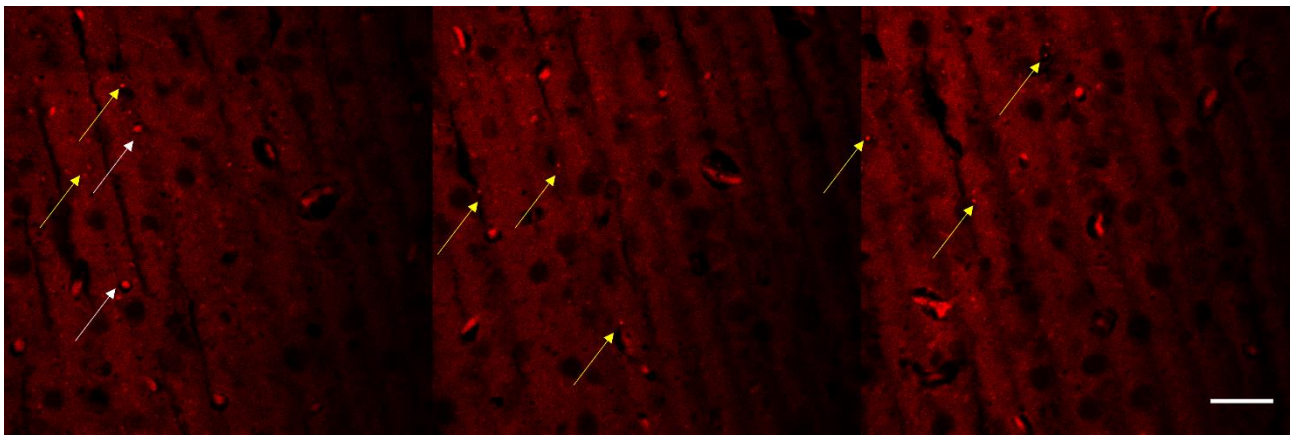

Figure 4.21 Confocal microscopy images on an administrated mouse. Yellow arrows indicate bright points compatible with the presence of Nano2 clusters. Scale bar 20 µm

Confocal images show bright spots corresponding to Au signal (indicated with yellow arrows in fig 4.21). In this configuration are also present auto-fluorescent cells, indicated with white arrows in the figure. However, dimensions of these auto-fluorescence elements are very different from the spots' ones.

As shown in Figure 4.16, cylinders of 500 µm in diameter were extracted from hemibrains embedded in paraffin. For each brain, samples were extracted at different positions:

- Near the olfactory bulb (p3 in Figure 4.22)
- In the middle part of the brain, in the cortex area (p2 in Figure 4.22)
- In the hippocampus area (p1 in Figure 4.22)

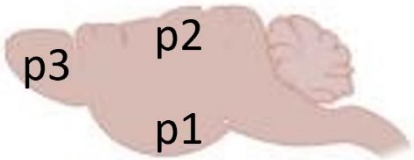

Figure 4.22 Schematic representation of the punching positions.

As in the previous experiment, the samples were imaged at two different pixel sizes, 190 and 40 nm.

When using 40 nm pixel cells are visualized in detail. An example of cell compatible with an astrocyte is shown in Figure 4.23.

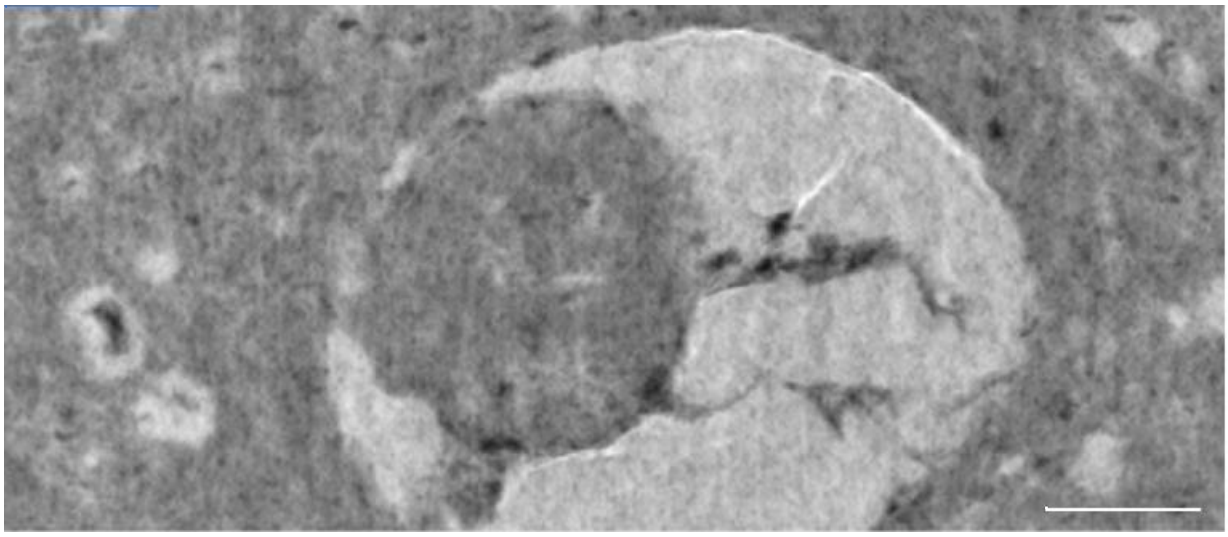

Figure 4.23 Holo-nano-tomographic image of a cell compatible with an astrocyte. Scale bar 15 µm

We studied different time points and different points in the brain to understand how the diffusion behavior of the Nano2 complex inside the tissue affects the detectability in the holo-nano-tomography experiment. The best combination of time after administration and position was 30 minutes p3.

In this configuration, in fact, we are able to detect different interesting points as reported in Figure 4.24.

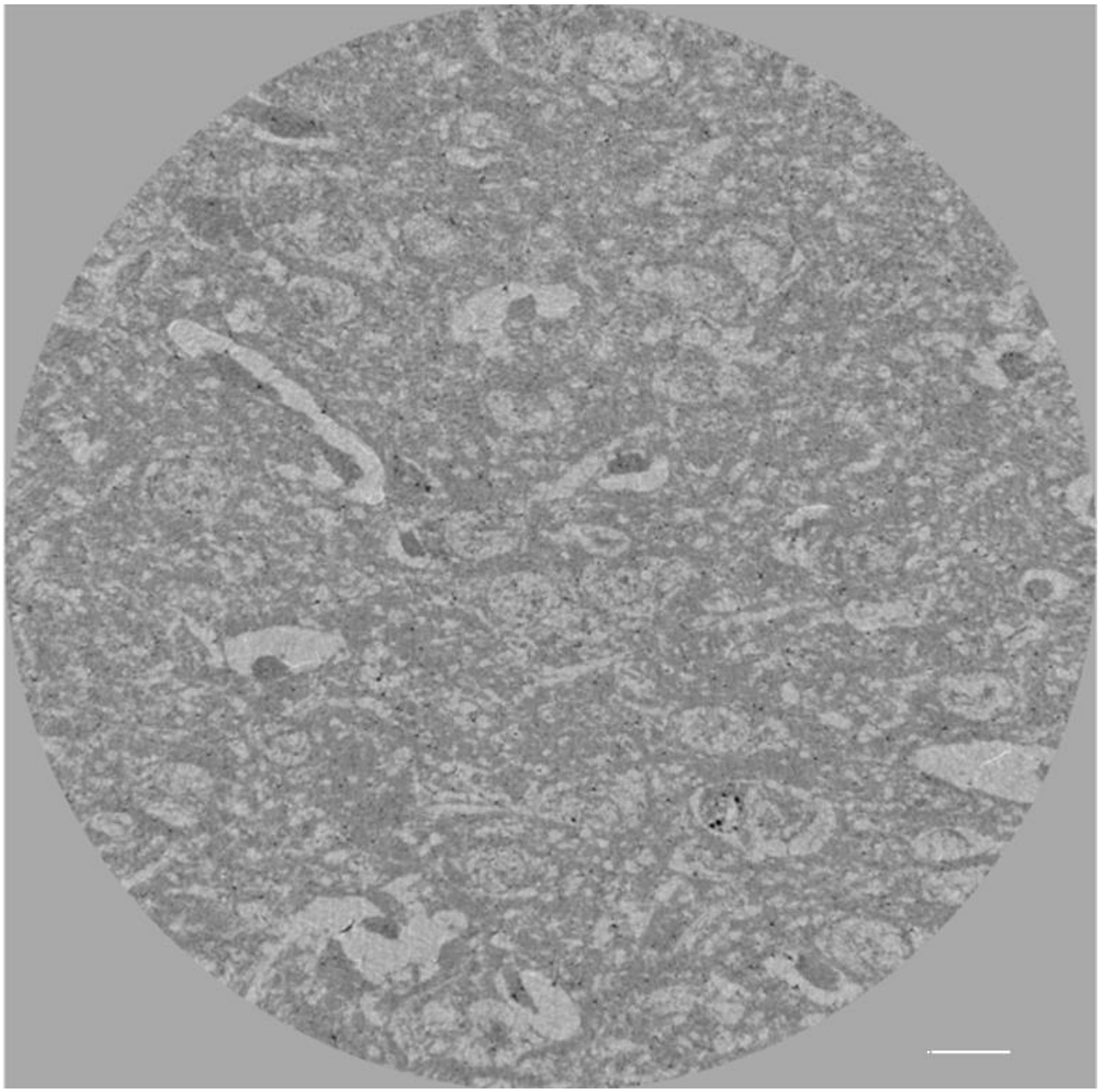

Figure 4.24 Holo-nano-tomographic acquisition on a Nano2 administrated mouse with 40 nm of pixel size. Dark points are compatible with the presence of Nano2 clusters. Scale bar 15 µm

Dark spots visible in the figure are elements compatible with the presence of gold in the sample; in this image, in fact, black corresponds to high density materials.

Starting from this result we performed an X-Ray fluorescence experiment on the area in the red box in Figure 4.25.

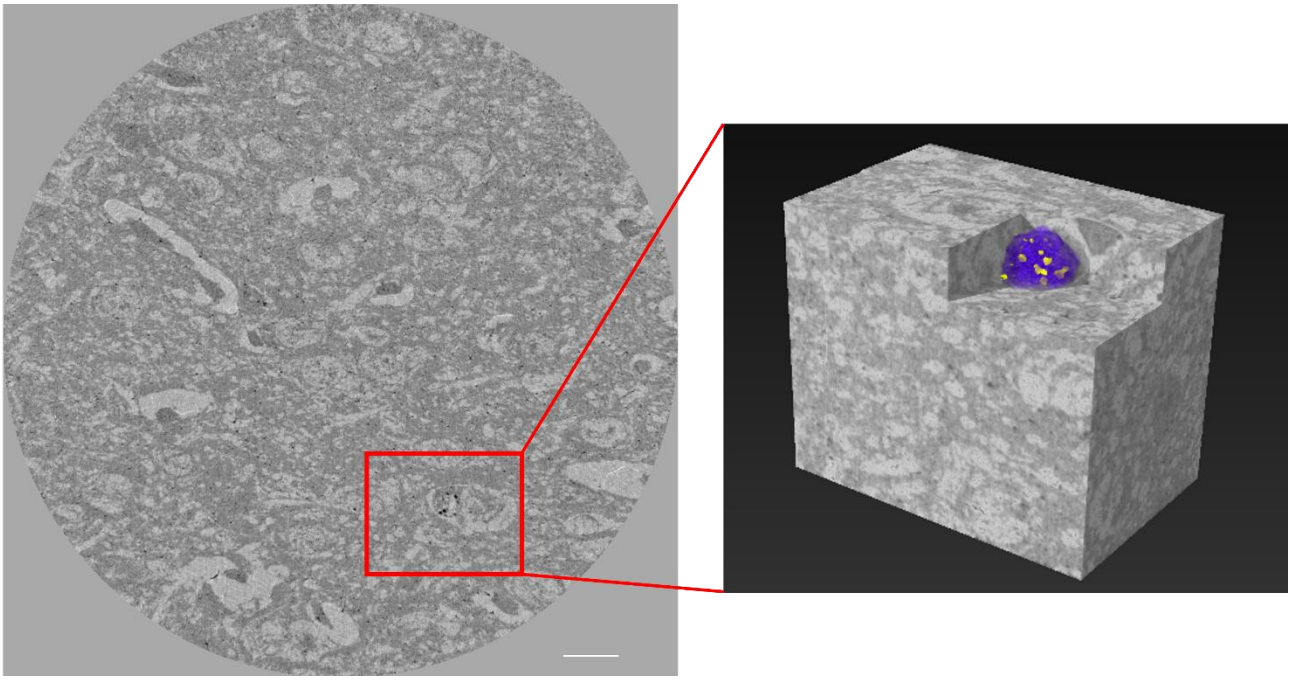

Figure 4.25 Holo-nano-tomographic acquisition on an administrated mouse with 40 nm of pixel size. On the right a 3D rendering of the area in the red box. The cell is represented in violet and the elements compatible with the presence of Nano2 in yellow. Scale bar 15 µm

In the XRF experiment maps of different metals were considered in order to evaluate the presence of the gold avoiding overlap with other elements present in the brain. Maps of the three L-edge of the gold compared with Ca and Zn maps are reported in Figure 4.26.

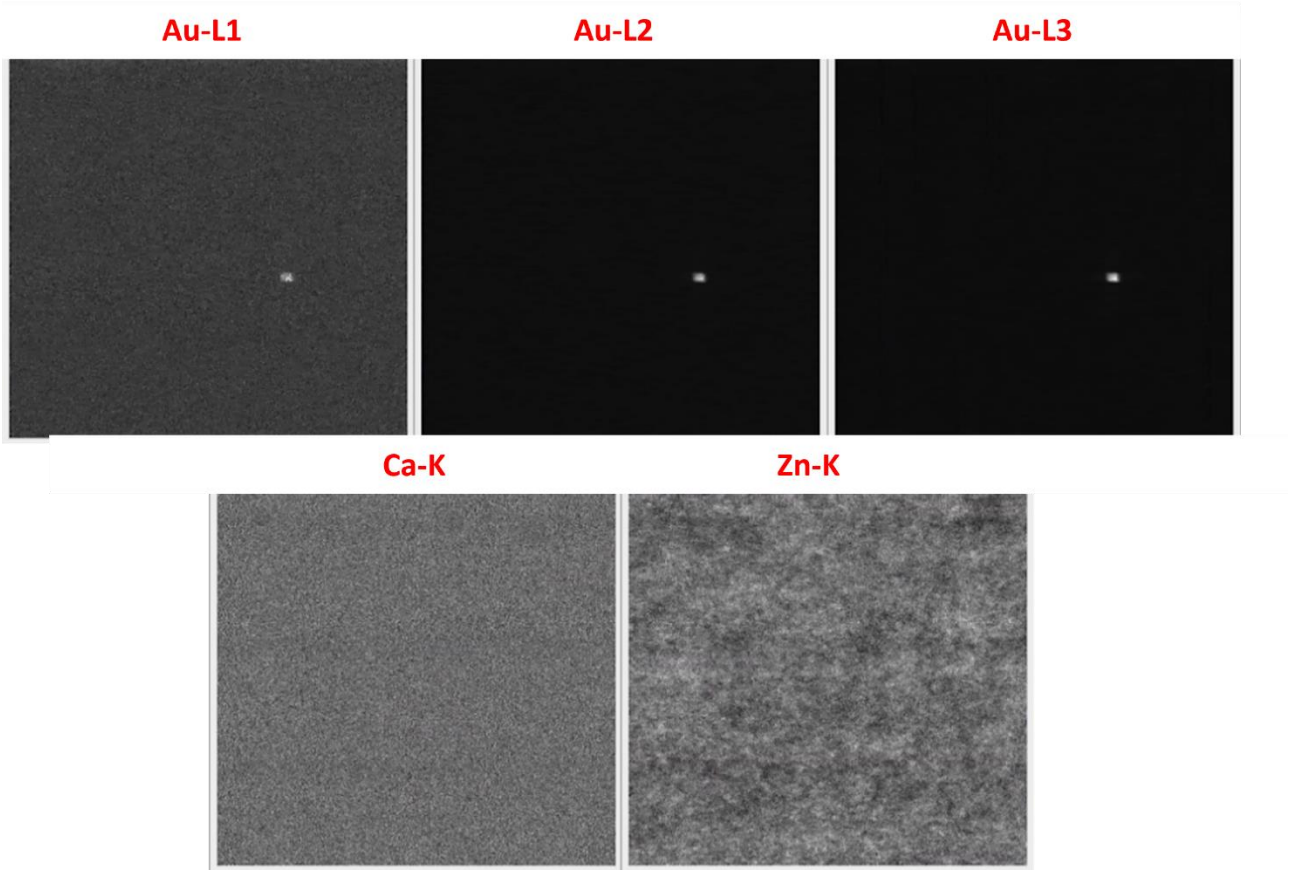

Figure 4.26 Synchrotron radiation X-Ray fluorescence maps of Au L1, Au L2, Au L3, Ca, Zn.

This is a strong and definitive indication of the presence of gold in the region of interest.

The spectrum collected in this experiment, together with the counts registered in correspondence of the peaks of interest, confirms it.

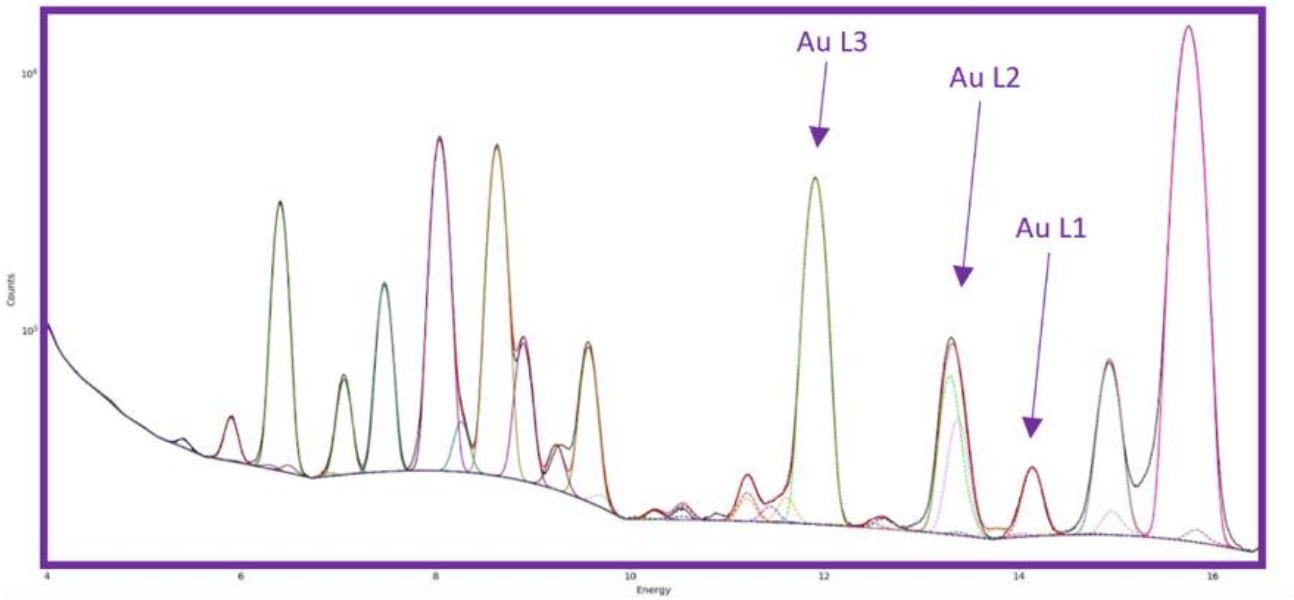

Figure 4.27 XRF spectra of different metals (represented with different colors) and fit of the acquired data. Energy on the x axis, counts on the y axis.

To have a final validation of the result we also performed a quantitative analysis on the gray values of the dark spots in the tomographic images. This test confirmed the presence of gold in our samples.

With this last experiment we proved that Nano2 can cross the BBB in physiological and pathological conditions, important point to be able to use the methods for the study of neurodegenerative diseases in which the comparison between healthy, affected and treated sample is fundamental. Another crucial information we collected from these experiments is that the holo-nano-tomography allows for the visualization of the cells of interest and of the complex, leading to a specific labeling.

Despite these important results, we need to face the limit that holo-nano-tomography doesn't provide with a single acquisition information about the whole brain (or organ in general) and can't be used for *in-vivo* experiments.

Discussion and Conclusions

Neurodegenerative diseases are a broad and heterogeneous class of disorders affecting millions of people worldwide. The number of people affected is constantly increasing and this represents a serious issue for the entire world population, also in economic terms. The costs for the diagnosis and treatment of neurodegenerative diseases, plus the cost of an acceptable quality of life for patients, are high. Common symptoms of neurodegenerative disorders include cognitive decline, motor symptoms, speech and language disorders, psychiatric and behavioral changes; these symptoms affect daily activities, making independent living difficult. To date, there is no cure for this type of disorders and the mechanisms underlying the diseases are not fully understood. In light of this, it becomes evident that new strategies are needed to study and understand neurodegenerative disorders and to test new drugs. Imaging techniques represent an important support for these studies, but, nevertheless, the available techniques do not meet all needs. Tools such as MRI, PET, SPECT or CT suffer from limitations in terms of spatial resolution and can not provide a simultaneous visualization of the cells of interest together with the surrounding tissue and the vascular and neuronal networks. This is a serious drawback for the study of neurodegenerative diseases, in which the follow up of the cells of interest is crucial as well as the appreciation of the pathology-induced microscopic and submicroscopic morphological changes in the tissues.

X-Ray phase contrast tomography is a powerful imaging technique that allows the 3D visualization of objects with a resolution ranging from a few dozen of nanometers to microns; the ability to image low absorbing materials makes this technique very useful in biomedical applications. Neurodegenerative disorders studies by XPCT show how this technique can provide three-dimensional information about details and changes in the central nervous system without the use of

contrast agent and while leaving the sample intact and available for experiments with other techniques. Despite the extremely important pros, XPCT is not able to specifically identify cells, except from a morphological point of view, and this always requires complementary and destructive immune-histo-chemical techniques.

This thesis project was born with the idea to add specificity to XPCT, to make it self-standing and able to solve biomedical problems. To this aim, we implemented XPCT introducing a complex we called Nano2 composed by metal nanoparticles and nanobodies. In this study we used Au nanoparticles and a GFAP nanobodies. The nanobody specifically targets the selected cells (astrocytes); through XPCT we detect the nanoconjugate (Au) by exploiting their physical properties (high Z). The initial idea was to apply this new technique to *ex-vivo* and *in-vivo* experiments. This project required several validation and feasibility steps before the detectability one. Once selected the nanoparticles and the nanobody, the first step concerned the functionalization of the former and the conjugation with the latter. Different protocols and techniques were used to be able of obtaining a stable complex with the wanted ratio between nanoparticles and nanobodies. We decided to set this ratio to 1:1 to better control the specific targeting of the cells. Tests using different techniques, such as TEM, DLS, PL, BCA assay and FTIR, confirmed the desired ratio (paragraph 4.1.2); we then validated the capacity of the complex to bind the selected GFAP antigen with the LSPR technique (paragraph 4.1.3). We then tested two different administration routes (intranasal and intravenous) to establish the one leading to a better diffusion and distribution within the brain (paragraph 4.1.4). First administration tests were performed on EAE affected mice presenting an altered BBB. Confocal microscopy experiments have shown that intranasal administration of Nano2 is followed by enhanced diffusion of the complex in the brain. Confocal microscopy also confirmed the astrocytes targeting capability of the nanoconjugate after the administration (4.1.5). The first X-Ray imaging test was a LES experiment: the co-registration of the results of this experiment with the ones obtained from confocal microscopy measurements on the same slab evidenced how LES radiography technique is

able to detect the Au signal. Starting from this 2D information we moved to the first 3D experiment, a KES tomography test. After a challenging image post processing, I proved the possibility to detect the presence and the distribution of Nano2 in the brain (by gold detection with KES) and confirmed these results with confocal microscopy experiments.

Next step involved several XPCT tests to determine the right quantity of Nano2 to be administered and to confirm the best administration route. These tests were performed on EAE affected and on healthy mice to verify the feasibility of the protocol both in pathological and normal conditions.

Both situations showed differences between the administered and the non-administered sample, indicating that (i) the complex can cross an intact BBB and that (ii) with XPCT we are able to identify their presence in the brain. Confocal microscopy images confirmed this interpretation. However, the limited pixel size of the experiments didn't allow us to reliably access the detection of Nano2 and to visualize the cells of interest and the colocalization with the complex. From this point we moved to holo-nano-tomography experiments on samples extracted from different locations in the brains of mice with EAE, sacrificed at different time points after intranasal administration of Nano2.

This experiment helped us to better understand the diffusion behavior of the complex inside the brain and allowed us to visualize cells and tissue in detail and to identify elements compatible with the presence of Nano2. The same experiment was performed on mice with an intact BBB, to test the capability of the technique in normal physiological conditions. Features indicating the possible presence of the nanoconjugate pushed me to perform a XRF experiment. This elemental test provided me the prove that the signal visible in the holo-nano-tomography images came from Au nanoparticles.

On the details of interest, I also acquired quantitative information about the gray values/densities and this analysis confirmed that the selected elements were clusters of Nano2. From the last experiment we can assess that we create a stable complex able to cross the BBB in physiological and pathological conditions and to spread within the brain, mostly after an intranasal administration (paragraph 4.1.6).

We proved that holo-nano-tomography is able to detect complex clusters and to simultaneously visualize them, the tissue and the cells of interest. However, this technique only provides information about a small volume portion, and it is not applicable to *in-vivo* experiments.

With my PhD thesis work I started a complex project *ex-novo* requiring several initial validation steps. Each of these steps presented some challenges, from the sample preparation to the image processing. In general, for all the tests I needed a large amount of nanoparticles and nanobodies with relative costs, and I used several techniques and instruments present in different laboratories around Europe (I carried out experiments in Italy (Lecce, Rome, Trieste), France (Grenoble) and Switzerland (Villigen)). The Covid-19 pandemic of course affected this project introducing delays, limiting the mobility and creating problems with the animals' availability. A type of study like the one presented here, which employs numerous techniques and requires validation steps, can often encounter unforeseen issues and experience delays. In my case, in addition to the logistical problems already mentioned, there were technical issues. Firstly, when conducting validation measurements such as LSPR (Localized Surface Plasmon Resonance) measurements, we realized that the nanoparticles we had functionalized did not exhibit a plasmonic peak due to their limited size. To confirm the binding specificity of Nano2 to its cytoplasmic protein, GFAP, it was necessary to start from scratch by functionalizing, conjugating, and characterizing new nanoparticles with a larger diameter. A second critical point was the choice of the nanobody. The original idea was to use membrane antibodies to achieve dense clusters of Nano2, easily identifiable with micro XPCT. For various reasons, however, we ended up using an intracellular antibody, and this could be one of the reasons we encountered difficulties in confidently identifying the complex in images with micrometric resolutions. The choice to use EAE mice to ensure the BBB permeability increasing implied temporal issues also. Once injected, mice needed time to develop the disease and in some cases it never happened; this drawback has clearly led to postponements of some experiments, and its criticality has increased as many enclosures have suffered from the conditions dictated by Covid19 and the delays in protocol

approvals. Another minor technical issue concerned the challenging subtraction imaging post-processing already described. In particular for the KES experiment I didn't use a detector capable of simultaneously imaging the sample at two different energies; this resulted in the subtraction being performed on volumes acquired at different times, after undergoing mechanical displacements and irreversible structural changes, as extensively described in the dedicated section. Analyzing details with dimensions of a few microns certainly suffers from misalignments and errors of a few pixels. In some cases, it was sufficient to repeat the two measurements with the sample completely dehydrated and then align the mechanical displacements, while in others, the data proved to be unusable.

The issues mentioned in this discussion have led to a modification of the original project plan.

The results obtained in my experiments undoubtedly leave the door open for new tests that could achieve the initial aim of this project: detecting Nano2 and specifically targeting cells of interest inside the entire brain in *ex-vivo* and *in-vivo* XPCT experiments.

In the validation and development of this new technique, further speculation is required. Some interesting points could be the choice of nanoparticles' metal, the type of nanobody (intracellular or membrane nanobody for example), the Nano2 quantity to be administrated and the sacrifice time to find the best configuration to achieve the goal of the project.

The work of these three years has laid the foundations for the potential development of a new imaging technique capable of providing answers to the many questions still open in the study of neurodegenerative diseases.

Appendix

Experimental details

Synthesis and functionalization of Au nanoparticles

2-nm sized Au nanoparticles were prepared following the procedure reported by Porret et al. (2017). Larger gold nanoparticles were prepared and conjugated to the nanobody, and thanks to the plasmon resonance effect they were used to assay the binding affinity between the conjugated nanoparticle and the antigen. To this aim, citrate coated Au nanoparticles (size: 5.5 nm) were prepared according to the Turkevich approach with slight modifications (Turkevich et al., 1951; Arocikia Jency et al., 2018). In detail, 1.8 mL of 0.010 M HAuCl4 3H2O and 500 µL of 0.010 M sodium citrate were added to 40 mL of ultrapure H2O and stirred for few minutes. Then, 120 µL of freshly prepared 0.10 M NaBH4 were added dropwise to the solution and left under stirring for 2 h. Hereafter, the freshly prepared solution was incubated with an aqueous solution of α-Mercapto-ω-carboxy PEG (5 mM) to exchange citrate with PEG molecules and stirred for additional 2 h. Then, the nanoparticles were thoroughly washed with centrifuge filters to remove excess ligands at 2,000 rcf for at least five times.

From this point on, the two types of Au nanoparticles were derivatized with the same surface chemistry. First, the nanoparticles were coated with a PEG mixture (α-Amino-PEG/α-Amino-ω-carboxy-PEG, molar ratio 10/1) through EDC: an aqueous solution of the PEG mixture (1 mL, 1 mM) was mixed to 1 mL 10 µM nanoparticles prior to add EDC (50 mM). The mixture was left under stirring for 3 h at room temperature. Subsequently, the nanoparticles were washed at 2,000 rcf at least

five times by using centrifugal filters. Similarly, Nα,Nα-Bis(carboxymethyl)-L-lysine molecules were anchored to the surface, followed by incubation with NiCl2 100 mM overnight (O.N.).

After being thoroughly washed with ultrapure water through centrifugal filters to remove excess nickel salt, the nanoparticle solution was incubated with the nanobody (molar ratio NP:NB equal to 1:2) O.N. at 4°C. Then, the nanobody-conjugated nanoparticles were washed prior to being used for characterization and biological studies. The nanoparticles were stored at 4°C. The final nanoconjugate was henceforth referred to as Nano2.

Characterization of Au nanoparticles

TEM images were recorded on a Jem1011 microscope (JEOL Ltd., Tokio, Japan) operating at an accelerating voltage of 100 kVp. A drop of nanoparticle solution was casted onto the carbon-coated grid and let dry before imaging. The size of the nanoparticles as measured by the TEM was estimated by ImageJ Software (Schneider et al., 2012). Electrophoretic characterization was carried out by running the nanoparticles through 1% agarose gel immersed in TBE buffer (pH 8.0) for 1 h at 100 V.

The hydrodynamic diameter (DLS measurements) and the surface charge (Zeta potential measurements) of the nanoparticles were measured by means of a Zetasizer Nano ZS90 (Malvern Instruments, United States) equipped with a 4.0 mW He–Ne laser operating at 633 nm and with an avalanche photodiode detector.

The concentration of AuNPs was estimated via elemental analysis using an Inductively Coupled Plasma Atomic Emission Spectrometer (ICP-AES) Varian 720-ES. A calibration curve of Au was prepared, and the relative amount of metal per sample was estimated upon acidic digestion in HNO3. The Bicinchoninic Acid (BCA) Protein Assay was used to estimate quantitatively the nanobody linked to the nanoparticles. A calibration curve of the nanobody was prepared. UV-vis absorption

spectra of the nanoparticles were recorded with a Varian Cary 300 UV-VIS spectrophotometer. Fourier transform infrared (FTIR) spectra were taken with a Perkin Elmer Spectrum One Fourier Transform spectrophotometer (Waltham, MA, United States); each spectrum was ac-quired with 64 scans and a resolution of 4 cm−1. To acquire the spectra, all the samples were dissolved in water and drop casting films were prepared directly on the ATR prism; spectra were collected after water evaporation.

Nano2/Antigen binding test

To estimate the binding affinity between the Nano2 and the GFAP antigen, glass substrates were cut from glass microscope cover slides into 15 mm × 15 mm slides that were cleaned in an ultrasonic bath with acetone and isopropanol, followed by plasma oxygen treatment to activate OH groups. Soon after, the slides were immersed in a slightly acidic solution of tiopronin 50 mM and shaken O.N. Then, the solution was removed, the slides washed with ultrapure water prior to being incubated with the GFAP antigen (20 nM in PBS) at 4°C O.N. At the end of the incubation time, the slides were rinsed with PBS and then incubated with BSA (1 mg/mL in PBS for 1 h). Finally, they were washed several times. Control slides coated with BSA and without the antigen were prepared as well.

In the binding test, two types of nanoparticles, both Nb-conjugated nanoparticles and AuNPs (without the nanobody, simply coated by PEG) were assayed on the glass slides to assess the affinity between the conjugated nanobody and the antigen as compared to the unconjugated AuNP.

The nanoparticles solutions (either Au-Nb or Au-PEG, 10 nM in PBS) were added to the slices and left under stirring for 1 h, at 4°C. Then, the solution was removed and the slides were analyzed accordingly.

Transmission spectra of the glass slides at normal incidence were measured in air with a spectrometer (Ava Spec HS TEC) before and after the functionalization. Spectra were registered in the range 400–800 nm, integration 100 ms, 10 averages, using glass as the reference.

Optical setup: the light coming from the Tungsten lamp (100 W) was collected to the optical fiber (727-733-2447, Ocean Optics) through a monochromator, then hits the sample and was sent to the spectrometer input port by another optical fiber (M38 L02 Thorlabs) with a 200-µm core diameter.

Astrocyte labelling and confocal microscopy

Astrocyte staining was performed on 4-8 µm thick brain sections using anti-Glast antibody coupled to PE (anti-GLAST Polyclonal antibody (Invitrogen #PA5-72895, 1:250, 1 h, RT) and anti-Rabbit IgG (H + L)-AF555 (Invitrogen, #P-2771MP, 5 µg/mL, 1 h, RT), to label the astrocytes. Fluorescence microscopy was performed on a Carl Zeiss LSM710 laser confocal microscope, using a plan-Apochromat 60x NA 1.4 oil-immersion objective and an APD detector ($\lambda_{exc.}$=405 nm, $\lambda_{em.}$ = 736 nm long pass filter for Au detection, and $\lambda_{exc.}$=543 nm, $\lambda_{em.}$ = 550–600 nm for PE detection).

Confocal microscopy

The images from the X-ray experiments were co-registered/compared to confocal microscopy images acquired on the same samples. In details, confocal Z-stack microscopy (Olympus FV1000), in reflection mode, by using a 405 nm-excitation laser line, a dichroic mirror DM405/488 and with a Z-resolution up to 200 nm was used. The individuation of Nano2 clusters was obtained by performing spatially resolved photoluminescence (SR-PL) spectra during the confocal scanning.

X-Ray imaging

ID 17 beamline at ESRF (Grenoble, France)

ID17 is one of the longest beamlines at ESRF, dedicated to biomedical research with a focus on imaging, radiation biology, radiosurgery, and radiotherapy. Experiments can be performed both in-vivo and ex-vivo in two separated endstations.

The first one is located inside the storage ring building, at 38.5 m from the wiggler source which provides intense-filtered X-ray beams, mainly used for microbeam radiation therapy (MRT) programs, and pink beam for microtomography.

The second endstation is located at 148.5 m from the source in an external building. The second hutch uses only monochromatic radiation (users can choose between 4 different monochromators, generating different ranges of energies and beam sizes). This external hutch is used for experiments of X-ray phase-contrast imaging, dual energy imaging techniques, radiobiology, radiotherapy.

In the following tables are reported the parameters used in the experiments performed at ID17.

KES Experiment	
Energy	Monochromatic, above and below 80.7 keV
Distance	2.3 m
Detector	PCO.Edge 5.5
Optics	2x

FOV (HxV)	5.0 mm x 6.0 mm
Pixel Size	3.05 μm
# Projections	3500
Acquisition Mode	180°
Exposure Time per frame	300 ms

ID 16 beamline at ESRF (Grenoble, France)

The ID16A beamline at ESRF is 185-m long beamline which provides a high-brilliance beam for nano-imaging, focusing on problems in biology, biomedicine and nanotechnology using X-ray fluorescence microscopy and nano-tomography. It is optimized for hard X-ray focusing of a beam with a large energy bandwidth at specific energies (17 keV or 33.6 keV). The beam presents high demagnification (sub-micrometer focused beam size) and high coherence. ID16A combines coherent imaging techniques and X-ray fluorescence microscopy. Two coherent imaging techniques, X-ray holographic and ptychographic tomography, provide the electron density distribution at length scales ranging from ~130 nm down to ~10 nm, while keeping a relatively large field of view. Multilayer-coated Kirkpatrick-Baez optics is used to focus the X-rays. The nano-focusing optics are combined with a carefully designed mechanical device for stable sample positioning and accurate scanning. The sample is put in the divergent beam downstream of the focus to produce magnified phase contrast images. The projection geometry also allows zooming into specific regions of a large sample by combining scans with different magnifications and FOV (Mokso et al., 2007; Bartels et al., 2015).

The beamline is equipped to perform holotomography by recording magnified radiographs at different sample-to-detector distances onto an X-ray detector using a FReLoN-charged coupled device. The samples are measured in vacuum. 2D and 3D imaging can be performed with cryogenic sample preservation to maintain the physiological conditions of biological samples close to their native state and reduce damage caused by radiation.

Holo-nano-tomography experiment	
Energy	17 keV *(divergent beam)*
Distance	225mm, 175mm, 75 mm, 45mm
Detector	FReLoN CCD
Optics	multilayer coated Kirkpatrick-Baez mirrors
FOV	/
Pixel Size	190 nm, 40 nm
# Projections	1500

TOMCAT beamline at SLS – PSI (Villigen, Switzerland)

The beamline for Tomographic Microscopy and Coherent radiology experiments (TOMCAT) offers cutting-edge technology and scientific expertise for exploiting the distinctive peculiarities of

synchrotron radiation for fast, non-destructive, high resolution, quantitative investigations on a large variety of samples.

The energy range available of 8-45 keV allows the use of several techniques such as Absorption-based and phase contrast imaging, Ultra-fast tomographic microscopy, Grating Interferometry and absorption and phase contrast nano-tomography. Different combinations of optical systems and detectors provide voxel sizes ranging from 0.16 to 11 μm (fields-of-view (h x v) of 0.4 x 0.3 mm^2 and 22 x 3-7 mm^2, respectively)]. Typical acquisition times are on the order of seconds to a few minutes. However, dynamic processes can be followed in 4D (3D space + time) using the ultra-fast endstation, which provides sub-second temporal resolution for extended time periods thanks to the in-house developed GigaFRoST system. Moreover, a temporal resolution of a few (< 5) minutes can also be achieved with the hard X-ray full-field microscope setup delivering a pixel size of 65 nm for microscopic samples (~75x75 μm^2 field-of-view).

XPCT experiment	
Energy	Monochromatic, 17 keV
Distance	5 cm
Detector	Pco.EDGE 5.5
Optics	4x
FOV (HxV)	4.16 mm x 3.51 mm
Pixel Size	1.625 μm
# Projections	3000
Mode	Half acquisition (360°)

Exposure Time	50 ms

SYRMEP at ELETTRA (Trieste, Italy)

The SYRMEP (SYnchrotron Radiation for MEdical Physics) beamline has been designed by Sincrotrone Trieste, in collaboration with the University of Trieste and the INFN, for research in medical diagnostic radiology, material science and life science applications.

The light source is a bending magnet. The experimental hutch is placed 20 m downstream, providing monochromatic or white-beam configuration, based on a double-crystal Si (111) which works in an energy range between 8 keV and 40 keV with a laminar-section beam with a maximum area of 120x4 mm^2. The available imaging techniques at the SYRMEP beamline are conventional absorption radiology and tomography, phase contrast imaging, diffraction enhanced imaging.

XPC radiography was performed with 2 energies: 11.9 keV, for imaging below the L-edge of absorption of gold, and 12 keV, just above the L-edge. Pixel size was set to 1.98 μm thanks to a system which allows to vary it with continuity. The sample-to-detector distance was fixed at 50 cm. 9 images for each radiography were collected with an exposure time of 10 seconds. In order to increase the contrast to noise ratio, images were summed.

LES experiment	
Energy	Monochromatic, 11.9-12 keV

Distance	50 cm
Detector	Pco.EDGE 5.5
Optics	/
FOV (HxV)	/
Pixel Size	1.98 μm
# Projections	10
Mode	Radiography
Exposure Time	10 s

Bibliography

1. Wilson, D.M., et al., *Hallmarks of neurodegenerative diseases.* Cell, 2023. **186**(4): p. 693-714.
2. Arya, A.D., et al., *A systematic review on machine learning and deep learning techniques in the effective diagnosis of Alzheimer's disease.* Brain Informatics, 2023. **10**(1): p. 1-15.
3. Aramadaka, S., et al., *Neuroimaging in Alzheimer's Disease for Early Diagnosis: A Comprehensive Review.* Cureus, 2023. **15**(5).
4. Lemasson, B., et al., *In vivo imaging of vessel diameter, size, and density: a comparative study between MRI and histology.* Magnetic resonance in medicine, 2013. **69**(1): p. 18-26.
5. Wei, Z., et al., *Brain metabolism in tau and amyloid mouse models of Alzheimer's disease: An MRI study.* NMR in Biomedicine, 2021. **34**(9): p. e4568.
6. Ricci, M., et al., *Positron emission tomography (PET) and neuroimaging in the personalized approach to neurodegenerative causes of dementia.* International Journal of Molecular Sciences, 2020. **21**(20): p. 7481.
7. Pavese, N. and D.J. Brooks, *Imaging neurodegeneration in Parkinson's disease.* Biochimica et Biophysica Acta (BBA)-Molecular Basis of Disease, 2009. **1792**(7): p. 722-729.
8. Mitchell, T., et al., *Emerging neuroimaging biomarkers across disease stage in Parkinson disease: a review.* JAMA neurology, 2021. **78**(10): p. 1262-1272.
9. Khan, S., K.H. Barve, and M.S. Kumar, *Recent advancements in pathogenesis, diagnostics and treatment of Alzheimer's disease.* Current neuropharmacology, 2020. **18**(11): p. 1106-1125.
10. Janeiro, M.H., et al., *Biomarkers in Alzheimer's disease.* Advances in Laboratory Medicine/Avances en Medicina de Laboratorio, 2021. **2**(1): p. 27-37.
11. Colombé, C., et al., *Gold nanoclusters as a contrast agent for image-guided surgery of head and neck tumors.* Nanomedicine: Nanotechnology, Biology and Medicine, 2019. **20**: p. 102011.
12. Zhao, J., et al., *The roles of gold nanoparticles in the detection of amyloid-β peptide for Alzheimer's disease.* Colloid and Interface Science Communications, 2022. **46**: p. 100579.
13. Samykutty, A., et al., *Simultaneous Detection of Multiple Tumor-targeted Gold Nanoparticles in HER2-Positive Breast Tumors Using Optoacoustic Imaging.* Radiology: Imaging Cancer, 2023. **5**(3): p. e220180.
14. Sancey, L., et al., *Long-term in vivo clearance of gadolinium-based AGuIX nanoparticles and their biocompatibility after systemic injection.* ACS nano, 2015. **9**(3): p. 2477-2488.
15. Broekgaarden, M., et al., *Surface functionalization of gold nanoclusters with arginine: A trade-off between microtumor uptake and radiotherapy enhancement.* Nanoscale, 2020. **12**(13): p. 6959-6963.
16. Schültke, E., et al., *Single-cell resolution in high-resolution synchrotron X-ray CT imaging with gold nanoparticles.* Journal of synchrotron radiation, 2014. **21**(1): p. 242-250.
17. Cruje, C., et al., *PEG-modified gadolinium nanoparticles as contrast agents for in vivo micro-CT.* Scientific Reports, 2021. **11**(1): p. 16603.
18. Detappe, A., et al., *Ultrasmall silica-based bismuth gadolinium nanoparticles for dual magnetic resonance–computed tomography image guided radiation therapy.* Nano letters, 2017. **17**(3): p. 1733-1740.
19. Kruger, R.A., et al., *Digital K-edge subtraction radiography.* Radiology, 1977. **125**(1): p. 243-245.
20. Li, T., et al., *Camelid single-domain antibodies: A versatile tool for in vivo imaging of extracellular and intracellular brain targets.* Journal of Controlled Release, 2016. **243**: p. 1-10.

21. Bélanger, K., et al., *Single-domain antibodies as therapeutic and imaging agents for the treatment of CNS diseases.* Antibodies, 2019. **8**(2): p. 27.
22. Pérez-Osorio, I.N., et al., *Nose-to-brain delivery of dexamethasone: Biodistribution studies in mice.* Journal of Pharmacology and Experimental Therapeutics, 2021. **378**(3): p. 244-250.
23. Loftus, J.R., S. Puri, and S.P. Meyers, *Multimodality imaging of neurodegenerative disorders with a focus on multiparametric magnetic resonance and molecular imaging.* Insights into Imaging, 2023. **14**(1): p. 1-35.
24. Hansson, O., *Biomarkers for neurodegenerative diseases.* Nature medicine, 2021. **27**(6): p. 954-963.
25. Erkkinen, M.G., M.-O. Kim, and M.D. Geschwind, *Clinical neurology and epidemiology of the major neurodegenerative diseases.* Cold Spring Harbor perspectives in biology, 2018. **10**(4): p. a033118.
26. Dawson, T.M., T.E. Golde, and C. Lagier-Tourenne, *Animal models of neurodegenerative diseases.* Nature neuroscience, 2018. **21**(10): p. 1370-1379.
27. Colpo, G.D., et al., *Animal models for the study of human neurodegenerative diseases*, in *Animal Models for the Study of Human Disease*. 2017, Elsevier. p. 1109-1129.
28. Rivers, T.M., D. Sprunt, and G. Berry, *Observations on attempts to produce acute disseminated encephalomyelitis in monkeys.* The Journal of experimental medicine, 1933. **58**(1): p. 39.
29. Larochelle, C., J.I. Alvarez, and A. Prat, *How do immune cells overcome the blood–brain barrier in multiple sclerosis?* FEBS letters, 2011. **585**(23): p. 3770-3780.
30. Greenwood, J., *Mechanisms of blood-brain barrier breakdown.* Neuroradiology, 1991. **33**: p. 95-100.
31. Stromnes, I.M., et al., *Differential regulation of central nervous system autoimmunity by TH1 and TH17 cells.* Nature medicine, 2008. **14**(3): p. 337-342.
32. Ferrara, G., et al., *NG2, a common denominator for neuroinflammation, blood–brain barrier alteration, and oligodendrocyte precursor response in EAE, plays a role in dendritic cell activation.* Acta Neuropathologica, 2016. **132**: p. 23-42.
33. Luo, J., et al., *Bioluminescence in vivo imaging of autoimmune encephalomyelitis predicts disease.* Journal of Neuroinflammation, 2008. **5**(1): p. 1-6.
34. Schellenberg, A.E., et al., *Magnetic resonance imaging of blood–spinal cord barrier disruption in mice with experimental autoimmune encephalomyelitis.* Magn. Reson. Med. , 2007. **58**(2): p. 298-305.
35. Daniel, P., D. Lam, and O. Pratt, *Changes in the effectiveness of the blood-brain and blood-spinal cord barriers in experimental allergic encephalomyelitis: Possible relevance to multiple sclerosis.* Journal of the neurological sciences, 1981. **52**(2-3): p. 211-219.
36. Mathis, C.A., et al., *Imaging technology for neurodegenerative diseases: progress toward detection of specific pathologies.* Archives of neurology, 2005. **62**(2): p. 196-200.
37. Fratini, M., et al., *Simultaneous submicrometric 3D imaging of the micro-vascular network and the neuronal system in a mouse spinal cord.* Sci. Rep., 2015. **5**(1): p. 1-7.
38. Bukreeva, I., et al., *Quantitative 3D investigation of Neuronal network in mouse spinal cord model.* Sci. Rep., 2017. **7**(1): p. 1-10.
39. Arfelli, F., et al., *Low-dose phase contrast x-ray medical imaging.* Physics in Medicine & Biology, 1998. **43**(10): p. 2845.
40. Horng, A., et al., *Multiscale X-ray phase contrast imaging of human cartilage for investigating osteoarthritis formation.* Journal of Biomedical Science, 2021. **28**: p. 1-14.
41. Barbone, G.E., et al., *High-spatial-resolution three-dimensional imaging of human spinal cord and column anatomy with postmortem X-ray phase-contrast micro-CT.* Radiology, 2021. **298**(1): p. 135-146.
42. Brombal, L., et al., *Image quality comparison between a phase-contrast synchrotron radiation breast CT and a clinical breast CT: a phantom based study.* Scientific reports, 2019. **9**(1): p. 17778.
43. Massimi, L., et al., *Volumetric high-resolution X-ray phase-contrast virtual histology of breast specimens with a compact laboratory system.* IEEE transactions on medical imaging, 2021. **41**(5): p. 1188-1195.

44. Cedola, A., et al., *X-ray phase contrast tomography reveals early vascular alterations and neuronal loss in a multiple sclerosis model.* Sci. Rep., 2017. **7**(1): p. 1-11.
45. Palermo, F., et al., *Multilevel X-ray imaging approach to assess the sequential evolution of multi-organ damage in multiple sclerosis.* Communications Physics, 2022. **5**(1): p. 290.
46. Töpperwien, M., et al., *Correlative x-ray phase-contrast tomography and histology of human brain tissue affected by Alzheimer's disease.* Neuroimage, 2020. **210**: p. 116523.
47. Bravin, A., P. Coan, and P. Suortti, *X-ray phase-contrast imaging: from pre-clinical applications towards clinics.* Phys. Med. Biol., 2012. **58**(1): p. R1.
48. Bouchet, A., et al., *Preferential effect of synchrotron microbeam radiation therapy on intracerebral 9L gliosarcoma vascular networks.* International Journal of Radiation Oncology* Biology* Physics, 2010. **78**(5): p. 1503-1512.
49. Bonse, U. and M. Hart, *An X-ray interferometer.* Applied Physics Letters, 1965. **6**(8): p. 155-156.
50. Hsieh, J., *Computed tomography: principles, design, artifacts, and recent advances.* 2003.
51. Russo, P., *Handbook of X-ray imaging: physics and technology*. 2017: CRC press.
52. Seibert, J.A. and J.M. Boone, *X-ray imaging physics for nuclear medicine technologists. Part 2: X-ray interactions and image formation.* Journal of nuclear medicine technology, 2005. **33**(1): p. 3-18.
53. Russo, P., *2.01 Physical basis of X-ray imaging.* Comprehensive biomedical physics, 2014: p. 1-48.
54. Zabler, S., et al., *Optimization of phase contrast imaging using hard x rays.* Review of Scientific Instruments, 2005. **76**(7).
55. Southwell, W., *Validity of the Fresnel approximation in the near field.* JOSA, 1981. **71**(1): p. 7-14.
56. Parrent, G.B. and B.J. Thompson Jr, *On the Fraunhofer (far field) diffraction patterns of opaque and transparent objects with coherent background.* Optica Acta: International Journal of Optics, 1964. **11**(3): p. 183-193.
57. Grella, R., *Fresnel propagation and diffraction and paraxial wave equation.* Journal of Optics, 1982. **13**(6): p. 367.
58. Sheriff, R.E., *Understanding the Fresnel zone.* AAPG Explorer, 1996: p. 18-19.
59. Fowles, G.R., *Introduction to modern optics*. 1989: Courier Corporation.
60. Olivo, A. and E. Castelli, *X-ray phase contrast imaging: From synchrotrons to conventional sources.* La rivista del nuovo cimento, 2014. **37**: p. 467-508.
61. Giuliani, A. and A. Cedola, *Advanced High-Resolution Tomography in Regenerative Medicine: Three-Dimensional Exploration into the Interactions between Tissues, Cells, and Biomaterials*. 2018: Springer.
62. Nugent, K.A., *Coherent methods in the X-ray sciences.* Advances in Physics, 2010. **59**(1): p. 1-99.
63. Snigirev, A., et al., *On the possibilities of x-ray phase contrast microimaging by coherent high-energy synchrotron radiation.* Review of scientific instruments, 1995. **66**(12): p. 5486-5492.
64. Wilkins, S., et al., *Phase-contrast imaging using polychromatic hard X-rays.* Nature, 1996. **384**(6607): p. 335-338.
65. Pogany, A., D. Gao, and S. Wilkins, *Contrast and resolution in imaging with a microfocus x-ray source.* Review of Scientific Instruments, 1997. **68**(7): p. 2774-2782.
66. Mayo, S.C., et al., *X-ray phase-contrast microscopy and microtomography.* Optics express, 2003. **11**(19): p. 2289-2302.
67. Cowley, J., *Coherent and incoherent imaging in the scanning transmission electron microscope.* Journal of Physics D: Applied Physics, 1975. **8**(6): p. L77.
68. Olivo, A. and R. Speller, *A coded-aperture technique allowing x-ray phase contrast imaging with conventional sources.* Applied Physics Letters, 2007. **91**(7).
69. Diemoz, P., et al. *Edge illumination X-ray phase-contrast imaging: nanoradian sensitivity at synchrotrons and translation to conventional sources*. in *Journal of Physics: Conference Series*. 2014. IOP Publishing.
70. Endrizzi, M. and A. Olivo, *Absorption, refraction and scattering retrieval with an edge-illumination-based imaging setup.* Journal of Physics D: Applied Physics, 2014. **47**(50): p. 505102.
71. Momose, A., et al., *Demonstration of X-ray Talbot interferometry.* Japanese journal of applied physics, 2003. **42**(7B): p. L866.

72. Burvall, A., et al., *Phase retrieval in X-ray phase-contrast imaging suitable for tomography.* Optics express, 2011. **19**(11): p. 10359-10376.
73. Paganin, D., et al., *Simultaneous phase and amplitude extraction from a single defocused image of a homogeneous object.* J. Microsc., 2002. **206**(1): p. 33-40.
74. Krol, A., *In-line hard X-ray holography for biomedical imaging.* In-line Hard X-ray Holography for Biomedical Imaging, Holography, Research and Technologies, 2011. **21**: p. 423-440.
75. Kulpe, S., et al., *K-edge subtraction imaging for coronary angiography with a compact synchrotron X-ray source.* PLoS One, 2018. **13**(12): p. e0208446.
76. Margaritondo, G., Y. Hwu, and G. Tromba, *Synchrotron light: From basics to coherence and coherence-related applications.* science, 2003. **3**: p. 1.
77. Mobilio, S. and A. Balerna. *Introduction to the main properties of Synchrotron Radiation*. in *Conference Proceedings-Italian Physical Society*. 2003. Editrice Compositori; 1999.
78. Huang, Z., *Brightness and coherence of synchrotron radiation and FELs.* 2013.
79. Bahrdt, J., *Insertion devices.* 2006.
80. Janssens, K.H., F. Adams, and A. Rindby, *Microscopic X-ray fluorescence analysis*. Vol. 434. 2000: Wiley Chichester.
81. Potts, P.J. and P.C. Webb, *X-ray fluorescence spectrometry.* Journal of Geochemical Exploration, 1992. **44**(1-3): p. 251-296.
82. Nwaneshiudu, A., et al., *Introduction to confocal microscopy.* Journal of Investigative Dermatology, 2012. **132**(12): p. 1-5.
83. Semwogerere, D. and E.R. Weeks, *Confocal microscopy.* Encyclopedia of biomaterials and biomedical engineering, 2005. **23**: p. 1-10.
84. De, M., P.S. Ghosh, and V.M. Rotello, *Applications of nanoparticles in biology.* Advanced Materials, 2008. **20**(22): p. 4225-4241.
85. Han, X., et al., *Applications of nanoparticles in biomedical imaging.* Nanoscale, 2019. **11**(3): p. 799-819.
86. Kelly, K.L., et al., *The optical properties of metal nanoparticles: the influence of size, shape, and dielectric environment*. 2003, ACS Publications. p. 668-677.
87. Jain, P.K., et al., *Noble metals on the nanoscale: optical and photothermal properties and some applications in imaging, sensing, biology, and medicine.* Accounts of chemical research, 2008. **41**(12): p. 1578-1586.
88. Murphy, C.J., et al., *Gold nanoparticles in biology: beyond toxicity to cellular imaging.* Accounts of chemical research, 2008. **41**(12): p. 1721-1730.
89. Song, C., et al., *Ultrasmall iron oxide nanoparticles: Synthesis, surface modification, assembly, and biomedical applications.* Drug discovery today, 2019. **24**(3): p. 835-844.
90. Duchesne, L., et al., *Robust ligand shells for biological applications of gold nanoparticles.* Langmuir, 2008. **24**(23): p. 13572-13580.
91. Jin, B.-k., et al., *Nanobodies: a review of generation, diagnostics and therapeutics.* International Journal of Molecular Sciences, 2023. **24**(6): p. 5994.
92. Yang, E., et al., *Engineering nanobodies for next-generation molecular imaging.* Drug Discovery Today, 2022. **27**(6): p. 1622-1638.
93. Ratliff, S.T., *Webb's Physics of Medical Imaging*. 2013, Wiley Online Library.
94. Beatty, J., *The radon transform and the mathematics of medical imaging.* 2012.
95. Cloetens, P., et al., *Holotomography: Quantitative phase tomography with micrometer resolution using hard synchrotron radiation x rays.* Applied physics letters, 1999. **75**(19): p. 2912-2914.
96. Brun, F., *From Projections to the 3D Analysis of the Regenerated Tissue.* Advanced High-Resolution Tomography in Regenerative Medicine: Three-Dimensional Exploration into the Interactions between Tissues, Cells, and Biomaterials, 2018: p. 69-90.
97. Vo, N.T., et al., *Reliable method for calculating the center of rotation in parallel-beam tomography.* Optics express, 2014. **22**(16): p. 19078-19086.
98. Brun, F., et al., *SYRMEP Tomo Project: a graphical user interface for customizing CT reconstruction workflows.* Advanced structural and chemical imaging, 2017. **3**(1): p. 1-9.

99. Rueden, C.T. and K.W. Eliceiri, *ImageJ for the next generation of scientific image data.* Microsc. Microanal., 2019. **25**(S2): p. 142-143.
100. Van Nieuwenhove, V., et al., *Dynamic intensity normalization using eigen flat fields in X-ray imaging.* Optics express, 2015. **23**(21): p. 27975-27989.
101. Perruchini, C., et al., *Llama VHH antibody fragments against GFAP: better diffusion in fixed tissues than classical monoclonal antibodies.* Acta neuropathologica, 2009. **118**: p. 685-695.
102. Kim, J.-H., et al., *Synthesis and anti-melanogenic effects of lipoic acid-polyethylene glycol ester.* Journal of Pharmacy and Pharmacology, 2008. **60**(7): p. 863-870.
103. Barth, A., *The infrared absorption of amino acid side chains.* Progress in biophysics and molecular biology, 2000. **74**(3-5): p. 141-173.
104. Huang, Y., L. Fuksman, and J. Zheng, *Luminescence mechanisms of ultrasmall gold nanoparticles.* Dalton Transactions, 2018. **47**(18): p. 6267-6273.
105. Tokel, O., F. Inci, and U. Demirci, *Advances in plasmonic technologies for point of care applications.* Chemical reviews, 2014. **114**(11): p. 5728-5752.
106. Miller, M.M. and A.A. Lazarides, *Sensitivity of metal nanoparticle surface plasmon resonance to the dielectric environment.* The Journal of Physical Chemistry B, 2005. **109**(46): p. 21556-21565.